Structure Function Relationships in Medial Entorhinal Cortex

DISSERTATION

zur Erlangung des akademischen Grades

d o c t o r re r u m n a t u r a l i u m

Dr. rer. nat.

im Fach Biologie

eingereicht an der

Lebenswissenschaftlichen Fakultät

der Humboldt-Universität zu Berlin

von

MSc Neuroscience

QIUSONG TANG

Präsident der Humboldt-Universität zu Berlin
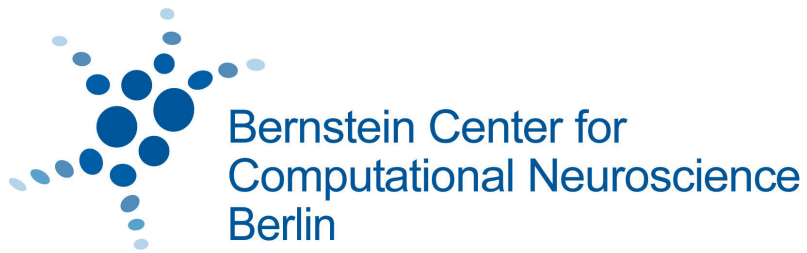
Prof. Dr. Jan-Hendrik Olbertz

Dekan der Lebenswissenschaftlichen Fakultät

Prof. Dr. Richard Lucius

Gutachter/innen:

1. Prof. Dr. Michael Brecht

2. Prof. Dr. Richard Kempter

3. Prof. Dr. Dietmar Schmitz

Tag der mündlichen Prüfung: 17.03.2015

Structure Function Relationships in Medial Entorhinal Cortex

PhD candidate:

Qiusong Tang

Supervisor:

Prof. Dr. Michael Brecht

December 2014

Bernstein Center for Computational Neuroscience

Animal Physiology / Systems Neurobiology and Neural Computation

Humboldt University of Berlin, Germany

Table of Contents

List of Figures

1. Abstract

Little is known about how medial entorhinal cortical microcircuits contribute to spatial navigation. Layer 2 principal neurons of medial entorhinal cortex divide into calbindin-positive pyramidal cells and dentate-gyrus-projecting calbindin-negative stellate cells. Calbindin-positive pyramidal cells bundled dendrites together and formed patches arranged in a hexagonal grid aligned to layer 1 axons, parasubiculum and cholinergic inputs. Calbindin-positive pyramidal cells were strongly theta modulated. Calbindin-negative stellate cells were distributed across layer 2 but avoided centers of calbindin-positive pyramidal patches, and were weakly theta modulated. We developed techniques for anatomical identification of single neurons recorded in trained rats engaged in exploratory behavior. Furthermore, we assigned unidentified juxtacellular and extracellular recordings based on spike phase locking to field potential theta. In layer 2 of medial entorhinal cortex, weakly hexagonal spatial discharges and head direction selectivity were observed in both cell types. Clear grid discharges were predominantly pyramidal cells. Border cells were mainly stellate neurons. Thus, weakly theta-locked border responses occurred in stellate cells, whose dendrites sample large input territories, whereas strongly theta-locked grid discharges occurred in pyramidal cells, which sample small input territories in patches organized in a hexagonal 'grid-cell-grid'. In addition, we investigated anatomical structures and neuronal discharge patterns of the parasubiculum. The parasubiculum is a primary target of medial septal inputs and parasubicular output preferentially targeted patches of calbindin-positive pyramidal cells in layer 2 of medial entorhinal cortex. Parasubicular cells were strongly theta modulated and carried mostly head-direction and border information, and might contribute to shape theta-rhythmicity and the (dorsoventral) integration of information across entorhinal grid scales.

2. Zusammenfassung

In dieser Arbeit werden Struktur-Funktionsbeziehungen in der medialen entorhinalen Hirnrinde untersucht. Schicht 2 Neurone im medialen entorhinalen Cortex unterteilen sich in calbindin-positive Pyramidenzellen und calbindin-negative Sternzellen. Calbindin-positive Pyramidenzellen bündeln ihre apikalen Dendriten zusammen und formen Zellhaufen, die in einem hexagolen arrangiert sind. Das Gitter von calbindin-positiven Pyramidenzellhaufen ist an Schicht 1 Axonen und dem Parasubiculum ausgerichtet und wird durch cholinerge Eingänge innerviert. Calbindin-positive Pyramidenzellen zeigen stark theta-modulierte Aktivität. Sternzellen sind vertreut in der Schicht 2 angeordnet und zeigen nur schwach theta-modulierte Aktivität, ein Befund, der gegen eine Rolle von zell-intrinsischen Oszillationen in der Entstehung von Theta-Modulation spricht. In der Arbeit wurden Methoden entwickelt, um durch die juxtazelluläre Färbung und Identifikation von Zellen, die räumlichen Feuermuster von Schicht 2 Sternzellen und Pyramidenzellen zu bestimmen. Insbesondere wird gezeigt, dass die zeitlichen Feuermuster von Sternzellen und Pyramidenzellen so unterschiedlich sind, dass auch Daten von nichtidentifizierten extrazellulär abgeleiteten Zellen Sternzellen und Pyramidenzellen zugeordnet werden können. Die Ergebnisse zeigen, dass Gitterzell (engl. grid cell) Feuermuster relativ selten sind und in der Regel in Pyramidenzellen beobachtet werden. Grenzzell (engl. border cell) Feuermuster sind dagegen meistens in Sternzellen zu beobachten. Weiterhin wurde die Anatomie und Physiologie des Parasubiculums untersucht. Die Ergebnisse deuten auf die Existenz eines hexagonalen 'Gitterzell-gitters' in der entorhinalen Hirnrinde hin und sprechen für starke Struktur-Funktionsbeziehungen in diesem Teil der Hirnrinde.

3.   Introduction

3.1   Encoding of Spatial Memory in Medial Entorhinal Cortex

Our brain is capable of generating representations of the external world and performing computations supporting navigation. Revealing the cellular mechanisms of cognitive brain operations (like mapping of space) is a major challenge of contemporary neuroscience. One of the most exciting discoveries in system neuroscience in the past decades concerns the spatial discharge patterns of medial entorhinal cortex (MEC). The grid cells recorded in medial entorhinal cortex, first described by the work from Mosers and their colleagues (Hafting et al., 2005), are spatially modulated neurons which show periodic, hexagonally arranged spatial firing fields when the animal is exploring the environment, similar to the holes of a Chinese checkerboard (**Figure 1** top). As there is no such grid pattern present in the environment nor in the sensory inputs, it can be assumed that the spatial discharge patterns of grid cells are internally generated. More recently, researchers have identified other spatial modulated cell types, including conjunctive cells and border cells. Conjuctive cells are cells which show both spatial tuning and directional tuning (Sargolini et al., 2006); and border cells are another unique population of cells which will respond specifically to the boundary of the environment (**Figure 1** middle; Solstad et al., 2008). Medial entorhinal cortex also contains head-direction cells, which are thought to be inherited from other parahippocampal areas such as presubiculum and parasubiculum (**Figure 1** bottom; Boccara et al., 2010).
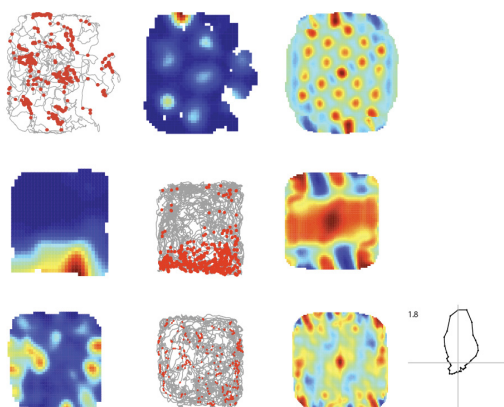
Figure 1: Spatial and directional modulated cells in the hippocampal formation. From top to bottom: grid cell, border cell, head-direction cell. From left to right: raw trajectory (grey) and spikes (red), rate map, spatial autocorrelation map, and head-direction tuning polar plot for head-direction cell.

Given the striking regularity and invariance of the grid representation, grid cells are thought to be part of the brain's coordinate system which supports spatial navigation (see Moser and Moser, 2013 for review). Although the firing pattern of grid cells is not derived from sensory inputs, medial entorhinal cortex receives convergent direct and indirect inputs from many sensory associated cortices. Grid cell activity could arise from local circuit computations that integrate all sensory and directional information of the environment. In the past years, a massive experimental, computational and modeling

effort has been undertaken to understand how grid cells can emerge from brain circuits, but the underlying neuronal mechanisms have remained mysterious with competing experimental evidence and theoretical implications. Understanding the cellular mechanisms of spatial representations is therefore central to the field and should be addressed before we can make biophysical realisitic models and theoretical assumptions.

3.2   Spatial Tuning in Layer 2 of Medial Entorhinal Cortex

The microcircuitry of layer 2 of medial entorhinal cortex is poorly understood. There is an impetus for focusing on layer 2, considering that it is the major output structure to the hippocampus and it contains the largest density of pure grid cells (Hafting et al., 2005; Boccara et al., 2010) and border cells (Solstad et al., 2008). Theta oscillations, which are generated by medial septal GABAergic and cholinergic inputs, are the most prominent local field potential oscillatory pattern (4-12 Hz) observed in the hippocampal formation. Strong temporal (Mizuseki et al., 2009; Boccara et al., 2010; Quilichini et al., 2010) firing patterns in layer 2 of medial entorhinal cortex have been described: 1. Many grid cells show phase precession, a phenomenon where the firing phase of each action potential will precess in relation to the local field theta oscillations, when the animal enters the grid firing field (Hafting et al., 2008). 2. It has been suggested that most grid cells are strongly theta modulated, oscillating in theta frequencies (Boccara et al., 2010). Disruption of theta oscillations by blocking medial septum causes a profound disruption of grid pattern in medial entorhinal cortex (Brandon et al., 2011; Koenig et al., 2011). It has been suggested that stellate cells in layer 2 of medial entorhinal cortex would generate entorhinal theta oscillations (Alonso and Llinás, 1989; Alonso and Klink, 1993) and grid activity (Hasselmo et al., 2007) by their intrinsic subthreshold membrane potential oscillations at theta frequency. Our understanding of medial entorhinal microcircuits is limited, however, because most of the experimental work stem from extracellular recordings of unidentified cells. Recent work has addressed this issue with intracellular recordings (Burgalossi et al., 2011; Domnisoru et al., 2013; Schmidt-Hieber and Häusser, 2013). Such recordings have characterized many spatial modulated cell types (Sargolini et al., 2006; Solstad et al., 2008; Krupic et al., 2012) in layer 2. The clustering and modularity of grid cells (Stensola et al., 2012) suggest there might be a strong anatomical topography of grid cells, but so far none of the studies have identified molecular markers of grid modules. It is not clear either, how functionally defined cell types correspond to stellate and pyramidal cells (Germroth et al., 1989; Alonso and Klink, 1993).

3.3   Principal Cell Types in Layer 2 of Medial Entorhinal Cortex

Pure grid cells are primarily found in layer 2 (Boccara et al., 2010), which differs from other cortical layers. Here the two types of principal cells, stellate and pyramidal neurons have been described in details before (Alonso and Klink, 1993; Germroth et al., 1989). Specifically, stellate and pyramidal neurons differ in conductances, immunoreactivity projection patterns and inhibitory inputs (Alonso and Llinás, 1989; Lingenhöhl and Finch, 1991; Klink and Alonso, 1997; Varga et al., 2010; Canto et al., 2012).

Very recent work indicates that stellate and pyramidal neurons can be reliably differentiated by calbindin immunoreactivity (**Figure 2**) and that these cells also differ in their inhibitory inputs (Varga et al., 2010). Calbindin-positive (calbindin+) cells have been recently shown to receive specific CCK+
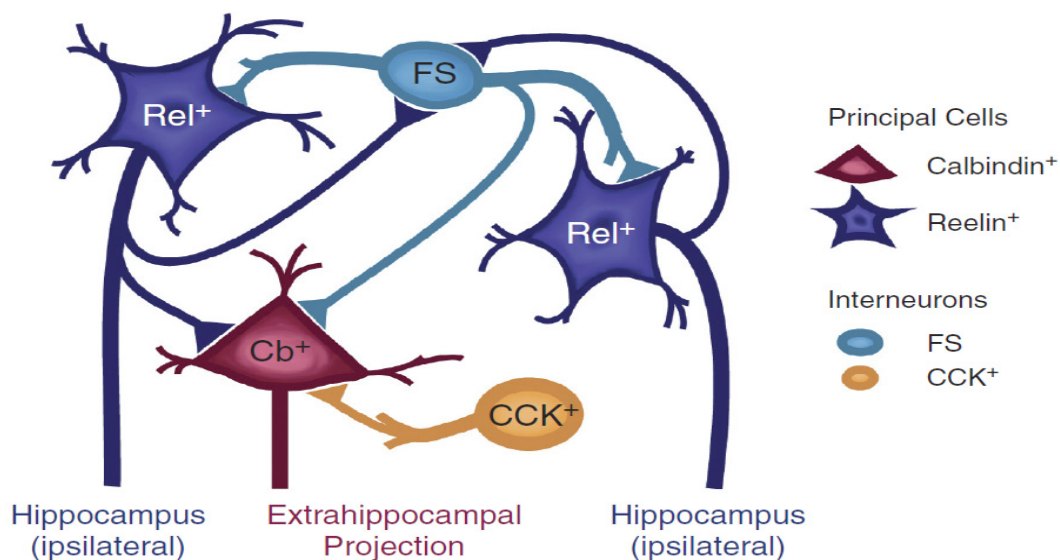
Figure 2: Microcircuitry in layer 2 of medial entorhinal cortex, adapted from Burgalossi and Brecht, 2014. Reelin-positive stellate cells project to the ipsilateral hippocampus and are interconnected via fast-spiking interneurons (FS); Calbindin-positive pyramidal cells are specifically targeted by CCK-positive interneurons and don't project to the ipsilateral hippocampus.

inhibitory inputs, not project to dentate gyrus (Varga et al., 2010), while calbindin-negative (calbindin-)/ Reelin-positive (Reelin+) neurons are homogeneously distributed, receive local GABAergic inputs, and project primarily to the dentate-gyrus (Varga et al., 2010). Few studies have so far explored structure-function relationships in entorhinal circuits (Schmidt-Hieber and Häusser, 2013; Domnisoru et al., 2013; Zhang et al., 2013; see Rowland and Moser, 2014 and Burgalossi and Brecht, 2014 for reviews). The functional implications of such remarkable cellular diversity of layer 2, the cellular identity and microcircuit structure of layer 2 cells in the MEC, thus, remains largely unresolved.

Resolving how differential spatial firing relates to principal cell types will clarify the cellular

mechanisms of grid discharges and spatial input patterns to distinct subfields of the hippocampus. This could only be done, by taking advantage of improved methodologies for identifying individual neurons recorded in freely moving animals, give the reality that previous available techniques have limits (Burgalossi et al., 2011; Herfst et al., 2012; Domnisoru et al., 2013; Schmidt-Hieber and Häusser, 2013). This approach could ultimately provide direct and indirect evidence, if pyramidal and stellate cells have differential spatial responses, respectively.

3.4   Parasubiculum as Major Input to Medial Entorhinal Cortex

The analysis of spatial discharge patterns in hippocampal and parahippocampal brain regions is a remarkable success story (Moser et al., 2008; Moser and Moser, 2013). Extracellular recordings revealed an astonishing degree of complexity, abstractness, but also understandability of discharge patterns such as place, head-direction, border- and grid cells. Along with the exploration of discharge properties, anatomists delineated in great detail the basic circuitry of the hippocampal formation (Amaral and Witter, 1989; van Strien et al., 2009).

The immense amount of data available about certain parts of the hippocampal formation – such as dorsal CA1 in the rodent – should not blind us for gaps in our knowledge about less 'classic' hippocampal processing nodes. The parasubiculum is one such structure that lies beyond the classic tri-synaptic hippocampal loop (Andersen et al., 1971) and has been relatively little investigated. This parahippocampal region provides massive input to layer 2 of medial entorhinal cortex (van Groen and Wyss, 1990; Caballero-Bleda and Witter, 1993, 1994) and shows prominent expression of markers for cholinergic activity (Slomianka and Geneser, 1991). Early physiological analysis described a small fraction of place-responsive cells in the parasubiculum (Taube, 1995). Subsequent extracellular recordings have also identified head-direction-, border- and grid-responses among parasubicular neurons (Cacucci et al., 2004; Boccara et al., 2010).

From a physiological and an anatomical perspective, the parasubiculum is somewhat difficult to study, due to its small size and complications with recordings and tracer injections. Furthermore, the position of the parasubiculum, on the caudal edge of the parahippocampal lobe, with a strong bending of the cortical sheet- greatly complicates the delineation of the parasubiculum. Providing a comprehensive description of parasubicular circuits by combining anatomical and functional approach is necessary (Burgalossi et al., 2011; Tang et al., 2014a). Specifically, it would be interesting to know how parasubicular circuits relate to pyramidal and stellate neuron microcircuits in layer 2 of medial entorhinal cortex (Ray et al., 2014; Tang et al., 2014b) . In our analysis we investigate four issues: First, we delineate the location, shape, laminar organization and internal structure of parasubiculum.

Second, we investigate the sources of parasubicular inputs as well as the targets of parasubicular outputs. Third, we assess spatial discharge patterns of identified parasubicular neurons by juxtacellular recording/labeling in freely moving rats. Fourth, we assess the temporal discharge patterns of identified and unidentified parasubicular neurons.

3.5   Methodology for Revealing Structure-Function Relationships in the brain

Deciphering the coding algorithms of neural circuits that give rise to certain behaviors is a most exciting topic in contemporary neuroscience. Neuronal circuits consist of a huge variety of neuronal cell types, which differ in morphology, intrinsic properties, molecular identity, microcircuit connectivity and projection patterns (Klausberger and Somogyi, 2008; Krook-Magnuson et al., 2012). Thus, resolving the contribution of individual neurons must be done before one can understand the cellular basis of behavior. A high degree of structure to function specialization and identification of distinct subclasses of interneurons has been described (Ascoli et al., 2008; Klausberger et al., 2003). For principal cells, which make up the large majority of cortical neurons, we still lack a mechanistic understanding. Although currently available evidence suggests a complex heterogeneity of principle cell types (Kamme et al., 2003; Kerr et al., 2007; Thompson et al., 2008; Dong et al., 2009; de Kock and Sakmann, 2009; Varga et al., 2010; Lee and Reid, 2011; Oberlaender et al., 2011; Harris and Mrsic-Flogel, 2013; Ray et al., 2014), cortical structure-function relationships at the single cell level remain to be established.

Optogenetic approaches have revolutionized the way for manipulating, probing, and investigating causal structure-function relationships in neuronal activity (Zhang et al., 2010; Fenno et al., 2011). In combination with electrophysiological (Anikeeva et al., 2011; Wang et al., 2012; Deisseroth and Schnitzer, 2013) and optical methods (Prakash et al., 2012; Deisseroth and Schnitzer, 2013), optogenetic manipulations make it possible to characterize cell-type-specific functions in neural circuitry (Aravanis et al., 2007; Zhang et al., 2007). Though with immense powerfulness, current optogenetic tools have two main limitations. Firstly, it is poorly limited to broadly defined cell groups, identified by the expression of individual molecular markers or on projection targets (Cardin et al., 2010; Lee et al., 2010; Chung et al., 2013). Cell types can however rarely be assigned unequivocally by single features (Ascoli et al., 2008; Klausberger and Somogyi, 2008; Battaglia et al., 2013; Kepecs and Fishell, 2014). Secondly, optogenetic approaches are not ideal for microcircuitry analysis, where single cell resolution is required for this. Moreover, by artificially increasing or decreasing neuronal activity by light activation, the network activity is thus not maintained functional according to its configured level; and the upstream/downstream cortical targets can be influenced unexpectedly as well. A precise,

non-manipulative relationship between neuronal activity, morphological diversity and microcircuit wiring diagrams is therefore critical for understanding cortical computation and creating biologically realistic models of neural circuit function (Brown and Hestrin, 2009; Lang et al., 2011; Denk et al., 2012; Potjans and Diesmann, 2014).

We know little about how the cellular mechanisms of neurons in the hippocampal formation give rise to specific spatial and directional firing. Most common electrophysiological techniques (extracellular tetrode recordings) do not allow the identification of the recorded neurons in freely moving animals. Since its establishment (Deschênes et al., 1994; Pinault, 1994, 1996), the juxtacellular recording and labeling technique has become the method of choice for investigating structure-function relationships in the many superficial brain areas (Pinault, 2011). Throughout its emergence and further development, however, most studies have been conducted on simplified (i.e. anesthetized) (Deschênes et al., 1994; Pinault et al., 1995; Pinault, 1994, 1996) or awake head-fixed (Houweling and Brecht, 2008; de Kock and Sakmann, 2009; Mileykovskiy and Morales, 2011; Boucetta et al., 2014;) preparations, and lately in freely-moving preparations limited with anesthetic-wakeup format (Lee et al., 2006; Lee et al., 2009; Herfst et al., 2012).

To overcome this problem, and allow for visualization of single neurons recorded in vivo under natural behaving conditions, it is necessary to improve upon previous existing methodologies (Burgalossi et al., 2011; Herfst et al., 2012). Such improvements should allow us to (1) record single neurons in drug-free rodents, pre-trained to explore large open field environments; (2) identify multiple neurons per animal. The combination of miniaturized pipette-positioning device ("micromanipulator") and novel stabilization & anchoring procedures may improve the stability and success rate of juxtacellular recordings to large extent. The feasibility and applicability of this approach will be very valuable for establishing structure-function relationships in freely behaving animals in the field.

4.   Material and Methods

All experimental procedures were performed according to German guidelines on animal welfare.

4.1   Materials

4.1.1 Surgery and Electrophysiology Reagents

• Experimental animals: Wistar rats (~130-250 g body weight; ~5-9 weeks old). As a rule, we do not recommend starting the procedure with rats larger than 300 g of body weight, as the mechanical stress they can exert upon fixation (step 16) can potentially destabilize the head-implant.

• Isoflourane (Isofluran CP, CP-Pharma, cat. no. 31303, store at 4°C)

• Ketamine (10% wt/vol, CP-Pharma, cat. no. 400203.00.00, store at 4°C)

• Xylazine (2% wt/vol, Bayer, cat. no. 6293841.00.00, store at 4°C)

• Pentobarbital (Narcoren, Merial GmbH, cat. no. 6088986.00.00, store at 4°C)

• Lidocaine (bela-pharm, cat. no. 6357796.00.00, store at 4°C)

• Bupivacaine (Marcaine, Sanofi, store at 4°C)

• Analgesic (Rimadyl, Pfizer, cat. no. 400684.00.00, store at 4°C)

• UV-curable adhesive (3M ESPE Filtek Silorane, cat. no. 4772TK, store at 4°C)

• HEPES (Sigma-Aldrich, cat. no. 54459, store at room temperature, i.e. 20-25°C)

• KCl (Sigma-Aldrich, cat. no. 60129, store at room temperature)

• NaCl (Sigma-Aldrich, cat. no. 71376, store at room temperature)

• $CaCl_2$ (Sigma-Aldrich, cat. no. 21108, store at room temperature)

• $MgCl_2$ (Sigma-Aldrich, cat. no. 63064, store at room temperature)

• NaOH solution (Merck KGaA, cat. no. 109137, store at 4°C)

• Neurobiotin (VectorLabs, cat. no. SP-1120)

Store at -20°C, protect from light and moisture. Biocytin can be used as alternative (Pinault, 1996). Biotinylated Dextran Amines (i.e. BDA-3000) are more resistant to intracellular degradation and can be used for revealing long-range axonal projections (see Introduction)

• Agarose (Sigma-Aldrich, cat. no. A9539, store at room temperature)

• Dental acrylic (Paladur powder and liquid, Heraeus-Kulzer; store at room temperature; mix the two components for preparing dental acrylic, according to manufacturer instructions)

Unpolimerized dental acrylic components can be irritating to the skin and respiratory pathways. Handle under a fume extractor and follow the producer's guidelines.

• Instant glue (cyanoacrylate, Henkel, cat. no. 1436519, store at room temperature)

• Mitomycin (Sigma-Aldrich, cat. no. M4287, store at 4°C)

• Silicone sealant (Kwik-Cast, World Precision Instruments, store at room temperature)

• Streptavidin conjugated to Alexa 546 (Life-Technologies, cat.no. S-11225, store at -20°C)

• Mouse monoclonal anti-Calbindin antibody (Sigma-Aldrich, cat.no. C9848; aliquote and store at -20°C)

• Anti-mouse secondary antibodies (i.e. conjugated with Alexa Fluor 488, Life-Technologies, cat.no. A-11001; aliquote and store at -20°C)

4.1.2 Equipment

• Faraday cage

• Stereomicroscope (e.g., Olympus, Zeiss)

• Cold light source (e.g., Olympus, Zeiss)

• Stereotaxic apparatus (e.g., Narishige)

• Animal body temperature control system (e.g., FHC)

• Drill system (e.g., Foredom)

• Surgical tools (e.g., Fine Science Tools)

• Surgery absorbent swabs (e.g. SUGI, Kettenbach, cat. no. 31602)

• Blue and red LEDs (e.g. Conrad; Red Top-View-LED, cat. no. 175272; Blue Top-View-LED, cat. no. 175265)

• Bridge amplifier with miniature head-stage (ELC-03XS, NPI electronic)

• Miniaturized micromanipulator (4 mm diameter, 16 mm length, 9 mm travel distance; Kleindiek Nanotechnik) (**Figure 3**)

• Audio monitor (e.g., AM10, Grass Technologies)

• Acquisition board (analog-to-digital converter, e.g., Heka LIH 8+8)

• Software for acquiring electrophysiology data (e.g., Patchmaster, Heka; Spike2, CED)

• Animal position tracking system (e.g., Neuralynx)

• Borosilicate glass capillaries (1.5 mm o.d., 0.87 mm i.d.; e.g., Hilgenberg)

• Glass-cutting file (e.g., VWR, cat.no. 470005-474)

• Pipette puller (e.g., P-97, Sutter Instrument)

• 100x air objective (e.g., MPLFLN, working distance 1.0 mm, Olympus)

• Hot plate (e.g., VWR, cat.no. 97042-650)

• 0.5 ml microcentrifuge tubes (e.g., neoLAB, cat. no. 780500)

• Vibratome (e.g., Microm)

• Cryostat (e.g., Leica)

• UV lamp (e.g., Heraeus)

Always wear UV-protection glasses upon use.

- UV-light protection glasses (e.g., Heraeus)
- Software/hardware for 3D morphological reconstruction (e.g., Neurolucida, MBF Bioscience)

4.1.3 Reagent Preparation

Extracellular (Ringer) solution (in mM): NaCl 135, KCl 5.4, HEPES 5, $CaCl_2$ 1.8 and $MgCl_2$ 1 (pH adjusted to 7.2 by adding NaOH, target osmolality 290 mmol kg^{-1}). Make in advance, filter sterile through a 0.2 µm filter and store at 4°C for up to several months.

Pipette solution: Add 1.5-2% Neurobiotin (wt/vol) to Ringer solution (above). As an alternative, biocytin can also be used. Filter through a 0.2 µm filter, make small aliquots (~5-10 µl) and store at temperatures ≤ -20°C. In our experience, aliquots are stable at -20°C for least several months. Osmolarity and pH are critical and should be checked for each batch.

Agar solution: Add 3% (wt/vol) agarose powder to Ringer solution, and boil it in a microwave. The solution becomes clear. Keep the solution on a hot plate and stir throughout the experiment, so that it can be used as liquid when necessary. The agarose solution can be used after it has cooled down to near physiological temperature. Make in advance before each experiment.

Ketamine/Xylazine: mix Ketamine (10% wt/vol) with Xylazine (2% wt/vol), resulting in a final concentration of 80 mg/kg Ketamine and 6 mg/kg Xylazine and injection dose of 0.11 ml/100 g. Supplemental doses should be administered by alternating injections of ketamine and ketamine/xylazine (1/2 of the initial doses) every 30-45 min, or as required. Store ketamine/xylazine mix at 4°C for up to 4-6 weeks.
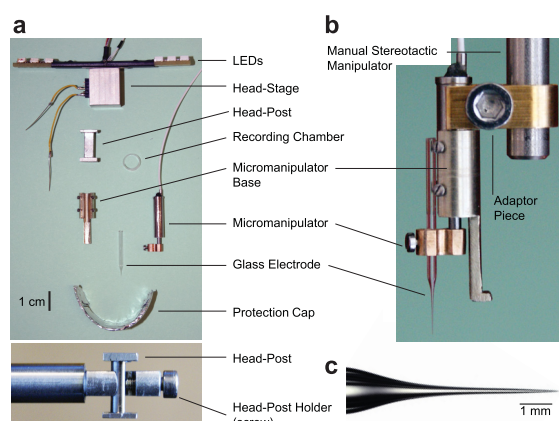
Figure 3: Implant components for obtaining juxtacellular recordings in freely moving animals. (a) The individual components of the implant that are either cemented (head-post, recording chamber, protection cap and micromanipulator base) or mounted on the rat's head for the recording (head-stage and micromanipulator). The bottom image shows a close-up view of the head-post, secured into the head-post holder by means of a screw. The bottom surface of the head-post is cemented on the animal's head (Step 14), whereas the top surface serves as support for the miniaturized head-stage (Step 26). **(b)** The assembled micromanipulator-base complex, which is attached to a manual stereotaxic manipulator via an adapter piece. This assembly is used for positioning and implanting the micromanipulator's base (Step 22). **(c)** High-magnification view of the pipette tip. Adapted from Tang et al., 2014a.

4.1.4 Equipment Setup

Recording chamber: Cut off a circular piece (approx. 5 mm diameter and 2 mm height) from the cap of a 0.5 ml microcentrifuge tube (**Figure 3A**).

LED assembly: Mount red and blue LEDs on a linear support (spacing 4.5 cm) and glue on the miniature head-stage (**Figure 3A**). Record the two lights using the video-tracking system (i.e. Neuralynx) and use them post-hoc for extracting the animal's positional coordinates and heading-direction. Alternatively, head-mountable LEDs integrated within the head-stage can also be used (e.g. from NPI Electronic).

Glass electrodes: Pull pipettes with a long taper, by using a horizontal puller (e.g., P-97, Sutter Instrument). Electrodes should be pulled with a long taper (**Figure 3C**), to avoid/minimize brain tissue damage upon electrode penetration, a tip opening of ~1.5-2 μm and a resistance of 4–6 MΩ. The tip of each electrode should be examined at high magnification (> 1000x total magnification, through a 100x air objective; See equipment). Discard electrodes with irregular, asymmetric shapes.

Protection cap (plastic, shielded with aluminum foil; **Figure 3A**): the protection cap should be light, and it is needed for protecting the implant (in particular the micromanipulator and the recording electrode) during the freely moving behavior. The aluminum foil provides additional electrical isolation from external noise.

Adaptor piece: for mounting the micromanipulator/base complex on a manual stereotaxic manipulator (see **Figure 3B**) (required for implanting the micromanipulator's base on the rodent's head; see step 22).

Rat restrainer box (PVC; length x width x height: 20 cm x 8 cm x 8 cm): the restrainer should be equipped with a top lid, as head-fixation in open space is source of stress and discomfort to the animal (Schwarz et al., 2010).

Head-post: (aluminum or stainless steel; see **Figure 3A**): it is a small piece of metal which is implanted on the rat's head, in tight adherence to the skull, which serves a dual function: to allow head-fixation in the stereotaxic frame and to serve as a base for the miniaturized head-stage.

Head-post holder (stainless steel): for holding the head-post and fixing the head of the rat on the stereotaxic frame. Secure the head-post onto the head-post holder with a screw (see **Figure 3A**).

Micromanipulator base (brass, **Figure 3A**; or aluminum, **Figure 3B**): for mounting the micromanipulator on the rat's head.

Behavioral arena: a square arena is used in the present protocol (1 m x 1 m). However, different geometrical designs are possible. In particular elevated platforms (without walls) can be used to diminish the occurrence of recording losses due to the implant accidentally touching the walls.

4.2 Methods

4.2.1 Anatomy Methods

Brain Tissue Preparation

For anatomy experiments, male and female Wistar rats (150-400 g) were anesthetized by isoflurane, and then euthanized by an intraperitoneal injection of 20% urethane. They were then perfused transcardially with 0.9% phosphate buffered saline solution, followed by 4% paraformaldehyde (PFA) in 0.1 M phosphate buffer (PB). After perfusion, brains were removed from the skull and postfixed in PFA overnight. They were then transferred into a 10% sucrose solution in PB and left overnight, and subsequently immersed in 30% sucrose solution for at least 24 hours for cryoprotection. The brains were embedded in Jung Tissue Freezing Medium, and subsequently mounted on the freezing microtome to obtain 20-60 μm thick sagittal sections or tangential sections (parallel to the pial surface). Tangential sections of the medial entorhinal cortex were obtained by separating posterior cortices (including the entorhinal cortex) from the remaining hemisphere by a cut parallel to the surface of the medial entorhinal cortex. The tissue was then frozen and positioned with the pial side to the block face of the microtome. Tissue from PV-Cre mice, expressing Cre recombinase under the parvalbumin promoter (B6;129P2-Pvalbtm1(cre)Arbr/J mice, stock nr 008069, Jackson, Bar Harbor, ME, USA), was prepared using similar methods, except that the sections were cut on a standard microtome (nominal thickness 100 μm, horizontal) right after overnight fixation in PFA. The mice were injected with AAV-Ef1a-dbf-hChR2(H134R)-EYFP-WPRE (serotype 1/2) roughly 6 weeks prior to perfusion, whereby we targeted the medial septum under stereotaxic guidance: starting from the pial surface at 1 mm anterior, 0.7 mm right lateral to Bregma, a 34-gauge NanoFil™ needle (WPI, Berlin, Germany) was advanced at an angle of 10° in the coronal plane for 4200 and 4600 μm, where we injected 1 μl each (100 nl/s), waiting 5 minutes after each injection before moving the needle.

Histochemistry and Immunohistochemistry

Acetylcholinesterase (AChE) activity was visualized according to previously published procedures (Tsuji, 1998; Ichinohe et al., 2008). After washing brain sections in a solution containing 1 ml of 0.1 M citrate buffer (pH 6.2) and 9 ml 0.9% NaCl saline solution (CS), sections were incubated with CS containing 3 mM $CuSO_4$, 0.5 mM$K_3Fe(CN)_6$, and 1.8 mMacetylthiocholine iodide for 30 min. After rinsing in PB, reaction products were visualized by incubating the sections in PB containing 0.05% 3,3'- Diaminobenzidine (DAB) and 0.03% nickel ammonium sulfate.

Immunohistochemicalstainings were performed according to standard procedures. Briefly, brain sections were pre-incubated in a blocking solution containing 0.1 M PBS, 2% Bovine Serum Albumin (BSA) and 0.5% Triton X-100 (PBS-X) for an hour at room temperature (RT). Following this, primary

antibodies were diluted in a solution containing PBS-X and 1% BSA. We used primary antibodies against the calcium binding protein Calbindin (1:5000), the extracellular matrix protein Reelin (1:1000), the extrinsic membrane protein Myelin Basic Protein (1:1000), the vesicular acetylcholine transporter (1:1000), and the DNA binding neuron specific protein NeuN (1:1000), and for the mice, against green fluorescent protein (GFP). Incubations with primary antibodies were allowed to proceed for at least 24 hours under mild shaking at 4°C in free-floating sections. Incubations with primary antibodies were followed by detection with secondary antibodies coupled to different fluorophores (Alexa 488 and 546). Secondary antibodies were diluted (1:500) in PBS-X and the reaction was allowed to proceed for two hours in the dark at RT. For multiple antibody labeling, antibodies raised in different host species were used. After the staining procedure, sections were mounted on gelatin coated glass slides with Mowiol or Vectashield mounting medium.

In a subset of experiments, primary antibodies were visualized by DAB staining. For this purpose, endogenous peroxidases were first blocked by incubating brain tissue sections in methanol containing 0.3% hydrogen peroxide in the dark at RT for 30 min. The subsequent immunohistochemical procedures were performed as described above, with the exception that detection of primary antibodies was performed by biotinylated secondary antibodies and the ABC detection kit. Immunoreactivity was visualized using DAB staining.

For whole-mount immunohistochemistry, we used a variant of the protocol in (Sillitoe and Hawkes, 2002; Jährling et al., 2008). Thick tangential sections (~ 300 µm) containing layer 2 of MEC were first post-fixed in Dent's fixative overnight at 4°C and then incubated in Dent's bleach overnight at 4°C. They were then dehydrated twice in 100% methanol for 30 min each and then rehydrated for 90 min each in 50% and 15% methanol in PBS at RT. Subsequently, sections were incubated with 10 µg/ml proteinase K for 5 min at RT. Sections were then rinsed three times for ten minutes in PBS at RT and subsequently incubated in PBS-X containing 2% BSA overnight. Primary antibodies were diluted in PBS-X containing 5% DMSO, 1% BSA and incubated for 96 hours at 4°C. After this incubation, whole-mounts were washed in PBS-X three times for 2–3 h each and then incubated overnight in secondary antibodies diluted in PBS-X and 5% DMSO at 4°C. Sections were then washed three times in PBS-X for 2–3 h each and incubated in PBS-X overnight to ensure efficient removal of unbound antibodies. The sections were dehydrated in series of 50%, 80%, and 100% methanol in PBS at RT for 90 min each. Finally, the sections were transferred for at least 2 days into a clearing solution consisting of two parts of benzyl benzoate and one part of benzyl alcohol at RT, until they became transparent.

For histological analysis of juxtacellularly-labeled neurons, neurobiotin was visualized with streptavidin conjugated to Alexa 546 (1:1000). Subsequently, immunohistochemistry for Calbindin

was performed as described above and visualized with Alexa Fluor 488. After fluorescence images were acquired, the neurobiotin staining was converted into a dark DAB reaction product, performed as previously described (Klausberger et al., 2003). This has advantages of being more sensitive than most fluorescent dyes, is permanent and not sensitive to photobleaching (Marx et al., 2012). In general we found similar results for calbindin immunohistochemistry as previous authors (Langston et al., 2010; Varga et al., 2010), who showed that the large majority (~90% in Peterson et al., 1996) of calbindin^{+} cells are glutamatergic neurons.

Anterograde and Retrograde Neuronal Labeling

Anterograde/retrograde tracer solutions containing either Biotinylated-Dextrane Amine (BDA) (10% w/v; 3.000 MW or 10.000 MW) or Cholera Toxin Subunit B, Alexa Fluor 488 Conjugate (CTB) (0.8 % in PB) were injected in juvenile rats (~150 gr) under ketamine/xylazine anesthesia. Briefly, a small craniotomy was opened above the targeted areas at intermediate positions along the septo-temporal axis. Animals were placed in a stereotaxic apparatus, and prior to injection, the area was localized by electrophysiological recordings, based on characteristic signatures of the local field potential and neuronal spiking activity. Glass electrodes with a tip diameter of 10-20 μm, filled with CTB or BDA solution, were then lowered unilaterally into the target region. Tracers were either pressure-injected (CTB; 10 injections using positive pressure of 20 p.s.i., 10-15 s injection duration) or iontophoretically-injected (BDA; 7s on/off current pulses of 1-5 mA for 15 min). After the injections, the pipettes were left in place for several minutes and slowly retracted. The craniotomies were closed by application of silicone and dental cement. The animals survived for 3-7 days before being transcardially perfused. The results from back-labeling agreed with previous authors (Germroth et al., 1989; Tamamaki and Nojyo, 1993; Peterson et al., 1996), who also found that the large majority of retrogradely-labeled neurons from the dentate gyrus had stellate morphologies.

Image Acquisition

A microscope equipped with a motorized stage and a z-encoder, was used for bright field microscopy. Images were captured using a MBF CX9000 camera using Neurolucida or StereoInvestigator. An epifluorescence microscope with camera was used to image the immunofluorescent sections. Alexa fluorophores were excited using the appropriate filters (Alexa 488 – L5, Alexa 546 – N3). Fluorescent images were acquired in monochrome, and colour maps were applied to the images post acquisition. Whole-mount stainings were imaged using a microscope. Fluorescence images were acquired with a 25x (1.05 NA) water-immersion objective. A femtosecond laser was used to excite fluorophores at 850 nm. Post hoc linear brightness and contrast adjustment were applied uniformly to the image under analysis.

4.2.2 Anatomy Analysis

Cell Counts and Patch Sizes

In the analysis for determining cell numbers and patch sizes, patches in consecutive sections were matched by overlaying them in Adobe Photoshop, and only the ones which could be reliably followed in all the sections under consideration were taken up for further analysis. Image stacks were first converted into .tiff files for different channels and focal planes using ImageJ. These files were then merged back together into a single file using the Neurolucida image stack module. In these patches all cells positive for Calbindin and NeuN were counted manually.

Quantification of patch sizes was done with the Neurolucida software by using the mean of maximum and minimum Feret diameter, defined as the maximum and minimum diameter of the patch, respectively. To correct for overestimation of neurons due to double counting in two adjacent sections, we estimated the number of cells in a section assuming uniform cell density and uniform spherical cell shape in the section and applied a correction factor of s/ (s+d) where, s is the section thickness and d is the diameter of a cell, to correct for the cells which would be counted again in an adjacent section.

Quantification of Axonal Orientation and Cholinergic Boutons

To quantify the orientation of axonal fibers in layer 1, axon segments from myelin-stained sections were traced using Neurolucida software. The polar histogram was constructed with angular bins of 3°, and the total length of axons in each angular direction was summed up.

Using Stereoinvestigator software we quantified the density of VAChT-positive puncta in calbindin patch and non-patch areas at the layer 1/2 border in tangential sections from five rats. In total, we selected 10 regions of interest (ROI) centered on calbindin patches and 10 ROIs positioned equidistant between calbindin patch centers. All VAChT positive puncta in the ROI were counted manually and divided by area size to obtain puncta density.

Analysis of Spatial Periodicity

To determine the spatial periodicity of calbindin$^+$ patches, we determined spatial autocorrelations and spatial Fourier spectrograms. The spatial autocorrelogram was based on Pearson's product moment correlation coefficient (as in Sargolini et al., 2006):

$$r(\tau_x,\tau_y)=(n\sum f(x,y)f(x-\tau_x,y-\tau_y)-\sum f(x,y)\sum f(x-\tau_x,y-\tau_y))/(\sqrt{(n\sum f(x,y)^2-(\sum f(x,y)^2)}\sqrt{(n\sum f(x-\tau_x,y-\tau_y)^2-(\sum f(x-\tau_x,y-\tau_y))^2))}$$

where, $r(\tau_x,\tau_y)$ is the autocorrelation between pixels or bins with spatial offset τx and τy. f is the image without smoothing or the firing rate map after smoothing, n is the number of overlapping pixels or bins. Autocorrelations were not estimated for lags of τ_x and τ_y, where n<20. Grid scores were

calculated as previously described by taking a circular sample of the autocorrelogram, centered on, but excluding the central peak. The Pearson correlation of this circle with its rotation for 60 degrees and 120 degrees was obtained (on peak rotations) and also for rotations of 30 degrees, 90 degrees and 150 degrees (off peak rotations). Gridness was defined as in as the minimum difference between the on-peak rotations and off-peak rotations. To determine the grid scores, gridness was evaluated for multiple circular samples surrounding the center of the autocorrelogram with circle radii increasing in unitary steps from a minimum of 10 pixels more than the width of the radius of the central peak to the shortest edge of the autocorrelogram. The radius of the central peak was defined as the distance from the central peak to its nearest local minima in the spatial autocorrelogram. The grid score was defined as the best score from these successive samples.

Grid scores reflect both the hexagonality in a spatial field and also the regularity of the hexagon. To disentangle the effect of regularity from this index, and consider only hexagonality, we transformed the elliptically distorted hexagon into a regular hexagon and computed the grid scores. A linear affine transformation was applied to the elliptically distorted hexagon, to stretch it along its minor axis, till it lay on a circle, with the diameter equal to the major axis of the elliptical hexagon. The grid scores were computed on this transformed regular hexagon.

The spatial Fourier spectrogram was calculated by implementing a two dimensional discrete Fourier transform and determining its power:

$$F(x,y) = \frac{1}{\sqrt{MN}} \sum_{n=0}^{N-1} \sum_{m=0}^{M-1} f(m,n)\, e^{-2\pi i\left(\frac{mx}{M} + \frac{ny}{N}\right)}$$

$$P(x,y) = \sqrt{F_r^2(x,y) + F_i^2(x,y)}$$

where, F is the spatial Fourier transform of f, which is a binary image representing the sample with regions of interest (patches) marked as white blocks, with the remaining area as black and zero padded to 2048 x 2048. M and N are the width and height of the image before zero-padding. Normalization by $\sqrt{MN}$ enables comparison of Fourier power in differently sized samples. P is the power of the Fourier transform with F_r and F_i being the real and imaginary parts of the Fourier transform.

To determine the probability that the patches present in the selected area would be arranged hexagonally, we employed a shuffling procedure and compared the maximum Fourier power of the block pattern representing the original image, to the 99th percentile of the power of a shuffled one with the same blocks (representing the patches) being randomly distributed in the same area without overlapping. This shuffling was performed on all samples on a sample-by-sample basis until the 99th percentile of the maximum power Fourier component converged to a constant.

4.2.3 Electrophysiology Methods

Anesthetized Juxtacellular Recordings

Juxtacellular recordings in anesthetized animals were performed under ketamine/urethane anesthesia, essentially as previously described (Klausberger et al., 2003). The ketamine/urethane mix is the anesthetic of choice for studying temporal dynamics of spiking activity, and it has long been used to study many aspects of hippocampal and entorhinal physiology (Klausberger et al., 2003; Quilichini et al., 2010). In a subset of recordings, scopolamine was injected systemically (0.4-1 mg/ml, i.p.; Tsuno et al., 2013). After a pre-injection baseline recording of ~5 min, scopolamine was injected and the effect on the recorded cell's activity monitored for further 15-20 min.

The juxtacellular signals were amplified by the ELC-03XS amplifier (NPI Electronics) and sampled at 20 kHz by a data-acquisition interface under the control of PatchMaster 2.20 software (HEKA). The animal's location was automatically tracked at 25 Hz by a videotracking system (Neuralynx).

Detailed Experimental Procedures of Freely-moving Juxtacellular Recordings

Animal Behavioral Training (7-10 days)

1| Progressively familiarize a male Wistar rat (~130-250 g body weight; see Materials) to the experimenter and the restrainer box for at least 3 days. To do this, handle the rat and let it explore the restrainer box in their home cages a few times per day. One/two days before starting the training (Step 2), habituate the rat to chocolate by adding a few crumbs to their regular food pellets.

2| Train the rat to chase randomly scattered food pellets inside a behavioral arena ("pellet-chasing" foraging task; Muller et al., 1987) by placing the animal in the behavioral arena, and throwing small chocolate crumbs randomly to initiate/motivate pellet chasing and running. Perform short training sessions (5-10 min) multiple times per day.

During training, animals receive unlimited access to food in the experimental arena and a limited food allowance in their cage. Monitor daily the rat's body weight. Under this food regime, animals should consistently maintain > 90% of their ad-libitum body weight; this provides the necessary motivation to the rat to actively engage in the behavioral training.

On initial training sessions, animals typically make only short excursions into the environment from their "home base" location (typically one corner of the arena) by moving along the walls. As training proceeds, this behavior will be slowly replaced by longer excursions eventually crossing the center of the arena. Keep low light conditions in the room and test animals in their dark phase for optimal behavioral performance. Provide a chocolate reward after each training session in their home cage. Reward with larger chocolate pellets when runs across the center of the arena are made.

3| Continue to train the animal until behavioral performance is satisfactory. For the specifics of our experimental design this corresponds to continuous running periods of ~20-30 min. This is typically achieved within 3-7 days by multiple (typically up to 4) training sessions per day of progressive durations.

Progression to the following steps can be delayed by a few days by keeping the rat at steady-state behavioral performance.

Behavior is a critical parameter for the success of the experiment. Daily training sessions at regular times should be performed to maintain the rat at steady-state performance.

Implantation and Animal Recovery (3-6 days)

4| Anesthetize the animal with an intraperitoneal injection of ketamine/xylazine (80-100 mg/kg ketamine; 10 mg/kg xylazine, see Reagent Setup) according to standard procedures.

5| Place the animal on a heating pad and fix the head in the stereotaxic apparatus. Using hair trimmers, shave the scalp above the area of interest.

6| Inject a local anesthetic (e.g., lidocaine or bupivacaine) subcutaneously into the scalp, and gently cover both eyes with ophthalmic cream to prevent drying.

7| Use forceps to lift the scalp and scissors to cut and remove a circle of skin. Both lambda and bregma points on the skull should be made visible. Scrape off connective tissue with a delicate bone scraper by applying gentle pressure. This step and steps 8-14 should be performed under stereomicroscopic guidance.

Minimal bleeding may occur at this point on the skull surface. Clean thoroughly with Ringer solution, and use cotton/surgery absorbent swabs for drying/cleaning the surface. Proceed to the next step only when bleeding has stopped.

8| Rinse the clean skull surface, and let it dry (typically 3-5 min; the bone will appear opaque). Mark your stereotaxic reference point (lambda or bregma) with a permanent marker. It will be used as a reference point for localizing the craniotomy site (step 19).

9| Apply a thin layer of adhesive (e.g., 3M ESPE; see Reagents) to the nearly dry skull. Cure the adhesive by ultraviolet (UV) light (follow guidelines from the producer). Protect your eyes from the UV light by means of UV-protection glasses.

The glue layer provides a base for the dental acrylic to adhere to. The skull surface should be dry and clean from blood before applying the glue (see next step). Traces of blood will prevent glue polymerization and compromise the adherence of the implant to the skull.

10| After UV curing the adhesive, clean the polymerized surface thoroughly with the help of a cotton swab. The polymerized adhesive should appear as a compact, resistant layer.

11| Use a stereotaxic atlas (Paxinos and Watson, 2006) to determine the coordinates of the brain region of interest. The marked bregma (or lambda) point is still visible through the thin transparent layer of polymerized adhesive. Mark the position for the center of the craniotomy. Use a permanent marker to mark the location for drilling.

12| Glue the recording chamber (see Reagent Setup) onto the exposed skull with adhesive (e.g., 3M ESPE; see Reagents). Seal the recording chamber edges with solid glue from 3M ESPE, in order to avoid leakage of the dental cement into the chamber (see step 13 below). Fill the recording chamber with silicone sealant.

13| Mix the dental cement and solvent in a weigh dish until it is slightly thickened and carefully pour the cement onto the skull and wound margins.

Dental cement powder and fumes are irritant and toxic. We recommend this step to be performed under a fume extractor (follow the producer's guidelines for proper use). Avoid the dental cement to enter the recording chamber.

14| Allow the cement to harden. Repeat step 13 for cementing the head-post posteriorly and the shielded protection cap anteriorly.

15| Release the rat from the stereotaxic frame and allow the animal to recover on the heating pad. Then return it to its cage for recovery under observation. Apply postoperative antibiotics and analgesics (i.e. Rimadyl) and follow standard surgical recovery procedures.

Animal behavior and recovery should be closely monitored. Allow the rat to fully recover from the surgery (typically 2-5 days) before proceeding to the next step.

Habituation to Head-fixation and Training (4-6 days)

16| Start to habituate the animal to the head-fixation by placing the animal in the restrainer box, and securing the head-post to the head-post holder (**Figure 3A**, bottom). This first fixation should not last more than 30 s-1 min. The animal is then placed back in its home cage, where a food reward (i.e. chocolate crumbs) is provided for positive reinforcement.

Perform the fixation of the head-post to the holder rapidly. On the first session, rats might exhibit overt signs of stress (i.e. vocalization, struggling, defecation). However, these signs will gradually disappear during habituation, and will typically be virtually absent after 2-3 days. Food reward is used as positive reinforcement for establishing an appetitive link and minimizing negative associations (Schwarz et al., 2010). Control body weight daily. Animals should not lose weight during the habituation procedure.

17| Slowly extend the fixation time over a number of days (2-3 sessions per day; the number of sessions and the increment in time between sessions should be adapted to the animal behavioral

response to fixation). Always provide food reward at the end of the session for positive reinforcement. From the second/third session onwards, upon release from fixation, place rats in the behavioral arena, where the chocolate reward is provided. Slowly re-initiate training to pellet chasing and running until pre-surgery behavioral performance is reached (as outlined in steps 1-3).

18| When the animal can sit quietly under head-fixation - i.e. without struggling and/or displaying overt behavioral signs of stress - for a minimal period of 15 min (this is typically achieved within 2-3 days), gradually present other individual aspects of the final recording situation; gradually habituate the animal to the lights/noise of the setup equipment (i.e. the stepping sound of the micromanipulator), the headstage, cables and LED lights while running (a dummy headstage with LEDs can be used for this purpose). The aim is to gradually habituate the rats to the final recording configuration by trying to mimic it as closely as possible during training (Schwarz et al., 2010). This typically requires an additional 2-3 days.

It is important that the steps and manipulations always follow the same order. Gradual habituation to the final recording situation is essential to minimize stress and improve behavioral performance during the recording experiment (see below).

Juxtacellular Recording and Labeling (1-2 days)

19| Anesthetize the rat with isoflourane and fix the animal's head firmly by securing the head-post to the holder. Remove the silicone plug from the recording chamber, and perform a small craniotomy under stereomicroscopic guidance. Use a small drill bit (e.g., 0.45 mm diameter) to drill a circular groove (1.5–2.0 mm diameter) until the bone at the edges starts to break. Use fine forceps to lift away the circular piece of bone in one piece. This step and steps 20-22 should be performed under stereomicroscopic guidance.

Avoid drilling across the bone as this might cause excessive bleedings. After removing the bone, the dura should appear intact and no bleeding should occur.

20| If you need to remove the dura, apply two drops of bupivacaine to the dura surface, and wait 3-5 min before washing thoroughly with Ringer solution. Remove the dura with the help of fine forceps, after making an incision with a hypodermic needle (e.g., 25 Gauge). Gently clean the exposed cortex with Ringer solution to remove blood. Usually, craniotomy-induced bleeding stops within 2–3 min.

Once the dura is removed, keep the brain surface from drying out. Removing the dura is not essential for obtaining juxtacellular recordings, as in young animals the dura can easily be penetrated by the electrode; removing the dura might however increase the chances of obtaining stable juxtacellular configurations, as the pipette enters the brain more cleanly.

21| If it is necessary to target the exact location and depth, map the location of the target region by recording local field potential/multiunit activity with a low-resistance electrode (e.g., Tungsten or glass-electrode, 0.5-1 MΩ) and a conventional headstage. Depending on the target brain area - and especially for deep brain structures, which are typically more difficult to target based solely on stereotaxic coordinates - this procedure might be necessary for fine tuning the exact target location and depth.
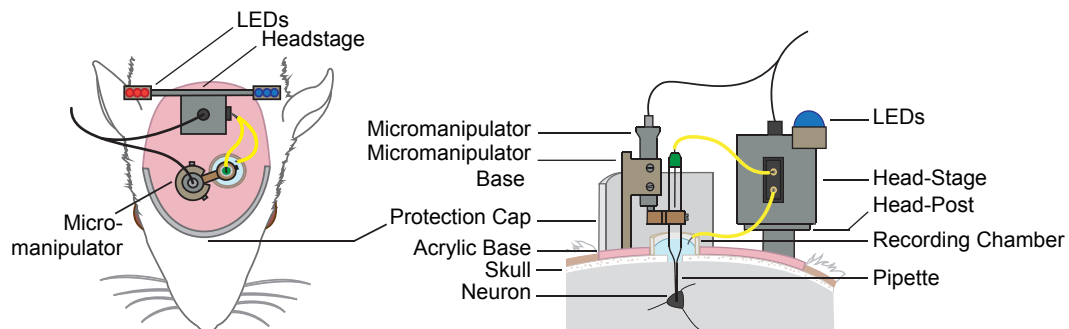
Figure 4: Assembled implant for juxtacellular recordings in freely moving animals. Schematic diagram showing the position of the individual implant components relative to the rat's head (left, top view; right, side view). Adapted from Tang et al., 2014a.

22| Screw the miniaturized micromanipulator on the base, and insert a sham pipette. By means of a manual stereotaxic manipulator (**Figure 3B**) place the pipette tip in the center of the craniotomy. Once the pipette is in the correct position, cement the micromanipulator's base in place by adding a thick layer of dental cement.

Tightly secure the micromanipulator's adaptor (see Equipment and **Figure 3B**) to avoid undesired movements of the pipette tip from its target position during hardening/shrinking of the dental cement.

23| Once the dental cement has hardened, release the micromanipulator / base assembly by unscrewing the adaptor piece (**Figure 3B**). Then release the micromanipulator by unscrewing the four screws on the base (**Figure 3**). Only the base remains cemented in place.

24| Seal the craniotomy with a layer of silicone sealant, and place the animal in the cage for recovery for > 4 hours.

Isofluorane anesthesia is associated with rapid animal recovery. We typically let the animals recover in their home cage for 4-24 hours before proceeding to the next step. For times longer than 24 hours, apply a drop of antibiotic agent (Mitomycin, see Reagent Setup) to the brain surface to minimize the occurrence of tissue regrowth and infections.

25| After recovery from isoflourane anesthesia (see step 24), head-fix the animal following the

same procedue used during training (step 16). Under stereomicroscopic guidance, remove the silicone plug from the craniotomy, evaluate the brain surface and, if necessary, clean the brain exposure.

The brain surface should appear clean. If tissue regrowth or signs of infections are observed (typically only for times longer than 24 hours after the craniotomy), carefully clean the exposure with ringer solution and surgery cellulose swabs. Avoid touching directly the brain surface, as this can potentially result in tissue damage.

26| Assemble the full recording implant (**Figure 4**) by first fixing the miniaturized head-stage on the head-post with a thin layer of instant glue (cyanoacrylate). Then fill a pipette (**Figure 3C**) with pipette solution (see reagent setup), and shorten it to approx. 2-3 cm total length by cutting the glass with a glass-cutting file. Insert the pipette in the micromanipulator and secure the micromanipulator onto the head-mounted base (**Figure 3B**).

27| Position the electrode wire inside the glass pipette, fix it with a tiny drop of silicone sealant and place the reference wire into the recording chamber. By operating the micromanipulator, slowly advance the pipette under high-magnification stereomicroscopic guidance until it touches the surface of the brain. This position can be taken as a reference for visually estimating the recording depth (see next step).

28| Advance the glass pipette into the brain by means of the micromanipulator, until the electrode tip reaches (or is close to) the target area.

The linear micromanipulator is not equipped with an absolute depth reader (Lee et al., 2006), as this would increase the mass and weight of the device. The desired recording depth, obtained from stereotactic atlas (Paxinos and Watson, 2006) and/or mapping experiments (step 21), is estimated by visually monitoring the distance travelled on the micromanipulator while the animal is head-fixed. Additionally, if the target area has characteristic electrophysiological signatures (i.e. ripples/sharp-wave complexes and complex spiking activity in the pyramidal layer of the CA1 region of the hippocampus (Lee et al., 2009); nested theta-gamma activity in the medial entorhinal cortex (Mizuseki et al., 2009)), they can be monitored on-line in current-clamp configuration while advancing the electrode, and can be used as an additional readout for localizing the target recording site.

29| Fill the recording chamber with a 3% agarose solution (see Reagent Setup) by gently applying it with large syringe needle (e.g., 20 Gauge). Use agarose solution similar to the animal's body temperature.

30| If you are going to perform a long recording session (> 2 hours) consider covering the agarose layer with a thin layer of bone wax or silicone, as this prevents drying of the agarose. Avoid thick layers of bone wax / silicone, as these might compromise the stepping performance of the micromanipulator.

31| Release the rat from head-fixation and place it in the behavioral arena.

32| Randomly throw chocolate crumbs in the behavioral arena. While the rat is foraging and actively running, try to establish a juxtacellular recording in the target region by slowly stepping down the micromanipulator (approximately 1 step every 2-3 seconds; micromanipulator settings should be adjusted in order to obtain 2-4 µm step size). Continuously monitor the electrode tip resistance on the oscilloscope by applying small negative current pulses (i.e. -0.5 nA, 200 ms long every 2-3 s). The establishment of a juxtacellular configuration is signaled by ~2-3 times increase in tip resistance and high signal-to-noise ratio of the spike signals (juxtacellular spike amplitude typically > 2 mV peak-to-peak).

Closely monitor the quality of the juxtacellular recording. This is done by monitoring the unfiltered raw signal and look for signs of cellular damage (i.e. negative DC shifts, spikes becoming broader and/or displaying an "intracellular-like" shape). Quickly discard recordings where cellular damage occurs, in order to avoid accidental staining of neurons. Current pulses for monitoring electrode resistance should have negative polarity, to avoid spillover of the positively charged Neurobiotin.

Head-shaking is a major mechanical disturbance which can lead to the loss of recording. While animals are actively engaged in foraging for food pellets, head-shaking rarely occurs. The occurrence of head-shaking can be minimized by injecting small volumes of lidocaine in the neck region, to minimize the discomfort of the head-implant.

33| If a stable juxtacellular recording is established and is maintained for a sufficient time for the animal to sample the surface of the 1 x 1 m arena, attempt juxtacellular labeling. This is done by modulating the cell's firing rate (i.e. "entrainment") by injecting typically 5-20 nA square current pulses (50% duty cycle: 200 ms ON, 200 ms OFF). The average duration of the labeling procedure in freely-moving animals is 1-3 min. Successful labeling during the entrainment procedure is signaled by broadening of the spikes and small negative DC shifts in the baseline potential. Further details of how to perform juxtacellular labeling can be found in (Deschênes et al., 1994; Pinault, 1994, 1996).

Juxtacellular labeling requires close proximity of the pipette tip to the recorded neuron. Attempt the labeling if large amplitude peak-to-peak spike signals (> 2 mV) and biphasic action potential shapes are observed, which are indicative for a close somatic/perisomatic location of the recording pipette tip (Herfst et al., 2012).

According to our experience, juxtacellular labeling is typically more difficult in an animal that is actively running compared to a resting animal, possibly because of higher mechanical instability of the juxtacellular configuration during active running. To circumvent this problem and maximize the success rate of labeling, give a large food pellet to the animal, so to keep it stationary while labeling is

attempted. If the juxtacellular recording is accidentally lost during labeling, quickly perfuse the animal (Step 37), as this might improve the chances of recovering the soma and proximal dendrites of the labeled cell.

34| Upon successful juxtacellular labeling, slowly retract the electrode.

Upon electrode retraction, monitor the spiking activity of the recorded cell. Spike shapes and firing rates should return to pre-labeling levels. This is to ensure that the transient membrane pores generated upon labeling have resealed and the cell is viable.

35| If desired, perform a second penetration for recording and labeling a second neuron in the target region by repeating steps 27-32. Head-fix the animal and release the micromanipulator from its base and replace the electrode with a new one.

Ensure that the two penetrations can be unequivocally assigned by post-hoc histological analysis. Rotate the micromanipulator within its anchoring base, to ensure that the electrode penetrates in a different location. Note the relative position of the electrode penetration compared to the previous one.

36| Head-fix the animal and remove the head-stage and the micromanipulator from the implant. Seal the craniotomy with silicone and place the animal back in its home cage for a sufficient time to allow complete filling of the recorded cell (typically > 2 hours). For assessment of dendritic morphology, shorter times (20-30 min) are typically sufficient.

37| Euthanize the animals by overdose injection of anesthetics (e.g., pentobarbital; i.p.). Perfuse the brain transcardially with saline followed by a 4% (wt/vol) paraformaldehyde solution, using standard methods.

38| Remove the brain and store it overnight at 4°C in a 4% paraformaldehyde solution. Afterwards, transfer the brain into a phosphate-buffered (PB) solution. The brain can be stored in the paraformaldehyde solution for up to 2-3 days, and afterwards for up to 1-2 weeks in PB solution. Longer storage times may decrease the quality of the subsequent stainings.

39| Slice the brain with a vibratome (e.g., into 100-150 μm thick sections) or cryostat (e.g., into 40-60 μm thick sections) and then process the slices with standard methods, based on the avidin-biotin binding reaction, for visualizing the Neurobiotin-filled cell morphology. Either the diaminobenzidine (DAB) chromogen, which produces a dark brown reaction product or fluorophores (i.e. streptavidin conjugated to Alexa 546) can be used for revealing the cell morphology. Further details on Neurobiotin detection methods can be found in (Horikawa and Armstrong, 1988; Huang et al., 1992; Marx et al., 2012). Reconstruct the 3D neuronal morphology with dedicated computer software (e.g. Neurolucida).

Tetrode Recordings

Tetrode recordings were obtained as previously described in detail (von Heimendahl et al., 2012). Tetrodes were turned from 12.5 μm diameter nichrome wire (California Fine Wire Company) and goldplated to ~250 kΩ impedance. Spiking activity and local field potential were recorded at 32 kHz (Neuralynx). Local field potential for theta phase assignment was recorded from the same tetrode as single units, relative to one tetrode left in superficial cortex. All recordings were done in a 1x1m box with behavioral training tasks same as juxtacellular procedures. The animal's location and head-direction was automatically tracked at 25 Hz by video tracking and head-mounted LEDs, as described above. After recordings, tetrode tracks were lesioned and the animal was trancardially perfused. The brain was sectioned tangentially and recording sites assigned by histology. Spikes were pre-clustered using KlustaKwik (K.D. Harris, Rutgers University) and manually using MClust (A.D. Redish, University of Minnesota). Cluster quality was assessed by spike shape, ISI-histogram, L-ratio and isolation distance, as previously described (von Heimendahl et al., 2012). Putative interneurons were identified based on firing rate, spike shape and ISI-histogram and were excluded from classification.

4.3   Data Analysis

Analysis of Theta Rhythmicity

The position of the rat was defined as the midpoint between two head-mounted LEDs. A running speed threshold (1 cm/s) was applied for isolating periods of rest from active movement. Theta-rhythmicity of spiking discharge was determined from the Fast Fourier Transform–based power spectrum of the spike-train autocorrelation functions of the cells, binned at 10ms. To measure modulation strength in the theta band (4-12 Hz), a theta-index was computed (Boccara et al., 2010), defined as the average power within 1 Hz of the maximum of the autocorrelation function in the 4-12 Hz, and divided by the average power in the 3-125 Hz range, or a theta-power without dividing. Only cells with mean firing rate > 0.5 Hz were included in the theta analysis, since low firing rates impede detection of firing rhythmicity (Barry et al., 2012b). Statistical significance was assessed by two-tailed Mann-Whitney nonparametric test with 95th confidence intervals.

Analysis of Theta Phase Locking

For all cells, we calculated the locking to theta phase based on spiking discharge in relation to theta rhythm in the local field potential. The local field potential was zero-phase band-pass filtered (4-12 Hz) and a Hilbert transform was used to determine the instantaneous phase of the theta wave. The strength of locking to theta phase, S, and the preferred phase angle, φ, was defined as the modulus and argument of the Rayleigh average vector of the theta phase at all spike times. Only spikes during

running (speed cutoff = 1 cm/s for juxtacellular signals, 5 cm/s for tetrode recordings) were included in the analysis. Only cells with mean firing rate > 0.5 Hz were included in the analysis (Barry et al., 2012b). Both the analysis procedures and the juxtacellular data set largely correspond to our recent publication (Ray et al., 2014), whereby a more stringent band-pass filtering was applied in a subset of cells.

Neurobiotin Labeling and Calbindin Immunohistochemistry

For histological analysis of juxtacellularly-labeled neurons, neurobiotin was visualized with streptavidin conjugated to Alexa 546 (1:1000). Subsequently, immunohistochemistry for Calbindin was performed as previously described (Ray et al., 2014) and visualized with Alexa Fluor 488. After fluorescence images were acquired, the neurobiotin staining was converted into a dark DAB reaction product. Neuronal morphologies were reconstructed by computer-assisted manual reconstructions (Neurolucida).

Spine Density Measurement

To assess the spine density of calbindin$^+$ and calbindin$^-$ dendrites, we labeled neurons in vivo juxtacellularly and identified the cells based on their calbindin immunoreactivity. We counted spines of fluorescent and DAB converted cells (10 calbindin$^+$ and 10 calbindin$^-$ neurons) at 50 μm, 100 μm and 150 μm from the soma. The spine counts were normalized by dendritic length to obtain the number of spines per μm.

Analysis of Spatial Modulation

The position of the rat was defined as the midpoint between two head-mounted LEDs. A running speed threshold (see above) was applied for isolating periods of rest from active movement. Color-coded firing maps were plotted. For these, space was discretized into pixels of 2.5 cm x 2.5 cm, for which the occupancy z of a given pixel x was calculated as

$$z(x) = \sum(t)(w|x-x_t|)\Delta t$$

where xt is the position of the rat at time t, Δt the inter-frame interval, and w a Gaussian smoothing kernel with τ = 5 cm.

Then, the firing rate r was calculated as

$$r(x) = (\sum(i)(w|x-x_i|))/z$$

where x_i is the position of the rat when spike i was fired. The firing rate of pixels, whose occupancy z was less than 20 ms, was considered unreliable and not shown.

To determine the spatial periodicity of juxtacellularly recorded neurons, we determined spatial autocorrelations. The spatial autocorrelogram was based on Pearson's product moment correlation coefficient:

$r(\tau_x,\tau_y)=(n\sum f(x,y)f(x-\tau_x,y-\tau_y)-\sum f(x,y)\sum f(x-\tau_x,y-\tau_y))/(\sqrt{(n\sum f(x,y)^2-(\sum f(x,y)^2)}\sqrt{(n\sum f(x-\tau_x,y-\tau_y)^2-(\sum f(x-\tau_x,y-\tau_y))^2)})$

where, $r(\tau_x,\tau_y)$ the autocorrelation between pixels or bins with spatial offset τ_x and τ_y. f is the image without smoothing or the firing rate map after smoothing, n is the number of overlapping pixels or bins. Autocorrelations were not estimated for lags of τ_x and τ_y, where n < 20. For spatial and head-directional analysis, both a spatial (> 50% spatial coverage) and a firing rate inclusion criterion (> 0.5 Hz) were applied. Spatial coverage was defined as the fraction of visited pixels (bins) in the arena to the total pixels.

Analysis of Spatial Information

For all cells, we calculated the spatial information rate, I, from the spike train and rat trajectory:

$I=1/(T \int r(x)\log_2(r(x)/r)o(x)dx)$

where r(x) and o(x) are the firing rate and occupancy as a function of a given pixel x in the rate map. r is the overall mean firing rate of the cell and T is the total duration of a recording session (Skaggs et al., 1993). A cell was determined to have a significant amount of spatial information, if the observed spatial information rate exceeded the 95th percentile of a distribution of values of I obtained by circular shuffling. Shuffling was performed by a circular time-shift of the recorded spike train relative to the rat trajectory by a random time $t'\in]0,T[$ for 1000 permutations (von Heimendahl et al., 2012; Bjerknes et al., 2014).

Analysis of Gridness

Grid scores were calculated as previously described (Wills et al., 2010; Barry et al., 2012a) by taking a circular sample of the autocorrelogram, centered on, but excluding the central peak. The Pearson correlation of this circle with its rotation for 60 degrees and 120 degrees was obtained (on peak rotations) and also for rotations of 30 degrees, 90 degrees and 150 degrees (off peak rotations). Gridness was defined as the minimum difference between the on-peak rotations and off-peak rotations. To determine the grid scores, gridness was evaluated for multiple circular samples surrounding the center of the autocorrelogram with circle radii increasing in unitary steps from a minimum of 10 pixels more than the width of the radius of the central peak to the shortest edge of the autocorrelogram. The radius of the central peak was defined as the distance from the central peak to its nearest local minima in the spatial autocorrelogram. The radius of the inner circle was increased in unitary steps from the radius of the central peak to 10 pixels less than the optimal outer radius. The grid score was defined as the best score from these successive samples. Grid scores reflect both the hexagonality in a spatial field and also the regularity of the hexagon. To disentangle the effect of regularity from this index, and consider only hexagonality, we transformed the elliptically distorted hexagon into a regular hexagon

and computed the grid scores (Barry et al., 2012a). A linear affine transformation was applied to the elliptically distorted hexagon, to stretch it along its minor axis, until it lay on a circle, with the diameter equal to the major axis of the elliptical hexagon. The grid scores were computed on this transformed regular hexagon (Barry et al., 2012a).

Analysis of Border Cells

To determine the modulation of a cell firing along a border, we determined border scores (Solstad et al., 2008). Border fields were identified from a collection of neighboring pixels having a firing rate higher than 0.3 times the maximum firing rate and covering an area of at least 100 cm (Sargolini et al., 2006). The coverage (Cm) along a wall was defined as the maximum length of a putative border field parallel to a boundary, divided by the length of the boundary. The mean firing distance (Dm) of a field was defined as the sum of the square of its distance from the boundary, weighted by the firing rate (Solstad et al., 2008). The distance from a boundary was defined as the exponential of the square of the distance in pixels from the closest boundary, normalized by half the length of the boundary. Border scores were defined as the maximum difference between Cm and Dm, divided by their sum, and ranged from -1 to +1.

Analysis of Head Direction

Head-direction tuning was measured as the excentricity of the circular distribution of firing rates. For this, firing rate was binned as a function of head-direction (n = 36 bins). A cell was said to have a significant head-direction tuning, if the length of the average vector exceeded the 95th percentile of a distribution of average vector lengths calculated from shuffled data and had a Rayleigh vector length > 0.3. Data was shuffled by applying a random circular time-shift to the recorded spike train for 1000 permutations.

Classification of Non-identified Cells into Putative Cell Types

For classification based on strength of locking to theta phase, S, and preferred theta phase angle, φ, we built a support vector machine using the built-in functions of the MATLAB Statistics Toolbox (The MathWorks Inc., Natick, MA, USA) using pairs of φ and S obtained from juxtacellular recording of identified cells. Because the phase angle is a circular variable, we trained the classifier on a space of the vectors (cos(φ)S, sin(φ)S), scaled to zero mean and unit variance using a gaussian radial basis kernel function with a scaling factor, sigma, of 1. To avoid cross-contamination of the two clusters, we employed a guard zone and excluded cells with a distance to the classification hyperplane < 0.1 from classification. Classifier robustness was evaluated using a bootstrapping approach. To test if the putative calbindin[+]/calbindin[-] border suggested by the classifier based on our limited set of identified cells would also correctly classify a large number of non-identified cells, we fitted the appropriate probability

density functions to the theta strength and phase angle of identified cells (beta distributions and circular Gaussian distributions, respectively) and generated 10.000 calbindin$^+$ and 10.000 calbindin$^-$ testing cells drawn from these distributions. Testing cells were classified and found to be classified 75.5% correctly for calbindin$^+$ cells and 86.7 % correctly for calbindin$^-$ cells (**Figure 19C**), suggesting that our classifier generally performes well and is not just overfitting our small dataset of identified cells from freely-moving rats. Assuming the prior distribution of ~53% calbindin$^+$ neurons, ~34% reelin$^+$ (calbindin$^-$) neurons and ~13% interneurons in layer 2 of the medial entorhinal cortex of a rat (**Figure 18A,B**), we estimate the purity (positive predictive value) of putative calbindin$^+$ and putative calbindin$^-$ cells assigned by our classifier to be 83% and 89%, respectively (**Figure 19D**). This gives us the final cell sample purity of our putative and identified dataset of 84% and 90% for calbindin$^+$ and calbindin$^-$ cells, respectively.

Classification of Cells into Functional Categories

Cells were classified as head-direction cells, grid cells, conjunctive cells, border cells and non-spatially modulated cells based on their grid score, border score, spatial information and significance of head-directionality according to the following criteria:

Head direction cells: Rayleigh vector length > 0.3 & significant head-direction tuning (Boccara et al., 2010).

Grid cells: Grid score > 0.3 & significant spatial information.

Border cells: Border score > 0.5 & significant spatial information (Solstad et al., 2008), or those who passed border test (Solstad et al., 2008; Lever et al., 2009).

Spatially irregular cells: significant spatial information (Bjerknes et al., 2014).

Non-spatially modulated cell: no significant spatial information.

In agreement with previous work (Solstad et al., 2008), few cells (n = 6) passed both the border cell and the grid cell threshold. These six cells were assigned to be grid cells by visual inspection.

5.   Results

5.1   Grid-Layout and Theta-Modulation of Layer 2 Pyramidal Neurons in Medial Entorhinal Cortex

Results in this chapter have been published (Ray et al., 2014).

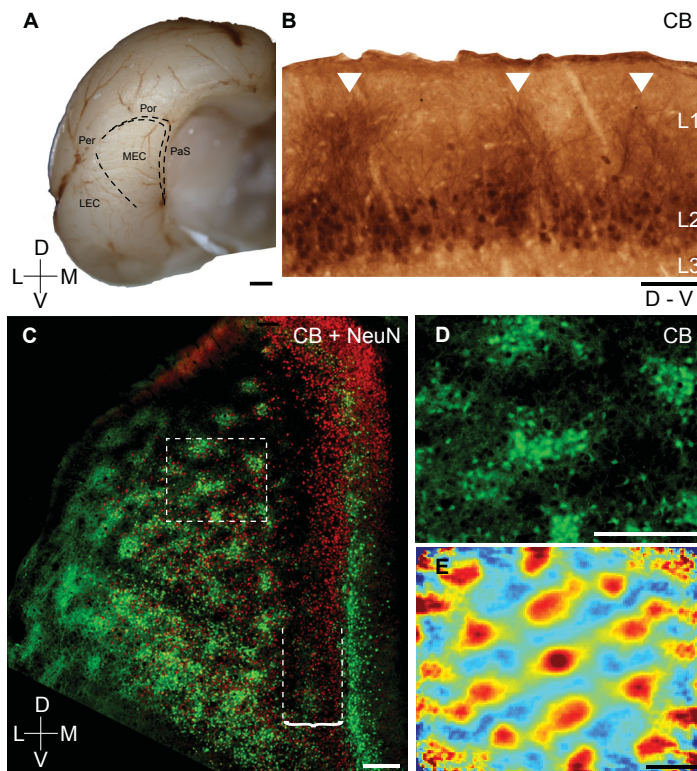### 5.1.1 Grid-like Arrangement of Calbindin⁺ Pyramidal Cells in the Medial Entorhinal Cortex

Figure 5: Grid-like arrangement of calbidin⁺ pyramidal cells in layer 2 of MEC. (A) Posterior view of a rat cortical hemisphere. LEC, lateral entorhinal cortex; PaS, parasubiculum; Per, perirhinal cortex; Por, postrhinal cortex. (B) Calbindinimmunoreactivity (brown precipitate) in a parasaggital section reveals patches with apical dendrites of calbindin⁺ pyramidal cells forming tents (white arrows) in layer 1. (C) Tangential section showing all neurons (red,NeuN-antibody) and patches of calbindin⁺ neurons (green). Bracket, dashed lines indicate the patch-free stripe of MEC. (D) Inset from (C). (E) Two-dimensional spatial autocorrelation of (D) revealing a hexagonal spatial organization of calbindin⁺ patches. Color scale, –0.5 (blue) through 0 (green) to 0.5 (red); grid score is 1.18. Scale bars, (A) 1 mm; (B) 100 mm; (C) to (E) 250 mm. D, dorsal; L, lateral; M, medial; V, ventral. Adapted from Ray et al., 2014.

Calbindin immunoreactivity (Varga et al., 2010) is a specific molecular marker that identifies relatively homogeneous the pyramidal neuron population in MEC layer 2. Parasagittal sections stained for calbindin (**Figure 5A,B**) confirmed early reports that calbindin-positive (calbindin⁺) pyramidal cells were arranged in patches (Fujimaru and Kosaka, 1996). Apical dendrites of calbindin⁺ pyramidal cells bundled together in layer 1 to form clusters and tent-like structures over the patches (**Figure 5B**). The patchy structure is most prominent at the layer 1/2 border, whereas in deep layer 2 this regularity of calbindin⁺ cell patches is less clear. Patch diameter increases from the upper layer 2 to middle layer 2. At the lower level of layer 2 there is no apparent modular structure of calbindin⁺ cells (**Figure 6**). By counting cell numbers we showed that in each patch, threre are 187 ± 70 cells (111 ± 42, ~60 % calbindin⁺, 76 ± 28, ~40 % calbindin⁻ cells; counts of 19 patches from four brains). To visualize these pyramidal cell patches in the cortical plane, we double-stained tangential entorhinal sections for

calbindin (green) and the neuronal marker NeuN (red). Calbindin⁺ (green/yellow) patches covered the MEC except for a 400-500 μm wide patch-free medial stripe adjacent to the parasubiculum (**Figure 5C**). Clusters of cells were not observed in calbindin⁻ neurons (red) (**Figure 5C**). However, a striking hexagonal organization of calbindin⁺ patches coud be ovserved (**Figure 5C,D**), which was further characterized by three techniques: (i) Two-dimensional spatial autocorrelation analysis (Hafting et al., 2005), to capture the recurring features and reveal a hexagonal regularity (**Figure 5E**). (ii) A modified grid score measurement (Sargolini et al., 2006) to quantify hexagonality also in elliptically distorted hexagons (Barry et al., 2012a), such distortions normally resulted from anatomical tissue curvature and anisotropic shrinkage. Grid scores range from -2 to +2, with values > 0 indicating hexagonality. The example in **Figure 5D** had a grid score of 1.18, suggesting a high degree of hexagonality. (iii) We assessed the probability of hexagonal patchy arrangements given preserved local structure (Krupic et al., 2012) by a shuffling procedure. We found that the strongest Fourier component of the sample (**Figure 5D**) exceeded that of the 99th percentile of shuffled data, suggesting such hexagonality is unlikely to arise by chance.

Figure 6: Cellular architecture of an individual calbindin patch. A, Side view of an optically-cleared patch of calbindin⁺ cells. Serial optical sections spaced 2 μm apart were taken along the x-z-axis and displayed as maximum intensity projection. **B-I,** Optical sections at the levels indicated in A, showing calbindin⁺ cells in green (B, D, F, H) and an overlay of calbindin⁺ cells in green and red autofluorescence showing all neurons (C, E, G, I). Dashed lines in A indicate the level of the optical sections displayed in (B-I): 70 μm below surface (B, C), 108 μm below surface D, E, 130 μm below surface (F, G) and 160 μm below surface (H, I). Scale bars: A = 50 μm; B = 50 μm, applies to B-I.

Adapted from Ray et al., 2014.

5.1.2 Calbindin⁺ Pyramidal but not Dentate-projecting Stellate Neurons Form Patches

To clarify the projection pattern of calbindin⁺ pyramidal cells, we retrogradely labeled neurons from ipsilateral dentate gyrus (**Figure 7A**) using biotinylated dextran amine (**Figure 7B**) or cholera toxin B (**Figure 7C**). Consistent with previous results with identified projection patterns and immunoreactivity (Varga et al., 2010), we also found that most retrogradely labeled neurons were stellate cells (Germroth et al., 1989; Tamamaki and Nojyo, 1993), with only a small fraction of cells with pyramidal morphologies, but these neurons appeared larger than typical calbindin⁺ pyramidal cells (**Figure 7B**). Calbindin⁺ neurons did not project to the dentate gyrus at all (only 1 double-labeled out of 313 neurons in **Figure 7C-E**; see also Varga et al., 2010). Thus, calbindin⁺ cells form hexagonally
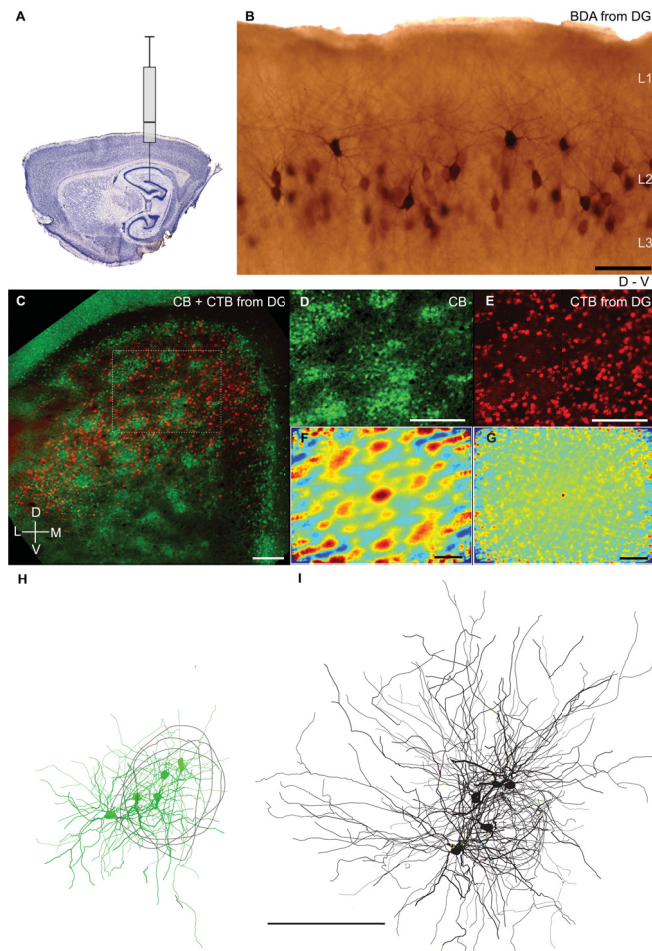
Figure 7: Calbindin⁺ pyramidal but not dentate-projecting stellate neurons form patches. (A) Schematic of retrograde labeling from dentate gyrus. **(B)** Such retrograde labeling (BDA, brown) stains neurons (most with stellate morphologies) in a parasaggital MEC section. **(C)** Tangential MEC section showing calbindin⁺ neurons (green) and retrogradely labeled neurons (red) after dentate gyrus choleratoxin B injection. **(D and E)** Insets from **(C)**. **(F)** Two-dimensional spatial autocorrelation of **(D)** reveals regular organization of calbindin⁺ patches; grid score is 0.32. The strongest Fourier component of the sample exceeded that of the 99th percentile of shuffled data confirming hexagonality. **(G)** Two-dimensional spatial autocorrelation of **(E)** reveals no spatial organization; grid score is –0.03. **(H and I)** Superimposed reconstructions of dendritic morphologies of 5 calbindin⁺ pyramidal (green) and 5 calbindin⁻ stellate neurons (black) in the tangential plane. Morphologies were "patch-centered" aligned according to orientation and the center of the nearest calbindin⁺ patch (gray outlines). Scale bars, **(B)** 100 mm; **(C)** to **(E)** and **(G)** to **(I)** 250 mm. D, dorsal; L, lateral; M, medial; V, ventral. Adapted from Ray et al., 2014.

arranged patches (**Figure 7C,D,F**), while dentate-gyrus projecting calbindin⁻ neurons (red) were uniformly distributed (**Figure 7E,G**). Reconstructions of calbindin⁺ and calbindin⁻ cells juxtacellularly labeled in vivo confirmed their pyramidal and stellate morphologies, respectively: Calbindin⁺ dendrites were largely confined to patches, whereas calbindin⁻ stellates cells had three times larger dendritic trees (7.6 vs 2.6 mm average total length, $p < 0.03$), which extended unrelated to patches (**Figure 7H,I**). Differentiating layer 2 neurons by calbindin and reelin immunoreactivity confirmed patchy hexagonality of calbindin⁺ cells and scattered distribution of reelin⁺ cells, forming two nonoverlapping
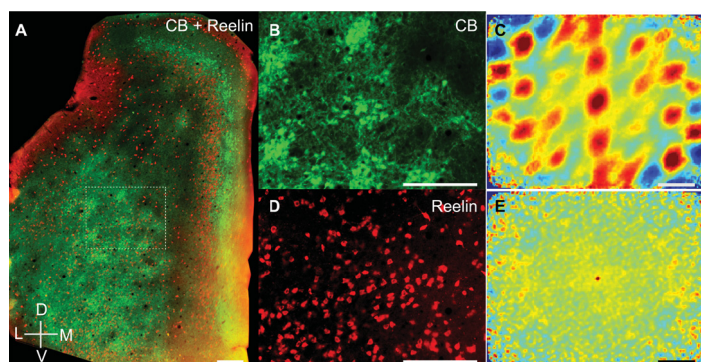
Figure 8: Calbindin⁺ pyramidal neurons but not reelin⁺ cells form patches. A, Tangential section of the rat MEC showing calbindin⁺ pyramidal neurons and neuropil (green) and reelin⁺, putative stellate, neurons (red). **B,** Inset from A showing a high magnification of calbindin⁺ patches. **C,** Two-dimensional spatial autocorrelation of calbindin⁺ patches shown in B. The grid score is 0.49. The strongest Fourier component of the sample exceeded that of the 99th percentile of shuffled data, confirming hexagonality. **D,** Corresponding image section from B showing reelin⁺ neurons. **E,** Spatial autocorrelation of reelin⁺ neurons shown in D. The grid score is -0.04. Scale bars: A-E = 250 μm. D = dorsal, L = lateral, M = medial, V = ventral. Adapted from Ray et al., 2014.

neuronal populations (2 double-labeled neurons in 168 calbindin[+] and 405 reelin[+] layer 2 neurons, **Figure 8**; Varga et al., 2010), and two-dimensional spatial autocorrelation illustrated regular spatial organization of calbindin[+] patches (**Figure 8B**) and a lack of spatial organization of reelin^{+} neurons.

5.1.3 Alignment of the Calbindin Grid to Parasubiculum, Layer 1 axons, and Cholinergic Markers

To investigate the organization of calbindin[+] patches across MEC, we prepared flattened whole-mount preparations. Patches had similar arrangements throughout the dorsoventral extent of MEC (**Figure 9**). At the layer 1/2 border we consistently observed hexagonal arrangements in well-stained specimen. We quantified patch size and spacing in ten largely complete MEC whole-mounts. Patch density was similar throughout MEC, while patch diameter slightly increased towards ventral (**Figure 9A**). Spatial autocorrelation also showed similar regular patterns in dorsal and ventral patch regions (**Figure 9B-D**). We estimated 69 ± 17 patches across the entire MEC (n = 10). Calbindin patches stained also positive for cytochrome-oxidase activity (Burgalossi et al., 2011). However, the two

Figure 9: Layout of calbindin patches across the extent of MEC. A, Measurements of mean patch diameter (red) and density (blue) across the dorsoventral extent of the MEC. Measurements refer to ten MEC whole-mounts and did not include the medial patch-free stripe of MEC (see Figure 5C). Error bars = SD. **B,** Tangential section from a flattened cortical preparation processed for calbindin immunoreactivity (green) showing modularity throughout the MEC. The image was flipped around the vertical axis for comparability. **C,** Two-dimensional spatial autocorrelation of the dorsal inset in A. The grid score is 0.32. The strongest Fourier component of samples C, D exceeded that of the 99th percentile of shuffled data confirming hexagonality. **D,** Two-dimensional spatial autocorrelation of the ventral inset in A. The grid score is 0.79. Scale bars: B-D = 250 μm. D = dorsal, L = lateral, M = medial, V = ventral. Adapted from Ray et al., 2014.

staining patterns were not the same as calbindin patches were more sharply delineated than spots revealed by cytochrome-oxidase-activity and cytochrome-oxidase staining revealed many more patches than calbindin staining in MEC (Burgalossi et al., 2011). Moreover, the staining patterns did not correspond at all in the parasubiculum.

Calbindin[+] patches shared 60° symmetry of their axes (**Figure 10A**). One axis runs parallel to the dorsoventral axis of the parasubiculum (**Figure 10A,B**). Lines fitted through the dorsoventral axis of the parasubiculum and the most medial column of calbindin[+] patches had the same orientation (**Figure 10B**). A second consistent axis was tilted about 60° relative to the dorsoventral axis. This calbindin[+] patch axis curved ventrally at more lateral positions and aligned with the orientation of

overlaying layer 1 myelinated axons (**Figure 10C-F**). Thus, the line connecting diagonally neighboring

calbindin patches (revealed by spatial autocorrelation, **Figure 10D,E**) aligned with the orientation of
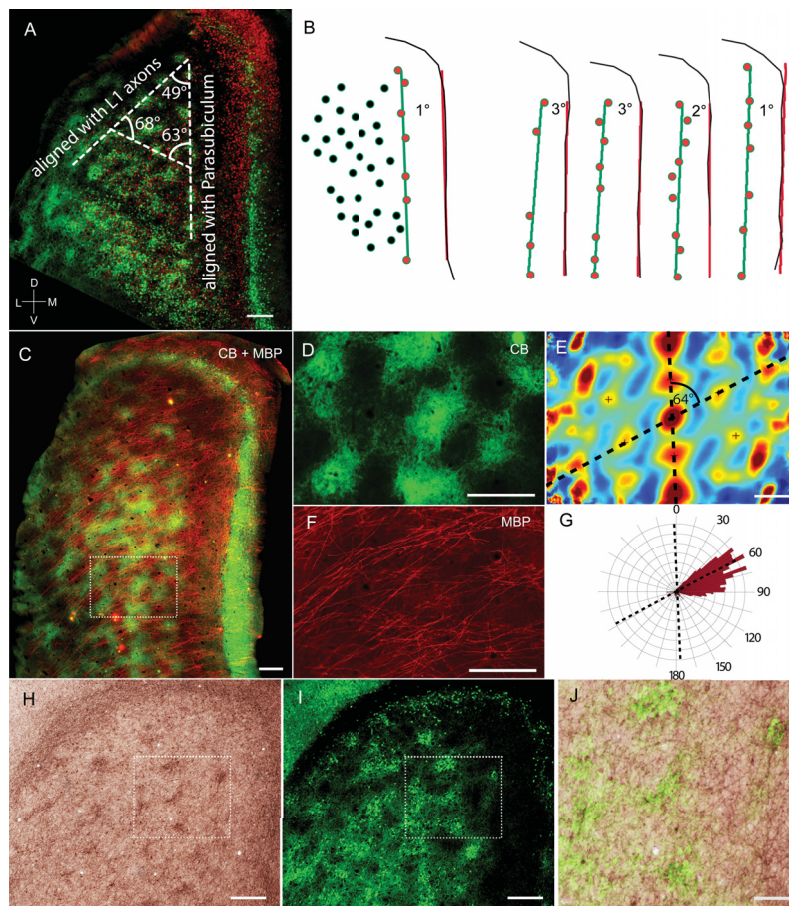

Figure 10: Alignment of the calbindin grid to parasubiculum, layer 1 axons, and cholinergic markers. (A) Section from Figure 5C. Dashed white lines indicate axes of the calbindin⁺ grid (angles are indicated). Axes aligned with parasubiculum (B) and layer 1 axons [(C) to (G)]. (B) (Left) Schematic of calbindin patches and parasubiculum from (A). The orange line fits the dorsoventral axis of the parasubiculum, and the green line fits the most medial column of patches (red); the angle between these lines is indicated. (Right) Fitted lines and their relative angles for four other brains. (C) Tangential section processed for calbindin (green) and myelin basic protein (red). (D) Inset from (C). (E) Two-dimensional spatial autocorrelation of (D). Dashed black lines indicate grid axes. (F) Inset from (C). (G) Axonal segments in (F) were manually traced from left to right, and we computed a polar plot (red) of the orientations of the axonal segments. The orientations of axonal segments aligned with one axis of the grid of calbindin patches [superimposed dashed lines from (E)]. (H) Tangential section stained for acetylcholinesterase activity. (I) Section from (H) costained for calbindin. (J) Overlay of (H) and (I) shows overlap between acetylcholinesterase and calbindin staining. Scale bars, (A), (C) to (F), (H), and (I) 250 mm; (J) 100 mm.D, dorsal; L, lateral; M, medial; V, ventral. Adapted from Ray et al., 2014.

layer 1 axons (**Figure 10F**). We quantified the orientation of axonal segments by a polar plot shown

in **Figure 10G** and confirmed that layer 1 axons share one main orientation in MEC (Blackstad,

1956; Witter et al., 1989; Burgalossi et al., 2011). Cholinergic transmission is of importance for MEC

function (Barry et al., 2012c; Heys et al., 2012) and grid cell activity (Brandon et al., 2011; Koenig et al., 2011; Newman et al., 2014). Staining of acetylcholinesterase also revealed a patch structure at the layer 1/2 border (**Figure 10H**), which colocalized with the cores of calbindin+ patches (**Figure 10H-J**).

Axonal terminals positive for the vesicular acetylcholine transporter (VAChT) were closely apposed to calbindin+ cells and their density was twofold larger in calbindin+ patches than between patches (**Figure 11A-C**). We also stained for M1 muscarinic receptors and observed a diffuse labeling without colocalization of these receptors with VAChT-puncta (**Figure 11E**). Moreover, we analyzed the apposition and distribution of presynaptic VAChT-puncta on a large number of in-vivo filled
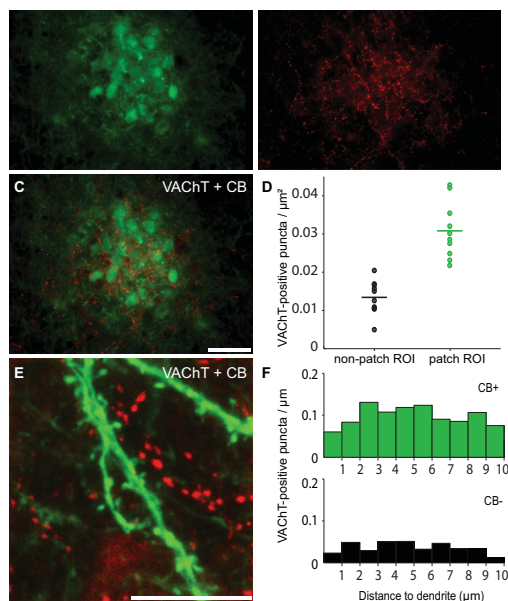

Figure 11: VAChT, calbindin patches and proximity of cholinergic boutons to calbindin+ dendrites A, Fluorescence micrograph showing one calbindin patch from a tangential section stained for calbindin (green). B, Same section as in A stained for VAChT immunoreactivity (red). C, Overlay of A and B. D, Density of VAChT-positive puncta in calbindin patches (green dots) and non-patch areas (black dots) at the layer 1/2 border. In five rats we selected 10 regions of interest (ROI) centered on calbindin patches and 10 ROIs positioned equidistant between calbindin patch centers. Horizontal bars indicate mean values. All VAChT positive puncta in the ROI were counted and divided by area size to obtain puncta density. E, Fluorescence micrograph showing an overlay of a calbindin+ dendrite (green) and nearby VAChT-positive puncta (red). F, Histogram of the closest distance of VAChT-positive puncta to dendrites of calbindin+ (top) and calbindin- (bottom) cells. We selected 35 dendritic segments of calbindin+ and 25 segments of calbindin- dendrites and measured the distance of VAChT-positive puncta and dendrites. The histograms were normalized by dendritic length to obtain the number of VAChT-positive puncta per μm. Data refer to 10 (5 each) juxtacellularly stained calbindin+ and calbindin- neurons. Scale bars: A, B, C = 50 μm; E = 10 μm. Adapted from Ray et al., 2014.

calbindin+ and calbindin- layer 2 cells by confocal microscopy. We find that VAChT-puncta are much more abundant around calbindin+ than calbindin- layer 2 cells, but ACh synapses do not seem to directly target calbindin+ cell dendrites, however (**Figure 11D-F**). Both the M1 receptor labeling and our dendrite-VAChT-puncta colocalization analysis are in line with a volumetric action of ACh in MEC.

5.1.4 Theta-modulation of Calbindin+ and Calbindin- Cells

Finally, we assessed in freely moving animals how activity of identified neurons related to the entorhinal theta-rhythm, with the method described above (see Methods; Tang et al., 2014a). We recorded 31 layer 2 neurons in rats trained to explore open fields, and classified them by morphology and immunoreactivity. Most calbindin+ neurons (n = 12) were pyramidal cells, while most calbindin- neurons (n = 19) had stellate morphologies. Firing rates were not different between two cell populations (calbindin+ = 2.1 ± 1.1 Hz; calbindin- = 2.3 ± 1.5 Hz; p > 0.5, Mann-Whitney test). Surprisingly,
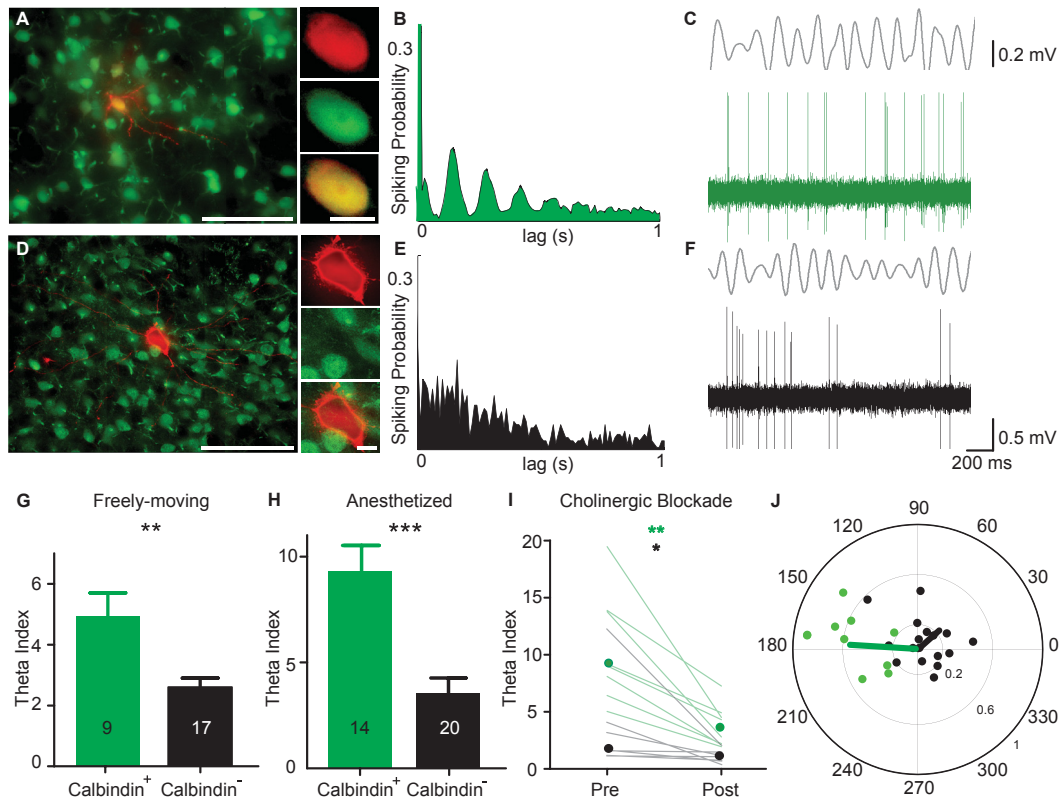
Figure 12: Theta-modulation of calbindin+ and calbindin− cells. (A) (Left) Micrograph (tangential section) of a calbindin+ neuron recorded in a freely moving animal. Green, calbindin; red, neurobiotin. (Right) Soma in red, green channel, and overlay. (B) Autocorrelogram of spike discharges for the calbindin+ neuron shown in (A). (C) Filtered (4 to 12 Hz) local field potential (top) and spiking pattern (bottom) of the neuron shown in (A). (D to F) Same as (A) to (C) but for a calbindin− neuron. (G) Strength of theta rhythmicity in calbindin+ and calbindin− neurons in freely moving animals. Numbers are n of neurons. Error bars indicate SEM. (H) Same as (G) but for recordings under urethane-ketamine anesthesia. (I) Theta-rhythmicity in calbindin+ neurons (green, n = 8) and calbindin− neurons (black, n = 7) under anesthesia before and after systemic cholinergic blockade with scopolamine (Wilcoxon signed rank test, P = 0.0078 for calbindin+, P = 0.0156 for calbindin− cells). Dots indicate medians. (J) Polar plot of preferred theta-phase (theta-peak = 0°) and modulation strength (Rayleigh vector, 0 to 1, proportional to eccentricity) for calbindin+ (green) and calbindin− (black); dots indicate single cells, and lines indicate averages. Scale bars, (A) and (D) 100 mm (left), 10 mm (right).calbindin− dendrites and measured the distance of VAChT-positive puncta and dendrites. The histograms were normalized by dendritic length to obtain the number of VAChT-positive puncta per μm. Data refer to 10 (5 each) juxtacellularly stained calbindin+ and calbindin− neurons. Scale bars: A, B, C = 50 μm; E = 10 μm. Adapted from Ray et al., 2014.

calbindin+ neurons (**Figure 12A-C**) showed much stronger theta-rhythmicity than calbindin− cells (**Figure 12D-G**; p < 0.01, unpaired t test). Theta-rhythmicity was associated with locomotion of the animal (**Figure 13**). When the animal started to move, prominent theta oscillatory patterns in LFP and theta rhythmic firing of calbindin+ cells could be observed (**Figure 13A-C**). Both calbindin+ and calbindin− neurons showed movement dependency; however, calbindin+ neurons showed much stronger movement dependency of theta-rhythmicity (**Figure 13D,E**). A similar twofold difference in theta-rhythmicity between calbindin+ (n = 14) and calbindin− cells (n = 20) was observed under urethane-ketamine anesthesia (**Figure 12H**; p = 0.0003, Mann-Whitney test), which preserves cortico-hippocampal theta-rhythmicity (Klausberger et al., 2003; Quilichini et al., 2010).
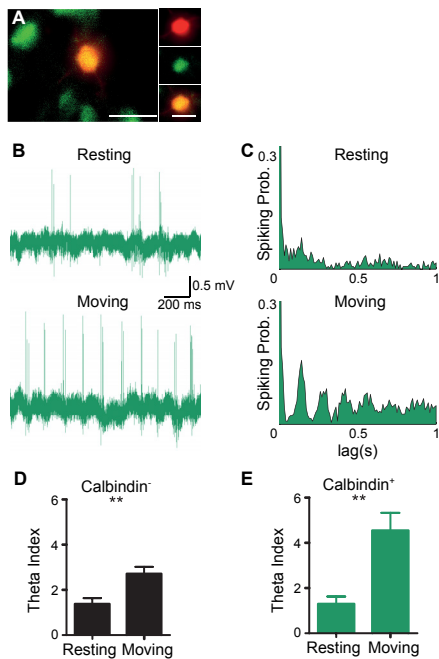
Figure 13: Movement dependency of theta-rhythmicity calbindin⁺ neurons. A, Fluorescence micrograph of a representative calbindin⁺ layer 2 neuron recorded from a freely moving rat. Green: calbindin, red: Neurobiotin. Scale bars: 100 μm (left) and 10 μm (right). **B,** Representative raw juxtacellular traces from the calbindin⁺ neuron shown in A under resting (top) and moving state (bottom). **C,** Spike autocorrelograms of the calbindin⁺ neuron shown in A under resting (top) and moving state (bottom). **D,E** Population average of the strength of theta-rhythmicity (theta index; see Methods) under resting and moving state in calbindin⁻ (D) and calbindin⁺ neurons (E) P = 0.0034 (left panel, n = 17) and 0.0036 (right panel, n = 9), Mann-Whitney test. Error bars = SEM. Adapted from Ray et al., 2014.
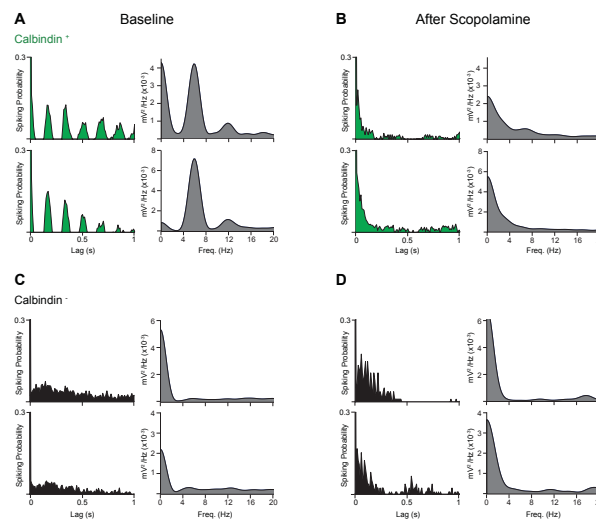

Figure 14: Effects of blockade of cholinergic transmission by scopolamine in individual neurons. Spike autocorrelograms (first and third column) and power spectra of spike discharges (second and fourth column) before (baseline) and after systemic cholinergic blockade with scopolamine. **A,B,** Two representative calbindin⁺ neurons. **C, D,** Two representative calbindin⁻ neurons. Adapted from Ray et al., 2014.

To investigate the involvement of cholinergic inputs in theta-rhythmicity, we blocked cholinergic transmission by systemic injection of scopolamine under anesthesia, and found that theta rhythmicity was severely disrupted in calbindin⁺ neurons (**Figure 12I**). Specifically we observed that cholinergic blockade let loss of the distinct peak at theta frequency in the power spectra of spike discharges of calbindin⁺ neurons (**Figure 14A,B**); The firing pattern of calbindin⁻ neurons was not affected, as typically they were non-rhythmic (**Figure 14C,D**). Cells also differed in their phase-locking to entorhinal field potential theta: calbindin⁺ cells were more strongly phase-locked (average Rayleigh vector length = 0.54 vs 0.22 in calbindin⁻ cells; p < 0.0012, Mann-Whitney test) and fired near the trough of the theta oscillation, whereas locking was weaker and more variable in calbindin⁻ cells (**Figure 12J**).

5.2 Establishment of Juxtacellular Recordings in Freely Moving Rats

Results in this chapter have been published (Tang et al., 2014a).

Before attempting the experiment, we suggest greenhand experimenters to practice the juxtacellular recording/labeling procedure first in anesthetized, then in awake head-fixed animals, until a stable recording condition and a reliable cell recovery rate (> 80%) are achieved. Unequivocal assignment of the recorded neuron(s) is crucial to the method; to ensure the specificity of cell labeling, control experiments s be considered, as originally described by Pinault (Deschênes et al., 1994; Pinault, 1994, 1996). For example, experiments where neurons are (i) recorded in juxtacellular configuration but not stimulated with positive current, (ii) stimulated with negative current or (iii) stimulated with sub-threshold positive current (i.e. insufficient to modulate cell firing), should result in no cell labeling. Killing the recorded neuron by high current injection at the end of the labeling protocol can be used as a proof-of-principle test for the specificity of the juxtacellular labeling procedure (see Deschênes et al., 1994; Pinault, 1994, 1996).

By making it possible to monitor the spiking activity of single, morphologically-identified neurons while animals are freely behaving, this approach has provided instrumental in elucidating structure-function relationships in the spatial memory circuits (Brecht et al., 2014; Ray et al., 2014; Tang et al., 2014a). As additional examples, here we show anatomical identification of some spatial/directional modulated neurons: a grid cell (Hafting et al., 2005; **Figure 15**) and a head-direction cell (Taube et al., 1990; Taube, 2007; **Figure 16**), which are thought to constitute an internal representation of external space (Moser et al., 2008; Moser and Moser, 2013). The grid cell was recorded in layer 3 of medial entorhinal cortex (Hafting et al., 2005), in which its cellular architechture and spatial tuning has been
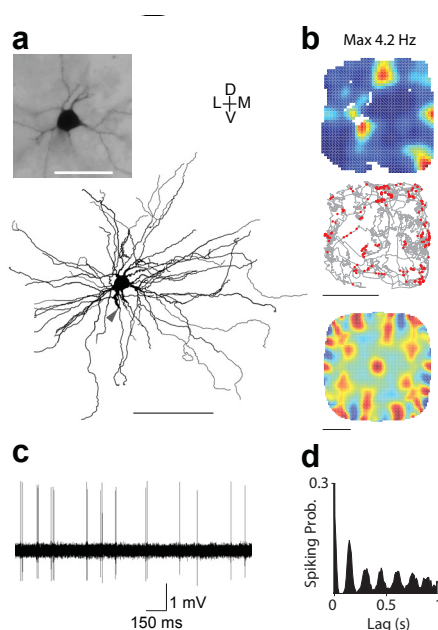
Figure 15: Morphological identification of a grid cell. (A) Top: micrograph of a diaminobenzidine-stained 60-μm-thick tangential section, showing the soma of a layer 3 neuron of MEC recorded in a freely moving rat. Scale bar, 50 μm. Bottom: tangential projection (top view) of the reconstruction of the basal dendritic field. Gray arrowhead shows the truncated apical dendrite (not shown in this reconstruction). Scale bar, 100 μm. D, dorsal; V, ventral; M, medial; L, lateral. (B) Top: color-coded rate map (red indicates maximal firing rate, indicated above) showing the spatial activity profile of the recorded neuron (shown in a). Middle: spike-trajectory plot showing the animal's trajectory (gray line) and the position at which spikes occurred (red dots). Bottom: 2D spatial autocorrelation of the rate map shown in b (top), revealing the hexagonal grid cell periodicity. Scale bar, 50 cm. (C) Representative juxtacellular spike-trace recorded during freely moving behavior for the neuron shown in a. (D) Spike autocorrelogram for the neuron shown in A. Adapted from Tang et al., 2014a.

reported (Canto and Witter, 2012; Burgalossi and Brecht, 2014). The recorded neuron was identified and classified as a large pyramidal neuron (**Figure 15A**), located in the upper layer 3 (L2/3 border). **Figure 15A** shows a reconstruction of the basal dendrites of the recorded neuron, where a large spread of the basal dendritic field within L3, extending for up to 322 μm and 371 μm along the dorsoventral and medio-lateral axis could be observed respectively. This neuron fired at multiple locations during exploration, showing a hexagonal symmetry (grid score = 0.53; **Figure 15B**), a defining feature of grid cell activity (Hafting et al., 2005), and was strongly modulated at theta frequency (4-12 Hz; **Figure 15C,D**). To our knowledge, this technique has provided first evidence of juxtacellularly recorded, anatomically identified and reconstructed grid cells in 2D open field.

Sharply tuned head-direction cells were recorded in the parasubiculum (Boccara et al., 2010; Burgalossi et al., 2011). **Figure 16A** showed a fluorescent micrograph containing the soma of the recorded neuron and a few proximal dendrites (**Figure 16A**). This cell did not show any clear spatial

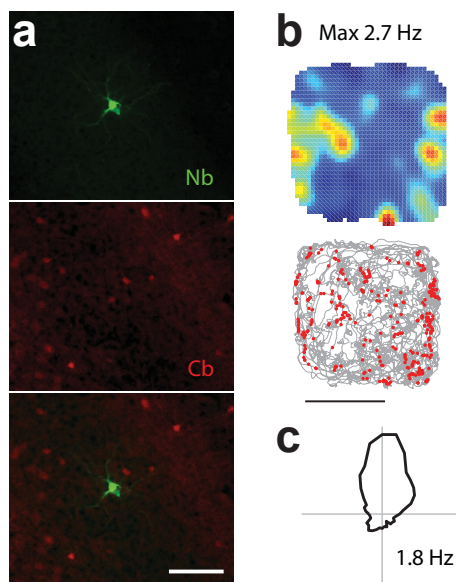**Figure 16: Morphological identification of a head-direction cell. (A) Fluorescence micrograph of a 60-μm-thick tangential section stained for Neurobiotin (Nb, green) and calbindin (Cb, red), showing the soma and proximal dendrites of a parasubicular neuron recorded in a freely moving rat. Scale bar, 100 μm. (B) Top, color-coded rate map (red indicates maximal firing rate, indicated above) showing the spatial activity profile of the recorded neuron (shown in A). Bottom: spike-trajectory plot showing the animal's trajectory (gray line) and the position at which spikes occurred (red dots). Scale bar, 50 cm. (C) Firing activity as a function of head direction for the cell shown in a. Peak firing rate is indicated. Adapted from Tang et al., 2014a.**

firing pattern (**Figure 16B**), but its spiking activity was sharply tuned to the animal's heading direction (**Figure 16C**), consistent with the previous extracellular recordings (Sargolini et al., 2006; Taube et al., 1990).

In these two cell examples, juxtacellular recordings were maintained for 16 min (**Figure 15**) and 14 min (**Figure 16**) before the labeling protocol was initiated. Within these times, the animals sampled 63 % (**Figure 15B**) and 77 % (**Figure 16B**) of the available surface of a large 1 x 1 m open field arena, which provided sufficient spatial coverage for assessing the functional properties of the recorded neurons.

In summary, the methodology described here represents a step forward towards filling the long-

standing gap between extracellular recordings and single-cell identification methods. It provides the means for exploring the functional implications of single cell heterogeneity, and is an addition to the portfolio of currently available methods aimed at resolving the cellular and circuit basis of animal behavior.

5.3   Pyramidal and Stellate Cell-specificity of Grid and Border Representations in Layer 2 of Medial Entorhinal Cortex

Results in this chapter have been published (Tang et al., 2014b).

5.3.1 Grid-like Firing Properties in a Calbindin⁺ Pyramidal Neuron and Border-responses in a Calbindin⁻ Stellate Neuron

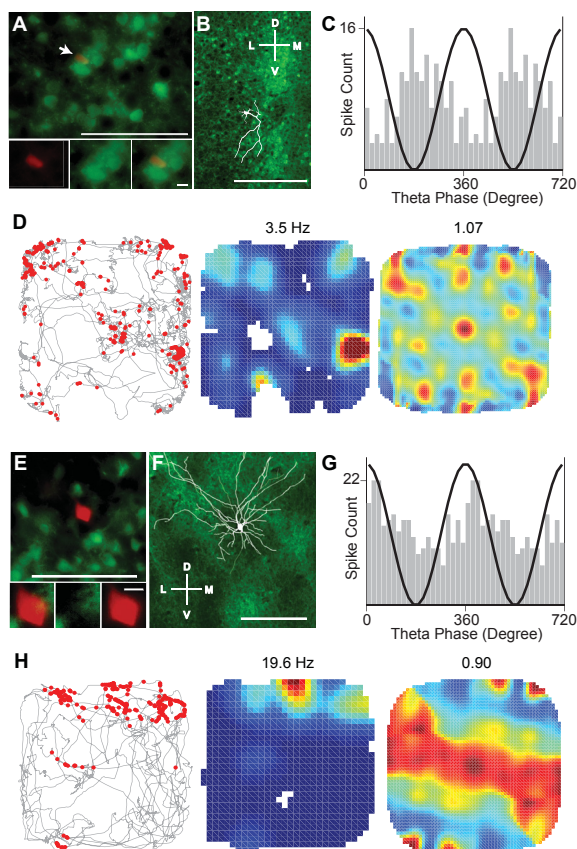Similar to previously described (Ray et al., 2014; Tang et al., 2014a), we juxtacellularly recorded

Figure 17: Grid firing in calbindin⁺ pyramidal neuron and border firing in calbindin⁻ stellate neuron. (A) Top, micrograph (tangential section) of a calbindin⁺ neuron recorded in a rat exploring a 2D environment (1 x 1 m). Green, calbindin; red, Neurobiotin. Bottom panels, soma in red, green channel and overlay. Scale bars, 100 μm (top), 10 μm (bottom). **(B)** Micrograph of a tangential layer 2 section with calbindin immunoreactivity (green) and superimposed reconstruction of the pyramidal neuron (white). The cell was poorly stained, basal dendrites were minor and a prominent apical dendrite extended towards the center of a calbindin patch ventral from the neuron. Scale bar, 250 μm. **(C)** Theta-phase histogram of spikes for the neuron shown in (A). For convenience, two repeated cycles are shown. The black sinusoid is a schematic local field potential theta wave for reference. **(D)** Spike-trajectory plot, rate map and two-dimensional spatial autocorrelation of the rate-map revealing the hexagonal grid cell periodicity. Spike-trajectory plot: red dots indicate spike locations, grey lines indicate the rat trajectory. Rate map: red indicates maximal firing rate, value noted above. Spatial autocorrelation: color scale -1 (blue) through 0 (green) to 1 (red). For this cell, the grid score is 1.07. **(E)** Left, micrograph (tangential section) of a calbindin⁻ neuron recorded in a rat exploring a 2D environment (70 x 70 cm). Green, calbindin; red, Neurobiotin. Right panels, soma in red, green channel and overlay. Scale bars, 100 μm (left), 10 μm (right). **(F)** Micrograph of the tangential layer 2 section with calbindin immunoreactivity (green) and superimposed reconstruction of the stellate neuron (white). The cell was well stained and the huge dendritic field encompassed several calbindin patches. Scale bar, 250 μm. **(G)** Theta-phase histogram of spikes for the neuron shown in (A). For convenience, two repeated cycles are shown. The black sinusoid is a schematic local field potential theta wave for reference. **(H)** Spike-trajectory plot, rate map and two-dimensional spatial autocorrelation of the rate-map revealing the elongated firing field. Spike-trajectory plot: red dots indicate spike locations, grey lines indicate the rat trajectory. Rate map: red indicates maximal firing rate, value noted above. Spatial autocorrelation: color scale -0.5 (blue) through 0 (green) to 0.5 (red). For this cell, the border score is 0.90. D = dorsal, L = lateral, M = medial, V = ventral. Adapted from Tang et al., 2014b.

and labeled neurons in layer 2 (which contains the largest percentage of pure grid cells; Boccara et al., 2010) in awake rats trained to explore 2D environments. Clear grid cell discharges were rare. The clearest grid-like firing pattern in our sample of 31 identified cells (17 of which met the criteria for spatial analysis; see Methods) was observed in the calbindin[+] cell shown in **Figure 17A**. This neuron had a typical pyramidal cell morphology, with simple dendritic arborization and a single large apical dendrite targeting a calbindin[+] patch (**Figure 17B**; see also Ray et al., 2014). During exploratory behavior, calbindin^{+} neurons fired in strong theta-rhythmicity and phase-locked near the trough of the local field potential theta-rhythm (**Figure 17C**; Ray et al., 2014). Spatial autocorrelation analysis of the firing pattern in the 2D environment revealed a hexagonal periodicity of firing fields (grid score = 1.07; **Figure 17D**), indicative of grid cell activity (Hafting et al., 2005). Because of its relatively low firing rate (~0.5 Hz) this cell was not included in the grid cell sample (see Methods). Many other identified calbindin^{+} neurons had no clear spatial firing patterns.

The calbindin[-] cell shown in **Figure 17E** showed the clearest border response in the identified dataset. This cell was a stellate neuron, which did not have a single apical dendrite, but instead extended multiple and widely diverging ascending dendrites; this dendritic tree spanned a vast field, which encompassed multiple calbindin[+] patches (**Figure 17F**; see also Ray et al., 2014). On average, spikes from calbindin^{-} neurons were weakly modulated by the local theta-rhythm without any obvious phase locking to the theta rhythm (**Figure 17G**). In 3 out of 11 calbindin^{-} cells from recordings with sufficient spatial coverage, we observed clear border firing patterns as in **Figure 17H**. Non-spatial firing patterns also dominated in calbindin^{-} neurons, but surprisingly no grid firing pattern was observed.

While the small dataset of identified neurons prevented us from establishing firm structure-function relationships, four preliminary observations can be drawn: (i) grid cells are less abundant in layer 2 than previously assumed (Sargolini et al., 2006; Boccara et al., 2010; but see Mizuseki et al., 2009; Gupta et al., 2012; Bjerknes et al., 2014) and there is no one-to-one relationship between spatial discharge characteristics and cell type; (ii) calbindin^{+} neurons might include grid cells; (iii) the absence of grid cells in the 22 identified calbindin^{-} stellate neurons suggests that grid cells might be rare in this cell population; (iv) calbindin^{-} neurons include border cells.

5.3.2 Anatomical Characterization of Calbindin[+] Pyramidal and Calbindin[-] Stellate Cells in Layer 2 of Medial Entorhinal Cortex

It has been suggested to have a strong correspondence between cytochemical (calbindin[+] vs calbindin[-]) and morphological (pyramidal vs stellate) classification of principal neurons in layer 2 (Varga et al., 2010; Kitamura et al., 2014; Ray et al., 2014). To further explore these relationships,
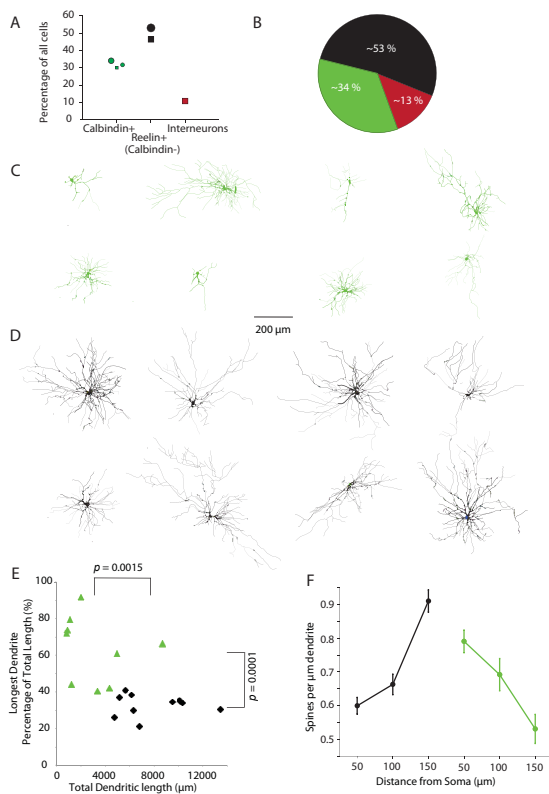
Figure 18: Anatomical characterization of calbindin⁺ pyramidal and calbindin⁻ stellate cells in layer 2. (A) Percentage of all neurons classified as calbindin⁺, reelin⁺ (calbindin⁻) and interneurons in layer 2 of MEC of a rat. Absolute reelin⁺ numbers have been extrapolated from calbindin⁺ and reelin⁺ counts. Circular markers indicate measurement made in this study. Square markers indicate measurements made by other studies (Peterson et al., 1996; Kumar and Buckmaster, 2006; Varga et al., 2010). **(B)** Distribution of calbindin⁺ neurons (green), reelin⁺ neurons (black) and interneurons (red) in layer 2 of MEC of a rat. Numbers indicate averages of measurements indicated in panel A. **(C)** Identified calbindin⁺ cells have pyramidal morphologies. All cells come from tangential sections and are hence shown in 'views from the top'. **(D)** Identified calbindin⁻ cells have stellate morphologies. All cells come from tangential sections and are hence shown in 'views from the top'. **(E)** Identified and reconstructed calbindin⁺ cells and calbindin⁻ cells show significant (t-test) size and shape differences. **(F)** Spine distribution differs in calbindin⁺ cells and calbindin⁻ cells; data refer to ten cells each, for which we counted spine densities in multiple ~30 μm dendrite segments at the distances from the soma specified in the plot. Slopes of spine density differed significantly between calbindin⁺ cells and calbindin⁻ cells (p = 0.0023, t-test). Adapted from Tang et al., 2014b.

we determined the percentage of calbindin⁺ cells in layer 2 and compared these data with related measurements in the literature (**Figure 18A**). In line with previous studies (Peterson et al., 1996; Kumar and Buckmaster, 2006; Varga et al., 2010), we found that layer 2 neurons consist of about one third calbindin⁺ and ~50 % calbindin⁻ (and reelin⁺) principal cells, and ~13 % interneurons (**Figure 18B**). We note that while Ray et al., 2014 found about 30% of calbindin⁺ cells most of which were shown to have pyramidal morphology (see also Varga et al., 2010; Kitamura et al., 2014), Gatome et al., 2010 found a slightly lower fraction of putative pyramidal cells. Calbindin⁺ and calbindin⁻ cells showed large quantitative differences in their morphology but without a clear bimodality in individual morphological parameters (**Figure 18C,D**). Calbindin⁺ cells had significant (on average ~2.5 fold) smaller dendritic trees (**Figure 18E**). Dendritic trees also differed in shape between cell types. Calbindin⁺ cells had a single long (always apical) dendrite, which accounted on average for 63% of the total dendritic length (**Figure 18E**) and which was polarized towards the center of pyramidal cell patches as shown previously (Ray et al., 2014). Calbindin expression matched well but not perfectly with pyramidal cell morphology (**Figure 18C,D**). Calbindin⁻ cells featured similar length dendrites with the longest dendrite contributing on average for 33% of the total dendritic length (**Figure 18E**). These results are in line with published data and indicate that calbindin⁺ and calbindin⁻ cells largely correspond to pyramidal and stellate neurons, respectively. However, the lack of clear morphological

bimodality in layer 2 (see also Canto and Witter, 2012) implies that the correspondence of pyramidal/ calbindin[+] and stellate/calbindin[-] might not be perfect. Interestingly, the spine density in calbindin^{+} cells decreased as a function of distance from the soma, whereas the reverse was the case calbindin^{-} cells (**Figure 18F**). These morphological differences, together with clustering of calbindin^{+} cells in patches and the polarization of their apical dendrites towards the center of calbindin[+] patches (Ray et al., 2014) probably suggest a local and overlapping sampling of inputs in neighboring calbindin^{+} cells, whereas neighboring calbindin^{-} stellate cells sample large and non-overlapping input territories.
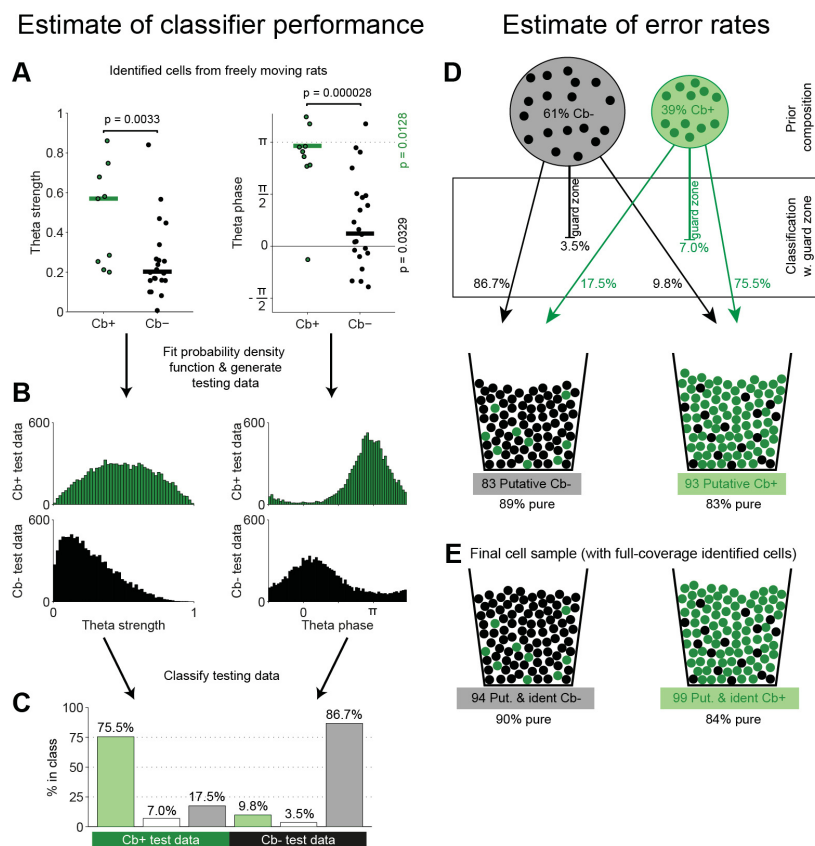
Figure 19: Testing of the classifier and error estimates. (A) Theta strength and preferred theta phase of identified calbindin^{+} cells (green dots) and calbindin^{-} cells (black dots) is significantly different. Green and black lines indicate medians of theta strength (p = 0.0033, Mann-Whitney U-test). Green and black lines indicate circular means of preferred theta phase (p = 0.000028, Parametric Watson-Williams multi-sample test). Calbindin^{+} cells show a significant tendency to fire near the trough (p = 0.013, Rayleigh's test for nonuniformity) and calbindin^{-} cells show a tendency to fire near the peak of theta rhythm (p = 0.033, Rayleigh's test for nonuniformity). **(B)** Distribution of testing data for estimation of classifier performance. Testing data is generated by fitting the appropriate probability density functions (beta distributions and circular Gaussian distributions, respectively) to the distributions of theta strength and preferred theta phase of identified calbindin[+] and calbindin^{-} cells (N = 10.000 for both cell types). **(C)** Result of classification of testing data shows that both calbindin^{+} cells and calbindin^{-} cells are classified with high accuracy and low false classification rates (75.5% correct and 17.5% incorrect for calbindin^{+} cells, 86.7% correct and 9.8% incorrect for calbindin^{-} cells). This shows that the classification boundary is robust and not just overfitting the small training set of identified cells. **(D)** Estimation of the purity (positive predictive value) of the classifier based on the estimate of 34% calbindin[+], 53% reelin[+] (calbindin[-]) and 13% interneurons in rat L2 of MEC (Figure 18A,B). The sample of 93 putative calbindin^{+} cells is estimated to be 83% pure, and the sample of 83 putative calbindin^{-} cells is estimated to be 89% pure. **(E)** After addition of identified, full-coverage cells (11 calbindin[-] and 6 calbindin[+]), we estimate the purity of our final cell sample to be 84% for calbindin[+] cell and 90% for calbindin^{-} cells. Adapted from Tang et al., 2014b.

5.3.3 Testing of the Classifier and Error Estimates

Calbindin$^+$ pyramidal and calbindin$^-$ stellate cells have diverse temporal discharge properties (**Figure 17C,G**; Ray et al., 2014). Therefore, temporal spike discharge properties could be useful parameters to classify layer 2 principal cells as putative pyramidal or stellate neurons. We designed a support vector machine to classify neurons based on both the preferred theta phase and phase locking strength to local field potential theta oscillations, which indeed clearly segregated calbindin$^+$ and calbindin$^-$ cells with a large distance to the separating hyperplane (see Methods). To further improve the purity and certainty of assigned cells, we added a more strict guard zone around the hyperplane separating the Gaussian kernels classifying calbindin$^+$ (light green background) and calbindin$^-$ (grey background) cells (omitting the guard zone and classifying all cells did not qualitatively affect the results; data not shown). We tested our classifier by a bootstrapping approach (**Figure 19A,B**) and found that a large fraction of calbindin$^+$ and calbindin$^-$ cells could be correctly assigned (**Figure 19C**). More importantly, the specificity of classification procedure, which is reflected in the purity of the resulting cell samples, was excellent, where ~89% putative calbindin$^-$ cells and ~83% putative calbindin$^+$ cells could be assigned (**Figure 19D**), and even higher values for combination of identified and putatively assigned cells (**Figure 19E**). We further evaluated the robustness of the classifier by testing in identified layer 2 neurons (Ray et al., 2014) under urethane/ketamine anesthesia (Klausberger et al., 2003). Even though theta-phase and strength of locking might differ between the awake and anesthetized state, similarly to the awake situation however, the large majority of neurons recorded under anesthesia were also correctly classified (92% of calbindin$^+$, 65% of calbindin$^-$ cells, $p < 0.001$, bootstrap; **Figure 20B** bottom), suggesting that our classification criteria work robustly and can effectively generalize across very different recording conditions (**Figure 20B**). Encouraged by these results, we classified the larger dataset of our hitherto unidentified layer 2 juxtacellular and tetrode recordings (classified + identified n = 193 cells).

5.3.4 Cell Classification and Grid and Border Responses in Pooled Identified and Theta-assigned Cells

To assess the relationship between cell identity and spatial firing properties, we pooled the non-identified recordings assigned to putative calbindin$^+$ and calbindin$^-$ cells, with identified neurons. The pooled datasets included n = 99 calbindin$^+$ and n = 94 calbindin$^-$ cells, respectively. We assessed spatial discharge patterns based on quantitiative scores (grid score > 0.3; border score > 0.5, Solstad et al., 2008) to the cells which carried significant amount of spatial information (Skaggs et al., 1993; Bjerknes et al., 2014; see also Methods).
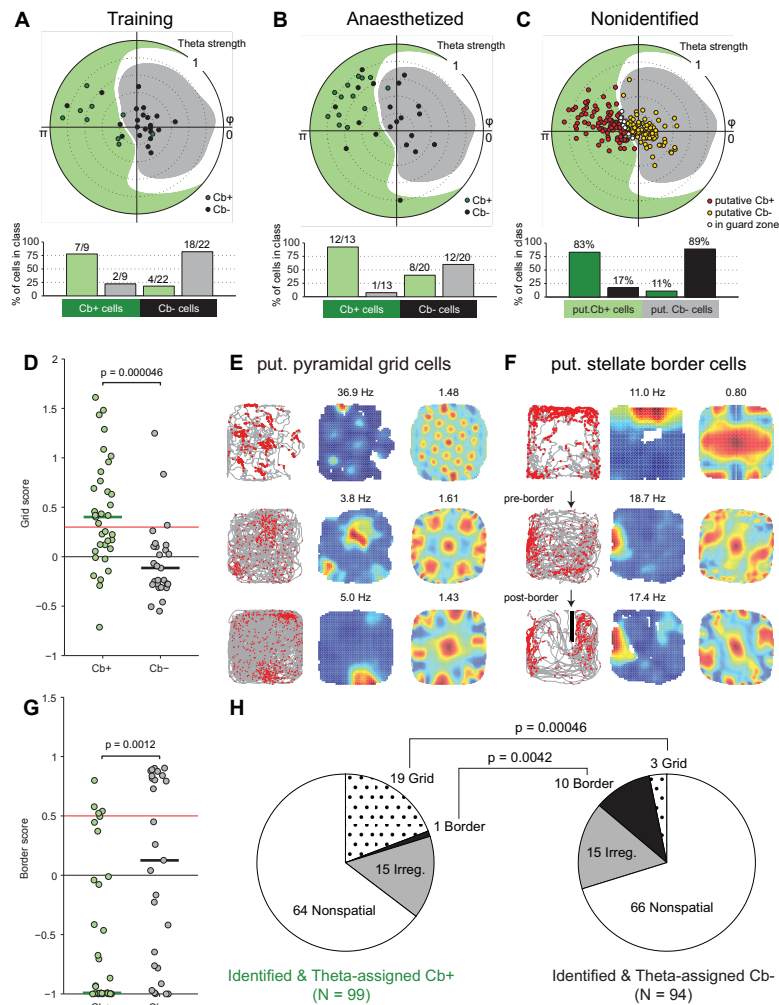
Figure 20: Cell classification and grid/border responses in pooled identified and theta-assigned cells. (A) Top, classification training set: Polar plot of theta strength (value indicated by the upper right number) and preferred theta phase angle, φ, for calbindin+ cells (green dots) and calbindin- cells (black dots) identified in freely moving rats. Background color fill shows classification boundary based on φ and theta strength: Cells in the pale green area and grey area will be classified as calbindin+ and calbindin- cells respectively. Bottom, fraction of cells in classification categories. **(B) Top,** polar plot of theta strength and of preferred theta phase angle, φ, for calbindin+ cells (green dots) and calbindin- cells (black dots) identified in anaesthetized rats, overlaid on classification boundary. Bottom, fraction of cells in classification categories. **(C) Top,** polar plot of theta strength and preferred theta phase angle, φ, for non-identified cells. Putative calbindin+ cells (red dots) and putative calbindin- cells (yellow dots) are shown overlaid on the classification boundary, together with unclassified cells (white dots). Bottom, estimate of the purity of the theta-assigned cell categories. The sample of putative calbindin- cells are estimated to be 89% pure, and the sample of putative calbindin+ cells are estimated to be 83% pure (see Figure 19). **(D)** Comparison of grid scores between (identified and putative) calbindin+ and calbindin- neurons; the dotted line indicates the threshold for grid cell; vertical lines indicate medians (p = 0.000046, Mann-Whitney U-test). **(E)** Representative grid firing pattern observed in calbindin+ neurons (spike-trajectory plot, rate-map and spatial autocorrelation. Maximum firing rate and grid score indicated above plots.). **(F)** Border firing patterns in calbindin- neurons. Conventions as in **(E)**. Arrows indicate insertion of additional border. **(G)** Comparison of border scores between (identified and putative) calbindin+ and calbindin- neurons; the dotted line indicates the threshold for border cells; vertical lines indicate medians (p = 0.0012; Mann-Whitney U-test). **(H)** Distribution of spatial discharge types in calbindin+ (left) and calbindin- (right) neurons, was found to be significantly different in numbers of grid cells and border cells (p = 0.00046 and 0.0042, Pearson's Chi-squared test). Adapted from Tang et al., 2014b.

This approach identified convincing grid and border responses in line with visual inspection. Consistent with previous studies (Hafting et al., 2005; Sargolini et al., 2006; Boccara et al., 2010;

Burgalossi et al., 2011; Domnisoru et al., 2013), a large fraction of layer 2 neurons (33%; n = 63 cells) were significantly spatially-modulated. Weak hexagonal symmetry of spatial firing patterns was observed in both the calbindin⁺ and calbindin⁻ cells, in agreement with previous observations (Burgalossi et al., 2011; Domnisoru et al., 2013; Schmidt-Hieber and Häusser, 2013). However, grid scores in the calbindin⁺ population were significantly higher than those in the calbindin⁻ population (p = 0.000046, Mann-Whitney test; **Figure 20D,E**), consistent with observations from the identified dataset (**Figure 17**). On the other hand, confirming our observations from the identified dataset (**Figure 17**), calbindin⁻ cells had significantly higher border scores than calbindin⁺ cells (**Figure 20G**; p = 0.0012, Mann-Whitney test). Representative border discharges in calbindin⁻ cells are shown in **Figure 20F**, including an example with border test (Solstad et al., 2008; Lever et al., 2009).

      Figure 20H overviewed the spatial response properties of our pooled calbindin⁺ and calbindin⁻ datasets, respectively. Many of the calbindin⁺ and calbindin⁻ neurons were not spatial modulated. Grid firing patterns were significantly more common in the calbindin⁺ population, where 19% (19/99) of the cells passed grid cell criteria, compared to only 3% (3/94) in the calbindin⁻ population (p = 0.00046, Fisher's exact test). A significant higher fraction of calbindin⁻ cells passed the border cell criterion (10% calbindin⁻, 10/94 cells; vs 1% calbindin⁺, 1/99 cells) than the calbindin⁺ cells (p = 0.0042, Fisher's exact test). These large data samples confirm and extend the conclusion from our
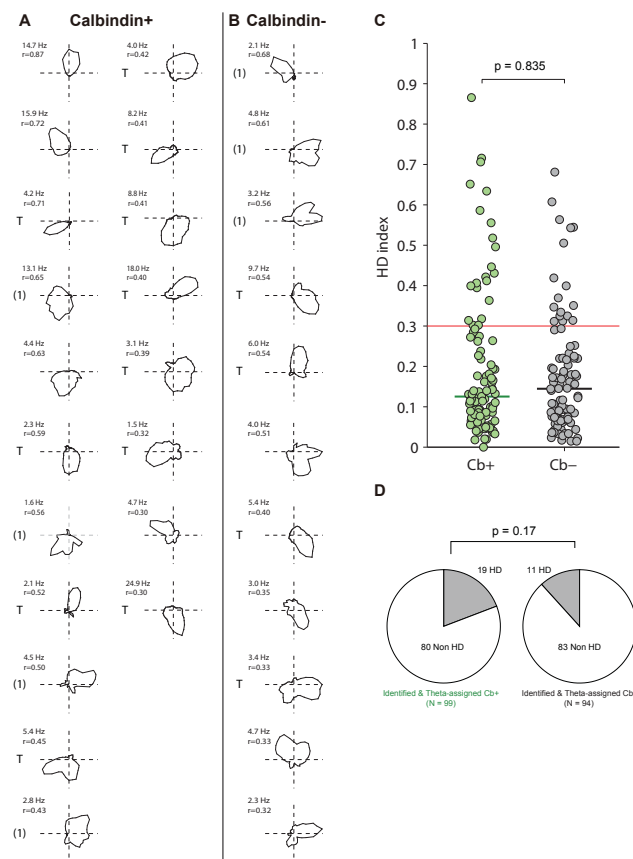
Figure 21: Head-direction tuning of identified and theta-assigned calbindin⁺ and calbindin⁻ neurons. (A) Polar plots of the head-direction tuning in identified and theta-assigned calbindin⁺ neurons, which carry significant directional information. Cells are ranked according to Rayleigh vector lengths. (B) Polar plots of the head-direction tuning in identified and theta-assigned calbindin⁻ neurons, which carry significant directional information. Cells are ranked according to Rayleigh vector lengths. (C) Comparison of HD index (Rayleigh vector length) between (identified and putative) calbindin⁺ and calbindin⁻ neurons; the dotted line indicates the threshold for head-direction cell; vertical lines indicate medians (p = 0.835, Mann-Whitney U-test). (D) Numbers of head-direction cells in (identified and putative) calbindin⁺ (A) and calbindin⁻ (B) neurons were not different (p = 0.17, Fisher's exact test). Adapted from Tang et al., 2014b.

recordings of identified cells and indicate that grid cells are preferentially recruited from the calbindin[+] population, while border responses preferentially occur in calbindin^{-} cells.

Unlike previous reports based on tetrode recordings (Sargolini et al., 2006; Boccara et al., 2010; but see Zhang et al., 2013) a substantial fraction of cells showed head-direction selectivity both in identified and theta-assigned calbindin[+] and calbindin^{-} cells (**Figure 21**). Head-direction selectivity was present in both calbindin[+] (19%, 19 out of 99 cells) and calbindin^{-} cells (12%, 11 out 94 cells), without preference (p = 0.17, Fisher's exact test); both classes contained pure as well as conjunctive responses (Sargolini et al., 2006).

5.3.5 Temporal Spiking Properties of Grid Cells and Border Cells
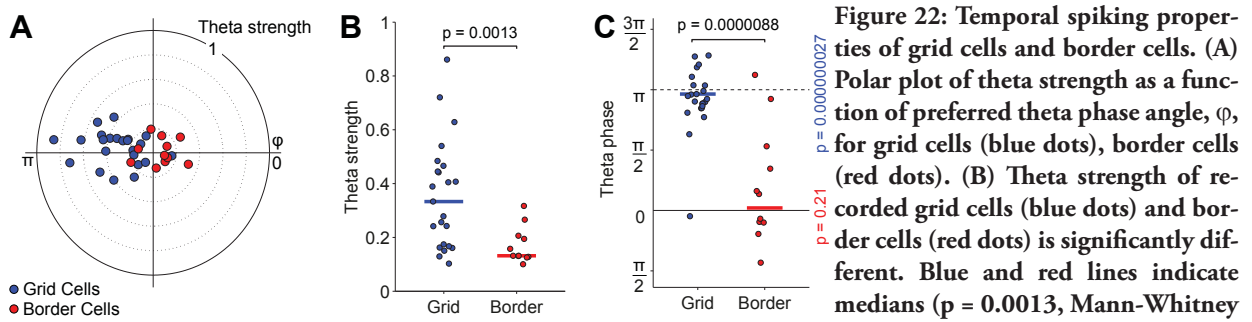
Figure 22: Temporal spiking properties of grid cells and border cells. (A) Polar plot of theta strength as a function of preferred theta phase angle, φ, for grid cells (blue dots), border cells (red dots). (B) Theta strength of recorded grid cells (blue dots) and border cells (red dots) is significantly different. Blue and red lines indicate medians (p = 0.0013, Mann-Whitney U-test). (C) Preferred theta phase for grid cells (blue dots) and border cells (red dots). Blue and red lines indicate circular means (p = 0.0000088, Parametric Watson-Williams multi-sample test). Grid cells show a significant tendency to fire near the trough (p = 0.000000027, Rayleigh's test for nonuniformity). Border cells show a tendency to fire near the peak of theta rhythm, but the phase-locking to theta peak did not reach significance in our data set (p = 0.21, Rayleigh's test for nonuniformity). Adapted from Tang et al., 2014b.

The grid and border cells showed systematic differences in spike phase locking to theta oscillations (**Figure 22A**). Spikes from most grid cells were strongly entrained by the theta-rhythm, with strong phase-locking (**Figure 22B**) and a phase-preference near the theta-trough (**Figure 22C**; p = 0.000000027, Rayleigh's test for nonuniformity). The modulation of spiking activity of border cells by the theta-rhythm was significantly weaker than in grid cells (**Figure 22B**; p = 0.0013, Mann-Whitney test) and showed on average only a weak phase-preference for the theta-peak (**Figure 22C**; p = 0.21, Rayleigh's test for nonuniformity), which differed significantly from the phase-preference of grid cells (**Figure 22B,C**; p = 0.0000088, Parametric Watson-Williams multi-sample test). Thus, in layer 2 grid and border signals mirrored the temporal differences between calbindin[+] pyramidal and calbindin^{-} stellate cells reported earlier (Ray et al., 2014).

5.4   Functional Architecture of the Parasubiculum

5.4.1 Geometry of the Parasubiculum

In our initial analysis we sought to determine the general organization of the parasubiculum. Tangential sections of the cortical sheet stained for acetylcholine esterase activity (**Figure 23A**) or calbindin immunoreactivity (**Figure 23B**) provide a particularly clear overview of the spatial extent of the parasubiculum. Consistent with findings from previous studies (Geneser, 1986; Slomianka and Geneser, 1991), we find that the parasubiculum shows prominent acetylcholine esterase activity (**Figure 23A**). The parasubiculum can also be identified by an absence of calbindin immunoreactivity as it contains barely any calbindin-positive neurons (**Figure 23B**; Fujise et al., 1995; Boccara et al., 2010). In **Figure 23C**, we show the parasubiculum schematically along with divisions of medial entorhinal cortex (see Ray et al., 2014). Here we also clarify that all our data refer to the 'outer / distal to medial entorhinal cortex' subdivision of the parasubiculum, i.e. the 'parasubiculum b' in the terminology of (Blackstad, 1956). The 'inner' parasubicular subdivision, the 'parasubiculum a' in the
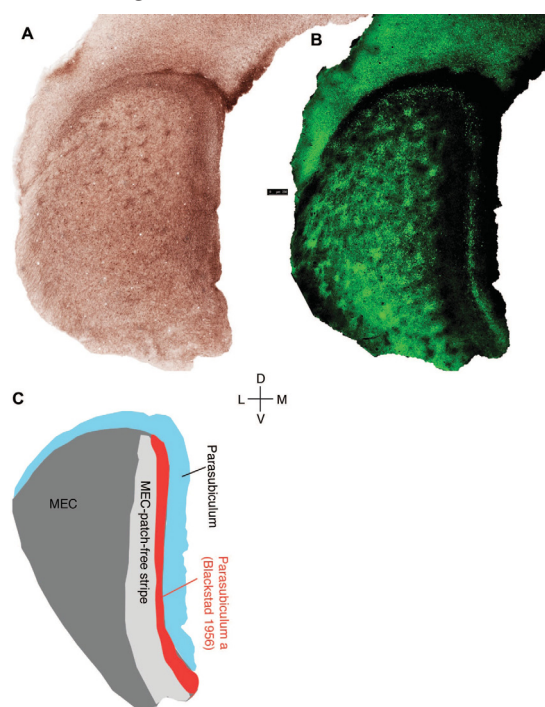
Figure 23: Shape of the rat parasubiculum in a section tangential to the cortical plane. (A) Tangential section stained for acetylcholinesterase activity (dark precipitate). The shape of the parasubiculum is outlined by high acetylcholinesterase activity. (B) Tangential section (adjacent to the one shown in A) processed for calbindin immunoreactivity (green), the shape of the parasubiculum is negatively outlined by an absence of calbindin immunoreactivity. (C) Schematic of the parasubiculum and adjacent medial entorhinal cortex subdivisions. We also show another parasubicular subdivision identified by (Blackstad, 1956), referred to as parasubiculum a. All our data refer to light blue region, the parasubiculum b in the terminology of (Blackstad, 1956). (A) and (B) were modified from (Ray et al., 2014).D = dorsal, L = lateral, M = medial, V = ventral.

terminology of (Blackstad, 1956) is not considered here; according to our observations, the latter has a cellular organization similar to medial entorhinal cortex and contains numerous calbindin-positive neurons (**Figure 23B**). As shown in **Figure 23A-C**, the parasubiculum forms a continuous stripe which flanks the medial entorhinal cortex from its medial to dorso-lateral side. The lateral part of the parasubiculum, dorsal to the medial entorhinal cortex, is narrower than the medial part. This may explain why this part of the parasubiculum has not been classified as such in most previous studies

(Boccara et al., 2010; Ding, 2013). Other histological markers such as cytochrome-oxidase activity or soma morphologies as visualized from Nissl stains (Burgalossi et al., 2011) also delineated the parasubiculum in the same way. Similarly, parasagittal sectioning angles delineate the same outlines of the parasubiculum. We conclude that the parasubiculum has a linear structure with its narrow width (matching that of a dendritic tree).

We also investigated the laminar structure of the parasubiculum. Consistent with our previous conclusions (Burgalossi et al., 2011), we found no evidence for a direct association of deep layers. Following tracer injections in the superficial parasubicular layers, we did not observe back-labeled cells in the adjacent deep layers, even when we observed back-labeled cells as distant as the subiculum (data not shown).

5.4.2 Internal Structure of the Parasubiculum
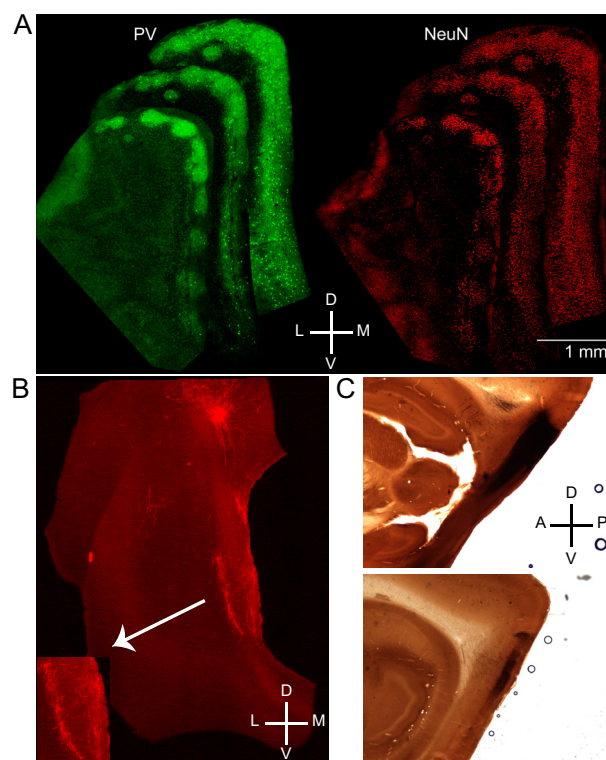
Figure 24: Internal structure of the parasubiculum.
(A) Tangential sections stained for parvalbumin (PV) immunoreactivity (green, left) and NeuN immunoreactivity (red, right). The parasubiculum stand out by its intense staining. Three sections are shown, the left one is most superficial (closest to the pia), middle and right are progressively deeper. Note how the patchy structure of the superficial parasubiculum is replaced by continuous cell band in deeper sections.
(B) Injection of tracer BDA (red fluorescence) reveals circumcurrent axons extending throughout the parasubiculum.
(C) Injection of larger amounts of tracer BDA completely fill the parasubiculum.
D = dorsal, L = lateral, M = medial, V = ventral, A = anterior, P = posterior.

Consistent with our previous observations (Burgalossi et al., 2011), we found the superficial parts of the parasubiculum (corresponding to layers 1 and 2) can be divided into 2 large patches with a diameter around 500 μm each. These patches can be revealed in superficial sections (**Figure 24A** left) by parvalbumin (PV)-immunoreactivity and by cell density visualized by NeuN immunoreactivity (**Figure 24A** right). However, the deeper parts of the parasubiculum (corresponding to layer 3) were not obviously divided into patches (right in **Figure 24A**).

Injections of the anterograde tracer Biotinyated Dextrane Amine (BDA, 3000 MW) showed that parasubicular neurons extend long axons throughout the full length of the parasubiculum (**Figure 24B**), consistent with previous observations from single-cell level (Burgalossi et al., 2011). As a consequence, a single tracer injection can label the full extent of the parasubiculum (**Figure 24C**). The fact that tracer injections at a single site could label the entire extent of the structure is a remarkable feature of the parasubiculum, which is not seen in the medial entorhinal cortex. Thus, analysis of the internal structure of parasubiculum indicates both modularity and global connectivity.

5.4.3 Inputs to the Parasubiculum
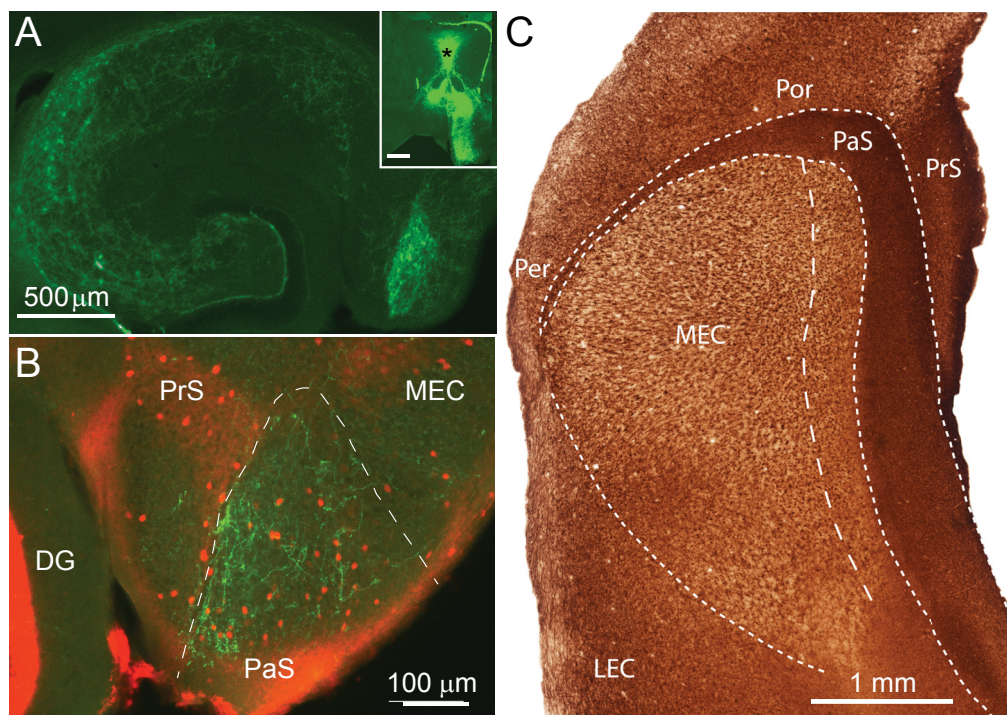
Figure 25: Parasubiculum receives GABAergic and cholinergic inputs. (A-B) Horizontal sections showing that the parasubiculum contains the densest projection in the hippocampal formation of GFP-positive, putative parvalbuminergic fibers (A) deriving from injection of AAV into the medial septum (inset, asterisk) of mice expressing Cre recombinase under the parvalbumin promoter. This dense projection pattern was seen in 3/3 injected mice. Note in this brain also olfactory and accessory olfactory areas were labelled unilaterally. Calretinin immunostaining delineates the border between presubiculum and parasubiculum (B). (C) Tangential section showing high levels of Acetylcholinesterase (AChE) in the parasubiculum.

Of particular interest for hippocampal function are the inputs from the medial septum, which are of critical importance to grid cell activity (Brandon et al., 2011; Koenig et al., 2011). We first sought to determine the patterns of GABAergic inputs from the medial septum, which are thought to play a critical role in theta-rhythm generation (Mitchell et al., 1982; Buzsáki, 2002; Hangya et al., 2009; Brandon et al., 2011; Koenig et al., 2011). To this end we performed viral injections in the medial septum in PV-Cre mice (see Methods), and expressed GFP selectively in GABAergic cells (**Figure 25**). As shown in **Figure 25A,B**, within the hippocampal formation the parasubiculum is the area receiving the densest innervation from GABAergic medial septal neurons. Thus, the parasubiculum appears to be the prime target of these fibers within the parahippocampal formation. As we already noted earlier, there is also a prominent expression of cholinergic activity markers (**Figure 23A** and **Figure 25C**). Taken together, these data point towards a strong medial septal drive to parasubicular neurons.

By retrograde-tracer injections, we also identified parasubicular-projecting neurons in the anterior thalamus, subiculum and presubiculum. The findings are consistent with the earlier conclusions of previous authors (Köhler, 1985; van Groen and Wyss, 1992; Honda and Ishizuka, 2004) and are therefore not shown.

5.4.4 Outputs from the Parasubiculum
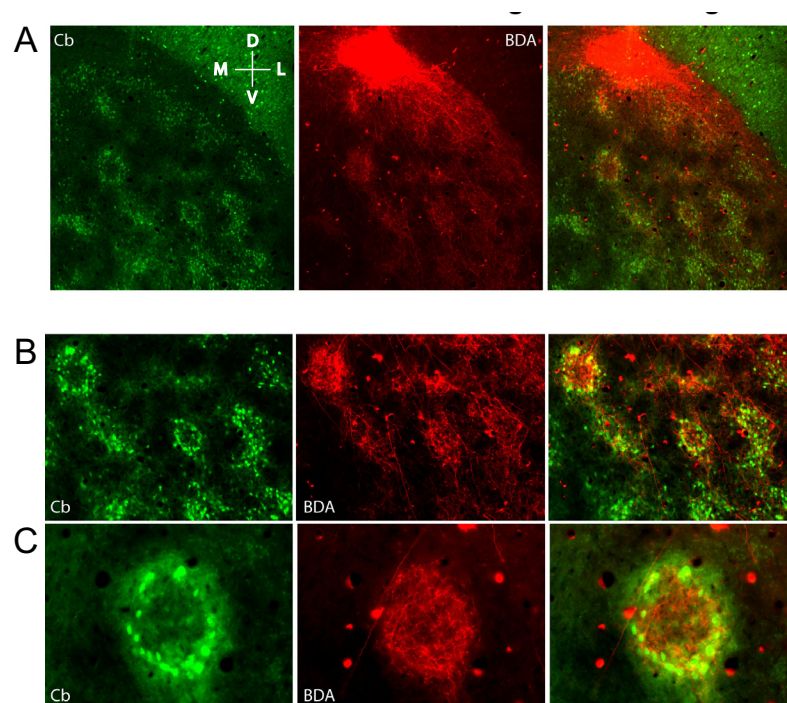
Figure 26: Parasubicular axons target layer 2 pyramidal cell patches in medial entorhinal cortex.
(A) Right, tangential section processed for calbindin immunoreactivity (green) revealing patches of calbindin-positive pyramidal cells. Middle, same section as left processed to reveal the tracer BDA (red). The location of the parasubicular injection site is marked with a white star. Right, overlay. (B) Same as (A) but higher magnification. (C) High magnification view of a single patch. D = dorsal, L = lateral, M = medial, V = ventral.

Previous work showed that the parasubicular axons innervate layer 2 of the medial entorhinal cortex (van Groen and Wyss, 1990; Caballero-Bleda and Witter, 1993, 1994; but see Canto et al., 2012). Recent work showed that principal cells in layer 2 of medial entorhinal cortex segregate into stellate and pyramidal cell subnetworks, which can be differentiated by the calbindin-immunoreactivity of the pyramidal neurons (Varga et al., 2010). Layer 2 pyramidal cells are arranged in a hexagonal grid, show strong theta-rhythmic discharges (Ray et al., 2014) and might preferentially contribute to the grid cell population (Tang et al. 2014b). To determine if parasubicular inputs target a specific subpopulation of neurons in layer 2 of medial entorhinal cortex, we performed fine scale injections of anterograde tracers in the dorsal parasubiculum, combined with visualization of calbindin patterns (**Figure 26**). As shown in **Figure 26**, tangential sections through layer 2 with calbindin immuno-staining revealed a regular organization of patches of pyramidal cells (Ray et al., 2014). Surprisingly, these patches were highly selectively innervated by parasubicular afferents (**Figure 26A,B**), which targeted the center of patches (**Figure 26C**). This indicates that parasubicular axons preferentially target layer 2 pyramidal neurons of medial entorhinal cortex.

5.4.5 Functional Cell Types in the Parasubiculum
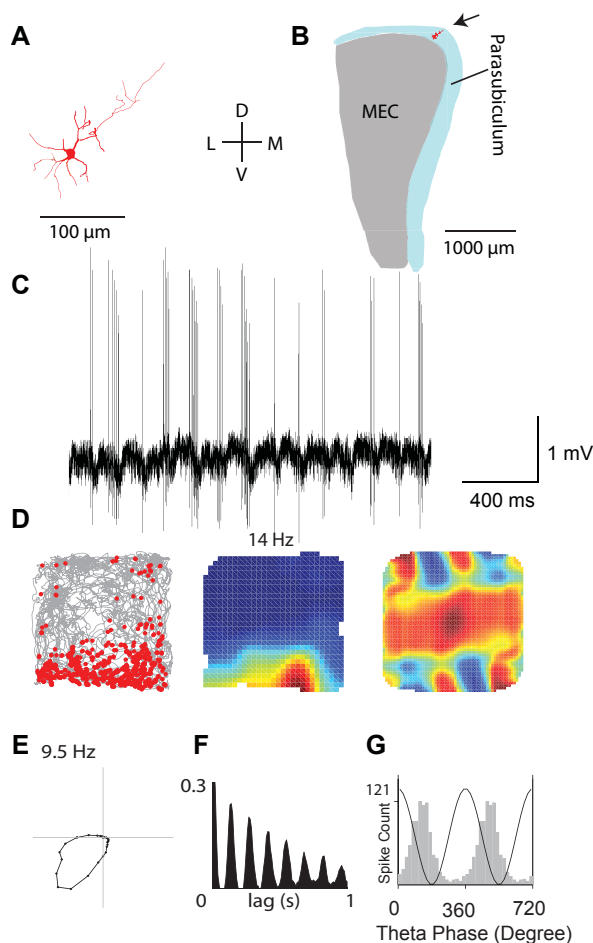
Figure 27: Border response in an identified parasubicular neuron.
(A) Reconstruction of a neuron recorded and identified in a rat exploring a 2D environment (70 x 70 cm). Scale bar, 100 μm.
(B) Schematic of the location the cell in the parasubiculum (arrow). The cell is located in the dorsal band of parasubiculum (blue), close to MEC (grey). Scale bar, 1000 μm.
(C) Representative raw traces of the recorded cell shown in (A). Note the prominent theta rhythms in LFP and theta modulated firing of the recorded cell.
(D) Spike-trajectory plot (left), rate map (middle) and two-dimensional spatial autocorrelation of the rate map (right) revealing the border firing. Spike-trajectory plot: red dots indicate spike locations; grey lines indicate the rat trajectory. Rate map: red indicates maximal firing rate, value noted above. Spatial autocorrelation: color scale -1 (blue) through 0 (green) to 1¬ (red). For this cell, the border score is 0.86.
(E) Polar plot of the cell's head-direction tuning. Value indicates maximum firing rate to the preferred direction.
(F) Autocorrelogram of spike discharges for the cell shown in (A).
(G) Theta-phase histogram of spikes for the cell shown in (A). For convenience, two repeated cycles are shown. The black sinusoid is a schematic local field potential theta wave for reference.
D = dorsal, L = lateral, M = medial, V = ventral.

In comparison to its major target structure - the entorhinal cortex - limited information is currently available about the spatial discharge properties in the parasubiculum (Taube, 1995; Cacucci et al., 2004; Boccara et al., 2010). To address this issue, we juxtacellularly recorded and labeled neurons (n = 16) or verified recording sites of single cell recordings (n = 7) in the parasubiculum of freely moving rats trained to explore 2D environments (Tang et al., 2014a). In about a third of all neurons with sufficient spatial coverage (6/19), we observed clear border responses, as shown in the neuron in **Figure 27**. This cell had divergent sideward-directed dendrites (seen from the top), situated in the dorsal part of the parasubiculum (**Figure 27B**) and discharged in spike bursts strongly entrained by the theta-rhythm (**Figure 27C**). The neuron discharged along the border of the enclosure (**Figure 27D**), a defining feature of border activity (Solstad et al., 2008). This neuron also showed strong head-direction selectivity (**Figure 27E**). Theta-rhythmicity of spiking was revealed by the spiking autocorrelogram (**Figure 27F**) and the spikes were also strongly locked to theta oscillations (**Figure 27G**). These data indicate that border discharge is a prime discharge pattern in the parasubiculum.
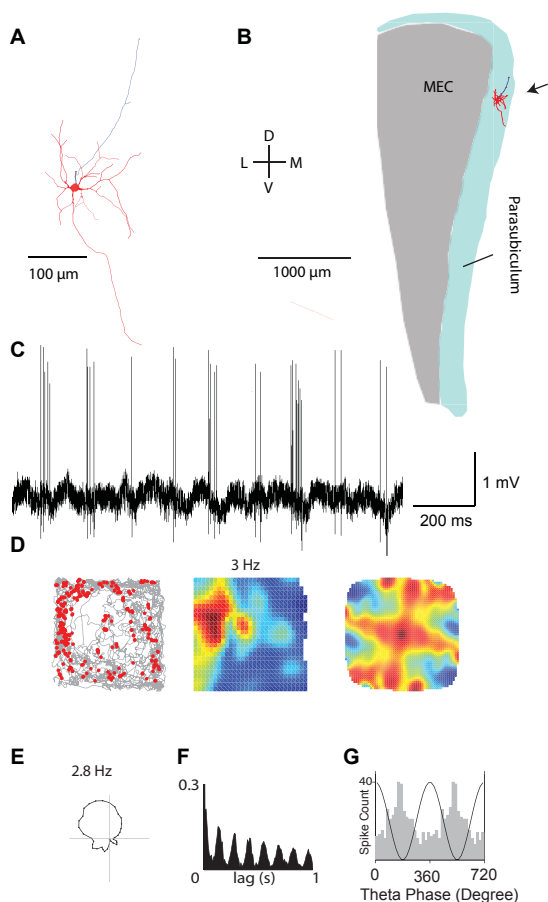
Figure 28: A head direction cell identified in the parasubiculum.

(A) Reconstruction of a neuron recorded and identified in a rat exploring a 2D environment (70 x 70 cm). Reconstructed dendrites and axon shown in red and blue, respectively. Scale bar, 100 μm.

(B) Schematic location of the cell in the parasubiculum. The cell is in the medial band of parasubiculum (blue), close to MEC (grey). Scale bar, 1000 μm.

(C) Representative raw traces of the recorded cell shown in (A). Note the prominent theta rhythms in LFP and theta modulated firing of the recorded cell.

(D) Spike-trajectory plot (left), rate map (middle) and two-dimensional spatial autocorrelation of the rate map (right) revealing the border firing. Spike-trajectory plot: red dots indicate spike locations; grey lines indicate the rat trajectory. Rate map: red indicates maximal firing rate, value noted above. Spatial autocorrelation: color scale -1 (blue) through 0 (green) to 1 (red).

(E) Polar plot of the cell's head-direction tuning. Value indicates maximum firing rate to the preferred direction.

(F) Autocorrelogram of spike discharges for the cell shown in (A).

(G) Theta-phase histogram of spikes for the cell shown in (A). For convenience, two repeated cycles are shown. The black sinusoid is a schematic local field potential theta wave for reference.

D = dorsal, L = lateral, M = medial, V = ventral.

In line with previous observations in linear mazes (Burgalossi et al., 2011), we also observed head-direction modulated responses (**Figure 28**); in fact, .a bout a third (35%; 8/23) of cells showed significant directional selectivity. The cell shown in **Figure 28A** was situated in the medial part of the

parasubiculum (**Figure 28B**) and also discharged in bursts with strong theta-rhythmicity (**Figure 28C**). The spikes were discharged throughout the enclosure without obvious spatial modulation (**Figure 28D**), but showed a clear head direction preference (**Figure 28E**). The spiking autocorrelogram also revealed a strong theta-rhythmicity (**Figure 28F**), and the spikes were also strongly locked to local theta oscillations (**Figure 28G**). In summary, in parasubiculum we observed an abundance of border cell activity and head-directional selectivity.

5.4.6 Theta-modulation of Parasubicular Neurons

As shown in representative cells (**Figure 27** and **Figure 28**), the large majority of parasubicular
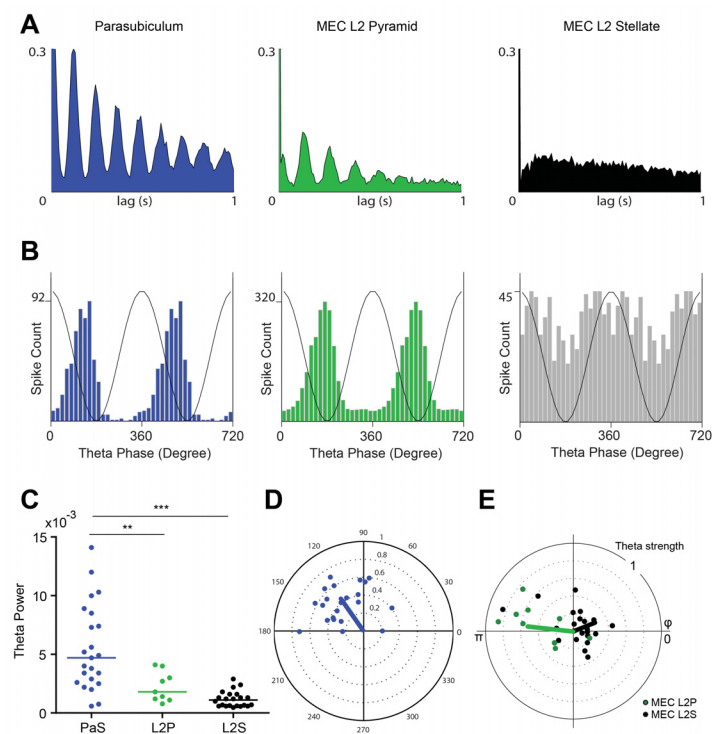
Figure 29: Theta modulation of parasubicular neurons comparing to layer 2 of MEC.
Data from layer 2 of medial entotorhinal cortex (MEC) come from the work of (Tang et al., 2014b) and are shown for comparison. (A) Representative autocorrelograms of spike discharges of identified cells recorded from parasubiculum (blue), MEC L2 pyramidal (green) and MEC L2 stellate (black) neurons. (B) Theta-phase histogram of spikes for the cells shown in (A). For convenience, two repeated cycles are shown. The black sinusoid is a schematic local field potential theta wave for reference. (C) Comparison of the strength of theta-rhythmicity in parasubiculum (blue), MEC L2 pyramid (green) and MEC L2 stellate (black) neurons. PaS cells show significantly higher theta modulation (Kruskal-Wallis test with Bonferroni correction). Lines indicate medians. (D) Polar plot of preferred theta-phase (theta-peak = 0°) and modulation strength (Rayleigh vector, 0-1, proportional to eccentricity) for parasubiculum neurons, dots = single cells, line = average. (E) Polar plot of preferred theta-phase (theta-peak = 0°) and modulation strength (Rayleigh vector, 0-1, proportional to eccentricity) for MEC L2 pyramid (green) and MEC L2 stellate (black), dots = single cells, lines = averages.

neurons (91%; 21/23) showed strong theta-rhythmic firing. Notably, theta-rhythmicity of parasubicular neurons exceeded several fold those of identified layer 2 neurons in medial entorhinal cortex (**Figure**

29A; see also Tang et al., 2014b). Parasubicular cells were also strongly locked to field potential theta oscillations, which were in phase with MEC theta (Glasgow and Chapman, 2007; **Figure 29B**); interestingly, parasubicular neurons discharged on average at a slightly earlier theta-phase (~45° phase angle, i.e. ~15 ms) than layer 2 pyramidal cell in medial entorhinal cortex (**Figure 29C**; MEC cells from the work of Tang et al., 2014b). On average, same as for the rhythmicity (**Figure 29C**), the strength of theta-phase locking in parasubicular neurons was also much stronger than those in layer 2 of medial entorhinal cortex (**Figure 29D,E**; MEC cells from Tang et al., 2014b). The strong theta-phase locking and rhythmicity of parasubicular neurons - the strongest within the parahippocampal area - suggest a role of the parasubiculum for imposing theta onto medial entorhinal cortex.

6.   Discussion

6.1   Functional Implications of a Pyramidal Cell Grid in Layer 2 of Medial Entorhinal Cortex

In the investigation of principal cells in layer 2 (Ray et al., 2014), we combined immunoreactivity, projection pattern, microcircuit analysis and in vivo electrophysiology. When we looked at layer 2 neurons in the tangential sections rather than in the classically-used parasagittal brain sections, we observed a remarkable regular arrangement of pyramidal cells by calbindin staining. Pyramidal neurons appeared to be clustered into patches arranged in a hexagonal grid, implying an astonishing similarity to the grid cell spatial firing. This hexagonal arrangement of calbindin patches is tightly anchored to other anatomical landmarks, and receives selective cholinergic innervation, a rhythmic drive critical for sustaining grid cell activity. Similarly, such clusters of pyramidal cells were also revealed by staining with Wfs1 marker co-localized with Calbindin (Kitamura et al., 2014). Both calbindin and Wfs1 could thus be powerful molecular markers to further develop genetic and optogenetic tools to selectively label and manipulate pyramidal cell activity in vivo to explore the functional contribution of pyramidal cells in spatial memory.

Using the juxtacellular recording technique described (Tang et al., 2014a; see Methods), we made the surprising observation that theta rhythmicity was about twofold stronger in pyramidal neurons than stellate neurons. Moreover, we showed in pharmacological experiments that the theta rhythmicity of pyramidal neurons depends on cholinergic drive (Ray et al., 2014). These results shed light on the cellular basis of theta rhythmicity in medial entorhinal cortex, and identified pyramidal neurons as the major receiver of theta inputs in layer 2. What is the cellular basis of theta-rhythmicity in MEC layer 2? Stellate cells have been prime candidates for theta discharges in layer 2 (Alonso and Llinás, 1989; Alonso and Klink, 1993), because intrinsic conductances make them resonate at theta frequency (Garden et al., 2008; Giocomo and Hasselmo, 2008). We found, however, that calbindin^{+} pyramidal cells show a twofold stronger theta-rhythmicity and theta phase-locking than calbindin^{-} stellate neurons. The stronger theta-rhythmicity of calbindin^{+} pyramidal neurons, which have weaker sag-currents (Alonso and Klink, 1993; Varga et al., 2010), is opposite from what had been predicted based on intrinsic properties (Hasselmo et al., 2007; Fernandez and White, 2008). Hence, layer 2 theta-modulation is cell type specific irrelative to cell-intrinsic resonance properties. This finding agrees with other evidence that questions a causal relationship between intrinsic properties and theta-rhythmicity in vivo (Fernandez and White, 2008; Giocomo et al., 2011; Schmidt-Hieber and Häusser, 2013). It is unlikely that the membrane properties of calbindin^{+} neurons contribute to the generation of theta rhythmicity (Varga et al., 2010).

The structure-function relationships of the layer 2 microcircuits we uncovered here (Ray et al., 2014), their remarkably precise geometry, which constrains information processing, their striking resemblance to the grid cell firing, and their unique physiological properties, will provide novel information for understanding entorhinal computations and its contribution to spatial cognition. These findings challenged the stellate-centered view of medial entorhinal cortex function, which has dominated the studies on the subject, and call for future experimental and computational work. The strong theta modulation suggests that pyramidal neurons might be the grid cells, which are confirmed to be strongly theta modulated. It remains unclear, where is the input source of these rhythmic inputs, which can be either from long-range medial septum projections or from upstream cortical structures, such as presubiculum or parasubiculum. Identifying the rhythmic source to these pyramidal cells will clarify the input topography and presumably help us understand the synaptic integration of grid cells.

Previous available evidence suggests that grid cells are a heterogeneous neuronal population in layer 2 (Domnisoru et al., 2013; Schmidt-Hieber and Häusser, 2013; Zhang et al., 2013) and indicates a weak structure-function relationship (Rowland and Moser, 2014). We however, observed strong similarities between calbindin+ neurons and grid cells (Ray et al., 2014): calbindin+ patches receive cholinergic inputs, which are required for grid cell activity (Newman et al., 2014); calbindin+ cells have strong theta-rhythmicity, a feature which correlates with grid cell discharge (Boccara et al., 2010); like grid cells, calbindin+ cells are clustered. Determining the spatial modulation patterns these identified cells will help clarify if and how the calbindin+ grid is related to grid cell activity, and the spatial firing properties of calbindin- stellate cells.

6.2   Structure-Function Relationship Revealed by Juxtacellular Recording Technique

This technique developed throughout the study has proven to be extremely powerful for exploring single-cell structure-function relationships in freely behaving rodents. As we have shown in our recent study (Ray et al., 2014), cell identity strongly predicted both neuronal connectivity and physiology in layer 2 of medial entorhinal cortex. Since our current experimental format meets the standards of tetrode recordings (Hafting et al., 2005; Solstad et al., 2008), we are now in the position to unequivocally identify spatially-modulated neurons (i.e. grid cells and head-direction cells) which form the basis of our internal representations of space. We provided (1) a mechanical description of our recording strategy, (2) a detailed procedure to obtain juxtacellular recordings in freely moving animals and (3) an overview of the method's performance, including the custom-made tools, and troubleshooting and technical tips, which are essential for the method to be established in other laboratories.

In our current dataset from freely-moving animals, in ~50% of the cases where labeling was attempted, a neuron was recovered (n= 53 identified cells out of 111 labeling attempts). Recording durations were up to 32 min, including all recordings (n = 417 from 209 rats; mean ± SD = 6.6 ± 4.1 min). The recording duration limited the range of questions that can be addressed with this method. The experimental design and animal behavior need to be optimized for obtaining sufficient information. It must however be noted that the recording durations reported here might be underestimated, since recordings in posterior or deep brain structures are known to be more unstable compared to anterior and superficial brain regions (Herfst et al., 2012; Domnisoru et al., 2013). Most recording losses occurred upon mechanical disturbances (i.e. head-bumps on the walls or head-shakes). Minimizing the occurrence of such events by using soft foam materials as cushion, and reducing the stress of the animal by careful habituation to the experimental procedures, has a strong impact in our experience on the recording duration and/or stability.

The techniques and procedures described here are optimized for rats, but can be potentially adapted for recording in other animal species. For smaller animals (i.e. mice), further miniaturization of the implant components and/or use of lighter construction materials (i.e. aluminum) should be considered. The applicability of this protocol is in principle not restricted by brain area or recording depth, as a "clean" pipette tip is beneficial but not a necessity for the establishment of juxtacellular recordings (unlike whole-cell recordings, electrodes can typically be used for multiple penetrations and without positive air pressure. Application of air pressure might however be essential for recording in very deep brain structures (i.e. > 4-5 mm from the pial surface) to avoid pipette clogging. The method described is focused on exploratory behavior, but can certainly be extended to many forms of unrestrained natural or trained behaviors. Success rates will depend on the experimenter, the target region, cell type and behavior.

The procedures illustrated in the present method (Tang et al., 2014a), consisting of a combination of animal training, electrophysiological recording and juxtacellular labeling procedures (Pinault, 1996; Pinault and Deschênes, 1998), enable anatomical visualization of single neurons recorded in freely-moving animals, engaged in exploratory behavior (see Ray et al., 2014). The methods described here include two key methodological developments over our previous procedures in (Burgalossi et al., 2011; Herfst et al., 2012): recordings are obtained in awake, drug-free animals, trained to run in large open field environments; "head-anchoring" stabilization procedures (Lee et al., 2009; Burgalossi et al., 2011; Herfst et al., 2012) are replaced by a removable stabilization seal, which enables multiple penetrations and recording/labeling attempts to be performed in the same animal. Fluorescent dyes for neuronal labeling (Judkewitz et al., 2009) could potentially be used for increasing the number of recovered

neurons. Other neuronal tracers, such as Biotinylated Dextran Amines (i.e. BDA-3000), which are more resistant to intracellular degradation (Veenman et al., 1992), could be used for improved visualization of long-range axonal projections, as they can be recovered up to a few days after labeling (Deschênes et al., 1994; Furuta et al., 2009; Pinault, 2011). The use of long taper, low-resistance electrodes, together with close proximity of cell, ensures high signal-to-noise ratio of juxtacellular spike signals (Burgalossi et al., 2011; Herfst et al., 2012) and unequivocal spike identification. Future technical improvements would be to realize the juxtacellular electroporation of powerful genetic tools such as small molecule DNAs and virus (Daniel et al., 2013), making it possible to conduct single cell chronic, cell-type specific investigations of synaptic input / output relationships and neural circuit coordinations in behaving animals.

6.3   Cell-type Specificity in Layer 2 of Medial Entorhinal Cortex

Triggered by the discovery that pyramidal neurons in layer 2 form a grid-like microcircuit (Ray et al, 2014), we further directly assessed the relationship between spatial firing pattern and different cell types. By taking advantage of the improved methodologies for identifying individual neurons recorded in freely moving animals described above (Tang et al., 2014a), as well as by cell identification and theta-locking based classification of unidentified recordings, we provided evidence that grid and border responses are preferentially contributed by pyramidal and stellate cells, respectively (Tang et al., 2014b).

In layer 2 of medial entorhinal cortex, most studies suggested that spatially-modulated responses are common, and that grid firing patterns can emerge in both stellate and pyramidal neurons (Burgalossi et al., 2011; Domnisoru et al., 2013; Schmidt-Hieber and Häusser, 2013; Zhang et al., 2013). In line with such evidence, we observed a large fraction of spatially-modulated neurons in layer 2; weakly hexagonal firing patterns in both stellate and pyramidal neurons. However, most grid cells (see Methods) were classified as putative calbindin^{+} pyramidal cells. Border cells, on the other hand, were predominantly observed in the calbindin^{-} stellate cells. We made our conclusion based on (1) the identification of calbindin[+] grid and calbindin^{-} border cells (see **Figure 17**) and (2) spike-timing based classification of unidentified layer 2 recordings, according to the striking differences of calbindin[+] and calbindin^{-} cells in their temporal discharge properties (Ray et al., 2014), the assessment of classification quality by our boot-strapping approach, and the robustness of classification across different datasets. The validity and accuracy of our classification procedure are critical to the study (Tang et al., 2014b).

A surprising finding is that layer 2 principal cells can be classified with high accuracy by their distinct temporal discharge properties (Tang et al., 2014b). Potentially, such classification can be

extended to a large number of unidentified layer 2 recordings from other laboratories, provided that the required histology and LFP data have been collected. Such post-hoc assignment of cell types to recording data – i.e. supplying identity to blind extracellular recordings – could be instrumental for understanding principal cell diversity and cortical microcircuitry.

Calbindin^{+} pyramidal cells might be predetermined for grid cell function as they receive cholinergic inputs, are strongly theta-modulated, and arranged in a hexagonal grid (Ray et al., 2014). We suggested an 'isomorphic mapping hypothesis' according to which an anatomical grid of pyramidal cells (Ray et al., 2014) generates grid cell activity (Brecht et al., 2014) and is an embodiment of the brain's representation of space in hexagonal grids. Representing grid discharge by a 'cortical grid' might offer similar advantages as isomorphic representations of body parts as barrel fields (Woolsey and van der Loos, 1970) or nose stripes (Catania et al., 1993) in somatosensory cortices of tactile specialists. Notably, the local similarity of grid cell discharges is high, as neighboring grid cells share the same grid orientation, scaling and are phase-coupled even across distinct environments (Hafting et al., 2005; Fyhn et al., 2007). We speculate that calbindin[+] pyramidal neuron clustering and apical dendrite bundling in patches (Ray et al., 2014) might impose this local similarity of grid discharges. Border responses on the other hand, arise in stellate neurons, with long and widely diverging dendritic trees, may result from a relatively global sampling of incoming inputs in medial entorhinal cortex and help generate place cell activity (Bjerknes et al., 2014; Bush et al., 2014). Recognizing the functional dichotomy of pyramidal and stellate cells in layer 2 will help elucidate how spatial discharge patterns arise in cortical microcircuits (**Figure 30**; Tang et al., 2014b).
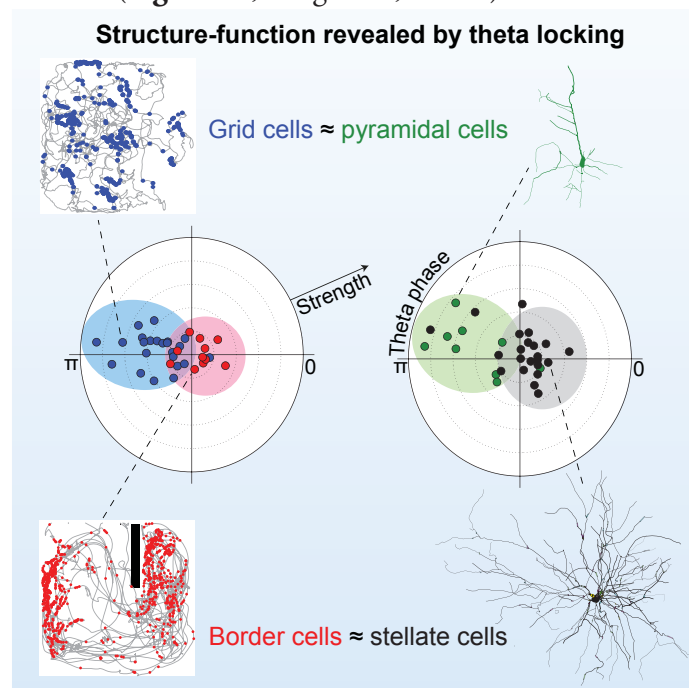

Figure 30: Schematic view of cell type specificity of grid and border cells in layer 2 of Medial Entorhinal Cortex.

6.4 Functional Architecture of the Parasubiculum

Our analysis indicates that the parasubiculum is in many regards distinct from other parahippocampal structures. The elongated shape of the parasubiculum, an almost linear arrangement of neurons, differs from the map-like 2D layout of the granule cells in the dentate gyrus, CA3, CA2, CA1, subiculum, presubiculum and medial or lateral entorhinal cortex (Amaral and Witter, 1989; Cenquizca and Swanson, 2007). Further, the apparent absence of directly-associated deep layers distinguishes the parasubiculum from the surrounding entorhinal, retrosplenial and presubicular cortices. The circumcurrent axons (Burgalossi et al., 2011; see also **Figure 24B**) that traverse the parasubiculum and establish a 'global' connectivity is also a unique feature of parasubicular anatomy, which could suggest a strongly recurrent network organization, possibly underlying the strong rhythmicity we detected. Furthermore, the parasubiculum is a preferred target of medial septal inputs and provides the major output to pyramidal neuron patches in layer 2 of medial entorhinal cortex. We observed a substantially larger fraction of border responses in the parasubiculum than in the adjacent medial entorhinal cortex (Solstad et al., 2008; Tang et al., 2014b), where such responses are fairly rare. The theta-modulation of parasubicular neurons exceeds that observed in other parahippocampal structures. Altogether, these are uniquely defining features of the parasubiculum, which distinguish it from neighboring parahippocampal cortices.

Our anatomical analysis agrees well with earlier descriptions that large parts of the parasubiculum are situated between the medial entorhinal cortex and the presubiculum (Amaral and Witter, 1989; Cenquizca and Swanson, 2007), however we provide evidence that the parasubiculum extends further laterally than previously estimated (Boccara et al., 2010) and this structure is not directly associated with deep layers. The idea that the parasubiculum extends dorso-laterally from the medial entorhinal cortex is based on three observations: (i) staining of cholinergic markers, calbindin immunoreactivity or cytochrome oxidase activity all delineate a continuous band, which extends dorso-laterally to the medial entorhinal cortex (**Figure 23**); similarly, both (ii) the modular structure of the large patches (**Figure 24A,B**) and (iii) circumcurrent axons extend as a continuous dorso-lateral band. Our conclusion that the parasubiculum extends dorso-laterally is strongly supported by recent work that applied high resolution mapping of gene expression in the medial entorhinal cortex and surrounding structures (Ramsden et al., 2015). The authors not only observed that this dorsolateral part is different from medial entorhinal cortex, but also showed that it shares patterns of gene expression with the parasubiculum (Ramsden et al., 2015). The extent to which deep layers were assigned to the parasubiculum differs in the literature. While some studies assigned deep layers to the parasubiculum (Funahashi and Stewart, 1997; Glasgow and Chapman, 2007; Boccara et al., 2010), other work found it difficult to assign

adjacent deep layers to either the presubiculum or the parasubiculum based solely on cytoarchitectonic criteria (Mulders et al., 1997). Our assessment that these deep layer cells should not be viewed as part of the parasubiculum is based on three observations: (i) the shape of dorsal part of the parasubiculum, as revealed by cholinergic markers, calbindin immunoreactivity or cytochrome oxidase activity, delineates only a "superficial-layer structure" encompassing layer 1-3, but not extending beyond the lamina disseccans (Burgalossi et al., 2011); (ii) we did not observe axons from the superficial parasubiculum into adjacent deep cortical layers; (iii) we did not observe axons from the adjacent deep cortical layers into the superficial parasubiculum. The idea that large parts of the parasubiculum lack deep layers is again supported by the gene expression analysis of Ramsden et al., 2015. This pattern of connectivity is very different from the adjacent deep layers of the medial entorhinal cortex, which heavily innervate superficial layers (Beed et al., 2010; Burgalossi and Brecht, 2014).

Our results agree with previous extracellular recording data that also revealed the presence of spatially-modulated neurons in the parasubiculum (Taube, 1995; Cacucci et al., 2004; Boccara et al., 2010; Burgalossi et al., 2011). In particular, our findings are in line with previous results, which described spatially-modulated, directional and theta-rhythmic responses in the parasubiculum (Cacucci et al., 2004). The present data are also consistent with the study of (Boccara et al., 2010), where the authors described border and head-direction responses in the parasubiculum. Notably, the strong head-direction tuning in the parasubiculum is also consistent with previous (Fyhn et al., 2008; Wills et al., 2010) and more recent work (Giocomo et al., 2014), where the large majority of sharply-tuned head-direction cells were recorded "near" the dorsalmost border medial entorhinal cortex, compatible with a parasubicular origin (**Figure 23**; Burgalossi et al., 2011). We recognized that ascertaining the origin of extracellularly recorded units here is particularly difficult - especially at more lateral sites, where the parasubiculum gets progressively thinner. While our identified cell data provide great certainty about the parasubicular location of the recorded cells, the strength of our conclusions is however limited by the relatively small dataset.

We argue that the parasubicular response properties observed match well with the inputs described by other authors and us. Parasubicular head-direction selectivity is in line with its inputs from anterior thalamus and presubiculum, two key structures in the head-direction system (Taube, 2007). The border responses observed here are in line with subicular inputs, as numerous boundary-vector cells have been observed there (Lever et al., 2009). Finally, one of the most prominent aspects of parasubicular activity is the strong theta-modulation and rhythmicity of spike discharges. Unusually large membrane-potential theta oscillations have also been recorded from parasubicular neurons in awake animals (termed "large-theta"; Domnisoru et al., 2013). We argue that such strong entrainment

may result from the massive GABAergic innervation from the medial septum, since GABAergic cells in the medial septum are known to be a key theta-pacemaker in the entorhinal-hippocampal network (Buzsáki, 2002; Hangya et al., 2009; Brandon et al., 2011; Koenig et al., 2011).

One of the most interesting aspects of the current data lies in the possible relationship between the parasubiculum and layer 2 of medial entorhinal cortex, where grid cells are commonly found (Sargolini et al., 2006; Boccara et al., 2010). Grid cells are distinct from other neurons in the medial entorhinal cortex in their strong theta-rhythmicity of spiking (Boccara et al., 2010). It is therefore most interesting that the strongly theta-rhythmic parasubicular cells project selectively into layer 2 pyramidal cell patches, where neurons show strong entrainment by the theta-rhythm (Ray et al., 2014) and where most grid cells might be located (Tang et al., 2014b). The discharge timing might be consistent with an activation/entrainment of layer 2 pyramidal cells by parasubicular inputs, as parasubicular neurons discharge on average at an earlier theta-phase (~45° phase angle, i.e. ~15 ms) than layer 2 pyramidal cells (**Figure 29D,E**). The parasubicular input to layer 2 pyramidal cells is also remarkable, in light of the little excitatory connectivity within layer 2 of medial entorhinal cortex (Couey et al., 2013; Pastoll et al., 2013). We speculate that parasubicular input could be important for two aspects: (i) for imposing theta-rhythmicity on grid responses, and possibly also contributing to their temporal spike dynamics, like phase-precession (Hafting et al., 2008) and (ii) parasubicular border responses could be instrumental in anchoring grids to environmental boundaries. Interestingly, direct projections from border to grid cells have been recently postulated, which might be responsible for determining grid orientation and ellipticity. In addition, grid cells have been shown to receive head-directional inputs (Bonnevie et al., 2013). The parasubiculum might be the source of this input, given the large-fraction of head-direction cells and the strong inputs to layer 2. We conclude that parasubicular input to the grid system should be an important subject of further functional analysis.

What does the parasubiculum do and how does it operate? As the studies of parasubicular circuits are in an early stage, we lack information to definitely answer this question. Tentatively, it seems likely that the parasubiculum plays a key role in determining spike-timing of downstream neurons relative to theta oscillations. The massive internal connectivity of the parasubiculum by circumcurrent axons is also a remarkably and unique feature. These axons connect along the dorso-ventral axis of the parahippocampal cortex. As different spatial scales are mapped onto the dorsoventral axis of the medial entorhinal cortex (Brun et al., 2008), we wonder, if these axons ensure that those parasubicular neurons along the dorsoventral axis signaling the same positions (at different spatial scales) fire at the same time relative to the theta cycle.

Another peculiar aspect of parasubicular anatomy is the lack of direct output to the hippocampus.

Together with the absence of deep layers (the recipient of CA1/subicular back-projections in the medial entorhinal cortex) and a thinner layer 1, it seems that the parasubiculum is only poorly connected to the classic 'memory circuits'. We envision it may function more for providing online spatial information like a pointer (where am I) than for long-term storage of information. This pointer hypothesis might be consistent with the deficits in working memory observed after parasubicular lesions (Kesner and Giles, 1998). Again, we admit that these ideas are speculative at this early stage.

6.5   Summary and Future Directions

By combining anatomy (Ray et al., 2014), methodological development (Tang et al., 2014a) and electrophysiological recordings (Tang et al., 2014b), we provided an in depth analysis of the microcircuitry structure and function in layer 2 of MEC and parasubiculum. The striking cell-type specificity of spatial representations in layer 2 of MEC is contrary to long-standing assumptions: (i) pyramidal neurons (not stellate neurons as classically thought) are the cellular substrate of grid cells; (ii) layer 2 grid cells do not project to the dentate gyrus; (iii) stellate neurons, the major projection neurons to the dentate gyrus, encode the environmental boundaries. These findings will have strong implications for understanding the cellular basis of spatial cognition, and will certainly lay the ground for new models of spatial memory in hippocampal formation, which do not rely on the assumption that stellate-grid neurons output to the dentate gyrus. In the parasubiculum, strong theta rhythmicity and direct projection to layer 2 pyramidal neurons, together with a large fracion of head-direction and border cells, suggest grid cells in layer 2 of MEC might receive theta-rhythmic directional and boundary information from parasubiculum. This discovery is also of fundamental importance for our understanding of spatial memory in general, and might shed light on more general principles of memory formation in the mammalian cortex. Technologically, the powerfulness of juxtacellular recording in freely moving animals will open a new frontier of systems neuroscience research at single cell resolution in awake behaving animals.

The results presented here also raised many intriguing and potentially very important questions. The primary projection pattern of layer 2 pyramidal cells remains mysterious. Several lines of evidence suggest different cortical targets (Varga et al., 2010; Kitamura et al., 2014). Clarifying the projections of these pyramidal cells, will provide essential information on the downstream targets of grid cells. MEC layer 2 and layer 3 receive differential projections from parasubiculum and presubiculum. Elucidating whether directional and spatial information have distinct pathways into different layers in MEC, and what is the functional contribution of theta oscillations within the entorhinal-hippocampal loop, will eventually provide a deeper understanding of the neuronal mechanisms of spatial representation.

7.   Abbreviations

MEC	medial entorhinal cortex
PrS	presubiculum
PaS	parasubiculum
FS	fast spiking
CCK	cholecystokinin
GABA	γ-aminobutyric acid
UV	ultraviolet
HEPES	4-(2-hydroxyethyl)-1-piperazineethanesulfonic acid
BDA	biotinylated dextran amines
LED	light-emitting diode
approx.	approximate
PFA	paraformaldehyde
PB	phosphate buffer
AChE	acetylcholinesterase
CS	saline solution
DAB	diaminobenzidine
BSA	bovine serum albumin
RT	room temperature
LFP	local field potential
CTB	cholera toxin subunit B
p.s.i.	pounds per sqaure inch
VAChT	vesicular acetylcholine transporter
ROI	regions of interest
i.p.	intraperitoneal
mm	millimeter
CA	cornu ammonis
mV	millivolt
ms	millisecond
nA	nanoampere
L	layer
min	minutes
S.E.M.	standard error of the mean
S.D.	standard deviation
µA	microampere

8.   References

Alonso, A., and Klink, R. (1993). Differential electroresponsiveness of stellate and pyramidal-like cells of medial entorhinal cortex layer II. J. Neurophysiol. 70, 128-143.

Alonso, A., and Llinás, R.R. (1989). Subthreshold Na+-dependent theta-like rhythmicity in stellate cells of entorhinal cortex layer II. Nature 342, 175-177.

Amaral, D.G., and Witter, M.P. (1989). The three-dimensional organization of the hippocampal formation: a review of anatomical data. Neuroscience 31:571–591.

Andersen, P., Bliss, T.V.P., Skrede, K.K., Lomo, T., and Olsen, L.I. (1971). Lamellar organization of hippocampal excitatory pathways. Exp. Brain Res. 13:222–238.

Anikeeva, P., Andalman, A.S., Witten, I., Warden, M., Goshen, I., Grosenick, L., Gunaydin, L.A., Frank, L.M., and Deisseroth, K. (2011). Optetrode: a multichannel readout for optogenetic control in freely moving mice. Nat. Neurosci. 15, 163-170.

Aravanis, A.M., Wang, L.-P., Zhang, F., Meltzer, L.A., Mogri, M.Z., Schneider, M.B., and Deisseroth, K. (2007). An optical neural interface: in vivo control of rodent motor cortex with integrated fiberoptic and optogenetic technology. J. Neural Eng. 4, 143-156.

Ascoli, G.A., Alonso-Nanclares, L., Anderson, S.A., Barrionuevo, G., Benavides-Piccione, R., Burkhalter, A., Buzsáki, G., Cauli, B., Defelipe, J., Fairén, A., et al. (2008). Petilla terminology: nomenclature of features of GABAergic interneurons of the cerebral cortex. Nat. Rev. Neurosci. 9, 557-568.

Barry, C., Ginzberg, L.L., O'Keefe, J., and Burgess, N. (2012). Grid cell firing patterns signal environmental novelty by expansion. Proc. Natl. Acad. Sci. U S A. 109, 17687-92.

Barry, C., Bush, D., O'Keefe, J., and Burgess, N. (2012). Models of grid cells and theta oscillations. Nature 488, 103.

Barry, C., Heys, J.G., and Hasselmo, M.E. (2012). Possible role of acetylcholine in regulating spatial novelty effects on theta rhythm and grid cells. Front. Neural Circuits 6, 5.

Battaglia, D., Karagiannis, A., Gallopin, T., Gutch, H.W., and Cauli, B. (2013). Beyond the frontiers of neuronal types. Front. Neural Circuits 7, 13.

Beed, P., Bendels, M.H.K., Wiegand, H.F., Leibold, C., Johenning, F.W., and Schmitz, D. (2010). Analysis of Excitatory Microcircuitry in the Medial Entorhinal Cortex Reveals Cell-Type-Specific Differences. Neuron 68:1059–1066.

Bjerknes, T.L., Moser, E.I., and Moser, M.-B. (2014). Representation of Geometric Borders in the Developing Rat. Neuron 82, 71–78.

Blackstad, T.W. (1956). Commissural connections of the hippocampal region in the rat, with special reference to their mode of termination. J. Comp. Neurol. 105, 417–537.

Boccara, C.N., Sargolini, F., Thoresen, V.H., Solstad, T., Witter, M.P., Moser, E.I., and Moser, M.-B. (2010). Grid cells in pre- and parasubiculum. Nat. Neurosci. 13, 987–994.

Bonnevie, T., Dunn, B., Fyhn, M., Hafting, T., Derdikman, D., Kubie, J.L., Roudi, Y., Moser, E.I., and Moser, M.-B. Grid cells require excitatory drive from the hippocampus. (2013). Nat. Neurosci. 16, 309-17.

Boucetta, S., Cisse, Y., Mainville, L., Morales, M., and Jones, B.E. (2014). Discharge Profiles across the Sleep-Waking Cycle of Identified Cholinergic, GABAergic, and Glutamatergic Neurons in the Pontomesencephalic Tegmentum of the Rat. J. Neurosci. 34, 4708–4727.

Brandon, M.P., Bogaard, A.R., Libby, C.P., Connerney, M.A., Gupta, K., and Hasselmo, M.E. (2011). Reduction of theta rhythm dissociates grid cell spatial periodicity from directional tuning. Science 332, 595–599.

Brecht, M., Ray, S., Burgalossi, A., Tang, Q., Schmidt, H., and Naumann, R. (2014). An isomorphic mapping hypothesis of the grid representation. Philos. Trans. R. Soc. Lond. B. Biol. Sci. 369, 20120521.

Brown, S.P., and Hestrin, S. (2009). Cell-type identity: a key to unlocking the function of neocortical circuits. Curr. Opin. Neurobiol. 19, 415–421.

Brun, V.H., Solstad, T., Kjelstrup, K.B., Fyhn, M., Witter, M.P., Moser, E.I., and Moser, M.-B. (2008). Progressive increase in grid scale from dorsal to ventral medial entorhinal cortex. Hippocampus 18:1200–1212.

Burgalossi, A., and Brecht, M. (2014). Cellular, columnar and modular organization of spatial representations in medial entorhinal cortex. Curr. Opin. Neurobiol. 24, 47–54.

Burgalossi, A., Herfst, L., von Heimendahl, M., Förste, H., Haskic, K., Schmidt, M., and Brecht, M. (2011). Microcircuits of Functionally Identified Neurons in the Rat Medial Entorhinal Cortex. Neuron 70, 773–786.

Bush, D., Barry, C., and Burgess, N. (2014). What do grid cells contribute to place cell firing? Trends. Neurosci. 37,136-45.

Buzsáki, G. (2002). Theta oscillations in the hippocampus. Neuron 33:325–340.

Caballero-Bleda, M., and Witter, M.P. (1993). Regional and laminar organization of projections from the presubiculum and parasubiculum to the entorhinal cortex: an anterograde tracing study in the rat. J. Comp. Neurol. 328, 115-129.

Caballero-Bleda, M., and Witter, M.P. (1994). Projections from the presubiculum and the parasubiculum to morphologically characterized entorhinal-hippocampal projection neurons in the rat. Exp. Brain Res. 101:93–108.

Cacucci, F., Lever, C., Wills, T.J., Burgess, N., and O'Keefe, J. (2004). Theta-modulated place-by-direction cells in the hippocampal formation in the rat. J. Neurosci. 24:8265–8277.

Canto, C.B., Koganezawa, N., Beed, P., Moser, E.I., and Witter, M.P. (2012). All layers of medial entorhinal cortex receive presubicular and parasubicular inputs. J. Neurosci. 32:17620–17631.

Canto, C.B., and Witter, M.P. (2012). Cellular properties of principal neurons in the rat entorhinal cortex. II. The medial entorhinal cortex. Hippocampus 22, 1277–1299.

Cardin, J.A., Carlén, M., Meletis, K., Knoblich, U., Zhang, F., Deisseroth, K., Tsai, L.-H., and Moore, C.I. (2010). Targeted optogenetic stimulation and recording of neurons in vivo using cell-type-specific expression of Channelrhodopsin-2. Nat. Protoc. 5, 247–254.

Catania, K.C., Northcutt, R.G., Kaas, J.H., and Beck, P.D. (1993). Nose stars and brain stripes. Nature 364, 493.

Cenquizca, L.A., and Swanson, L.W. (2007). Spatial organization of direct hippocampal field CA1 axonal projections to the rest of the cerebral cortex. Brain Res. Rev. 56:1–26.

Chung, K., Wallace, J., Kim, S.-Y., Kalyanasundaram, S., Andalman, A.S., Davidson, T.J., Mirzabekov, J.J., Zalocusky, K. a, Mattis, J., Denisin, A.K., et al. (2013). Structural and molecular interrogation of intact biological systems. Nature 497, 332–337.

Couey, J.J., Witoelar, A., Zhang, S.-J., Zheng, K., Ye, J., Dunn, B., Czajkowski, R., Moser, M.-B., Moser, E.I., Roudi, Y., and Witter, M.P. (2013). Recurrent inhibitory circuitry as a mechanism for grid formation. Nat. Neurosci. 16:318–324.

Daniel, J., Polder, H.R., Lessmann, V., and Brigadski, T. (2013). Single-cell juxtacellular transfection and recording technique. Pflugers Arch. 465, 1637-1649.

Deisseroth, K., and Schnitzer, M.J. (2013). Engineering approaches to illuminating brain structure and dynamics. Neuron 80, 568–577.

Denk, W., Briggman, K.L., and Helmstaedter, M. (2012). Structural neurobiology: missing link to a mechanistic understanding of neural computation. Nat. Rev. Neurosci. 13, 351–358.

Deschênes, M., Bourassa, J., and Pinault, D. (1994). Corticothalamic projections from layer V cells in rat are collaterals of long-range corticofugal axons. Brain Res. 664, 215–219.

Ding, S.L. (2013). Comparative anatomy of the prosubiculum, subiculum, presubiculum, postsubiculum, and parasubiculum in human, monkey, and rodent. J. Comp. Neurol. 521:4145-62.

Domnisoru, C., Kinkhabwala, A. a, and Tank, D.W. (2013). Membrane potential dynamics of grid cells. Nature 495, 199–204.

Dong, H.-W., Swanson, L.W., Chen, L., Fanselow, M.S., and Toga, A.W. (2009). Genomic-anatomic evidence for distinct functional domains in hippocampal field CA1. Proc. Natl. Acad. Sci. U. S. A. 106, 11794–11799.

Fenno, L., Yizhar, O., and Deisseroth, K. (2011). The development and application of optogenetics. Annu. Rev. Neurosci. 34, 389–412.

Fernandez, F.R., and White, J.A. (2008). Artificial synaptic conductances reduce subthreshold oscillations and periodic firing in stellate cells of the entorhinal cortex. J. Neurosci. 28, 3790–3803.

Fujimaru, Y., and Kosaka, T. (1996). The distribution of two calcium binding proteins, calbindin D-28K and parvalbumin, in the entorhinal cortex of the adult mouse. Neurosci. Res. 24, 329–343.

Fujise, N., Hunziker, W., Heizmann, C.W., and Kosaka, T. (1995). Distribution of the calcium binding proteins, calbindin D-28K and parvalbumin, in the subicular complex of the adult mouse. Neurosci. Res. 22:89–107.

Funahashi, M., and Stewart, M. (1997). Presubicular and parasubicular cortical neurons of the rat: Functional separation of deep and superficial neurons in vitro. J. Physiol. 501:387–403.

Furuta, T., Kaneko, T., and Deschênes, M. (2009). Septal neurons in barrel cortex derive their receptive field input from the lemniscal pathway. J. Neurosci. 29, 4089–4095.

Fyhn, M., Hafting, T., Treves, A., Moser, M.-B., and Moser, E.I. (2007). Hippocampal remapping and grid realignment in entorhinal cortex. Nature 446, 190-4.

Fyhn, M., Hafting, T., Witter, M.P., Moser, E.I., and Moser, M.-B. (2008). Grid cells in mice. Hippocampus 18:1230-8.

Garden, D.L.F., Dodson, P.D., O'Donnell, C., White, M.D., and Nolan, M.F. (2008). Tuning of synaptic integration in the medial entorhinal cortex to the organization of grid cell firing fields. Neuron 60, 875–889.

Gatome, C.W., Slomianka, L., Lipp, H.P., and Amrein, I (2010). Number estimates of neuronal phenotypes in layer II of the medial entorhinal cortex of rat and mouse. Neuroscience 170, 156-65.

Geneser, F.A. (1986). Distribution of acetylcholinesterase in the hippocampal region of the rabbit: I. Entorhinal area, parasubiculum, and presubiculum. J. Comp. Neurol. 254:352–368.

Germroth, P., Schwerdtfeger, W.K., and Buhl, E.H. (1989). Morphology of identified entorhinal neurons projecting to the hippocampus. A light microscopical study combining retrograde tracing and intracellular injection. Neuroscience 30, 683–691.

Giocomo, L.M., and Hasselmo, M.E. (2008). Time constants of h current in layer ii stellate cells differ along the dorsal to ventral axis of medial entorhinal cortex. J. Neurosci. 28, 9414–9425.

Giocomo, L.M., Hussaini, S.A., Zheng, F., Kandel, E.R., Moser, M.-B., and Moser, E.I. (2011). Grid cells use HCN1 channels for spatial scaling. Cell 147, 1159–1170.

Giocomo, L.M., Stensola, T., Bonnevie, T., van Cauter, T., Moser, M.-B., and Moser, E.I. (2014). Topography of head direction cells in medial entorhinal cortex. Curr. Biol. 24:252–262.

Glasgow, S.D., and Chapman, C.A. (2007). Local generation of theta-frequency EEG activity in the parasubiculum. J. Neurophysiol. 97:3868–3879.

van Groen, T., and Wyss, J.M. (1990). The connections of presubiculum and parasubiculum in the rat. Brain Res. 518:227–243.

van Groen, T., and Wyss, J.M. (1992). Projections from the laterodorsal nucleus of the thalamus to the limbic and visual cortices in the rat. J. Comp. Neurol. 324:427–448.

Gupta, K., Keller, L.A., and Hasselmo, M.E. (2012). Reduced spiking in entorhinal cortex during the delay period of a cued spatial response task. Learn. Mem. 19, 219-230.

Hafting, T., Fyhn, M., Molden, S., Moser, M.-B., and Moser, E.I. (2005). Microstructure of a spatial map in the entorhinal cortex. Nature 436, 801–806.

Hafting, T., Fyhn, M., Bonnevie, T., Moser, M.-B., and Moser, E. I. (2008). Hippocampus-independent phase precession in entorhinal grid cells. Nature 453, 1248–1252.

Hangya, B., Borhegyi, Z., Szilágyi, N., Freund, T.F., and Varga, V. (2009). GABAergic neurons of the medial septum lead the hippocampal network during theta activity. J. Neurosci. 29:8094–8102.

Hasselmo, M. E., and McGaughy, J. (2004). High acetylcholine levels set circuit dynamics for attention and encoding and low acetylcholine levels set dynamics for consolidation. Prog. Brain Res. 145, 207–231.

Hasselmo, M. E., Giocomo, L. M., and Zilli, E. A. (2007). Grid cell firing may arise from interference of theta frequency membrane potential oscillations in single neurons. Hippocampus 17, 1252–1271.

Harris, K.D., and Mrsic-Flogel, T.D. (2013). Cortical connectivity and sensory coding. Nature 503, 51–58.

von Heimendahl, M., Rao, R.P., and Brecht, M. (2012). Weak and nondiscriminative responses to conspecifics in the rat hippocampus. J. Neurosci. 6, 2129-2141.

Herfst, L., Burgalossi, A., Haskic, K., Tukker, J.J., Schmidt, M., and Brecht, M. (2012). Friction-based stabilization of juxtacellular recordings in freely moving rats. J. Neurophysiol. 108, 697–707.

Heys, J.G., Schultheiss, N.W., Shay, C.F., Tsuno, Y., and Hasselmo, M.E. (2012). Effects of acetylcholine on neuronal properties in entorhinal cortex. Front. Behav. Neurosci. 6, 32.

Honda, Y., and Ishizuka, N. (2004). Organization of Connectivity of the Rat Presubiculum: I. Efferent Projections to the Medial Entorhinal Cortex. J. Comp. Neurol. 473:463–484.

Horikawa, K., and Armstrong, W.E. (1988). A versatile means of intracellular labeling: injection of biocytin and its detection with avidin conjugates. J. Neurosci. Methods 25, 1–11.

Houweling, A., and Brecht, M. (2008). Behavioral report of single neurons stimulation in somatosensory cortex. Nature 451, 65–69.

Houweling, A.R., Doron, G., Voigt, B.C., Herfst, L.J., and Brecht, M. (2010). Nanostimulation: manipulation of single neuron activity by juxtacellular current injection. J. Neurophysiol. 103, 1696-1704.

Huang, Q., Zhou, D., and DiFiglia, M. (1992). Neurobiotin(TM), a useful neuroanatomical tracer for in vivo anterograde, retrograde and transneuronal tract-tracing and for in vitro labeling of neurons. J. Neurosci. Methods 41, 31–43.

Ichinohe, N., Knight, A., Ogawa, M., Ohshima, T., Mikoshiba, K., Yoshihara, Y., Terashima, T., and Rockland, K.S. (2008). Unusual patch-matrix organization in the retrosplenial cortex of the reeler mouse and Shaking rat Kawasaki. Cereb. Cortex 18, 1125–1138.

Jährling, N., Becker, K., Kramer, E.R., and Dodt, H.-U. (2008). 3D-Visualization of nerve fiber bundles by ultramicroscopy. Med. Laser Appl. 23, 209–215.

Judkewitz, B., Rizzi, M., Kitamura, K., and Häusser, M. (2009). Targeted single-cell electroporation of mammalian neurons in vivo. Nat. Protoc. 4, 862–869.

Kamme, F., Salunga, R., Yu, J., Tran, D.-T., Zhu, J., Luo, L., Bittner, A., Guo, H.-Q., Miller, N., Wan, J., et al. (2003). Single-cell microarray analysis in hippocampus CA1: demonstration and validation of cellular heterogeneity. J. Neurosci. 23, 3607–3615.

Kepecs, A., and Fishell, G. (2014). Interneuron cell types are fit to function. Nature 505, 318–326.

Kerr, J.N.D., de Kock, C.P.J., Greenberg, D.S., Bruno, R.M., Sakmann, B., and Helmchen, F. (2007). Spatial organization of neuronal population responses in layer 2/3 of rat barrel cortex. J. Neurosci. 27, 13316–13328.

Kesner, R.P., and Giles, R. (1998). Neural circuit analysis of spatial working memory: role of pre- and parasubiculum, medial and lateral entorhinal cortex. Hippocampus 8:416–423.

Kitamura, T., Pignatelli, M., Suh, J., Kohara, K., Yoshiki, A., Abe, K., and Tonegawa, S. (2014). Island cells control temporal association memory. Science 343, 896-901.

Klausberger, T., and Somogyi, P. (2008). Neuronal diversity and temporal dynamics: the unity of hippocampal circuit operations. Science 321, 53–57.

Klausberger, T., Magill, P.J., Márton, L.F., Roberts, J.D.B., Cobden, P.M., Buzsáki, G., and Somogyi, P. (2003). Brain-state- and cell-type-specific firing of hippocampal interneurons in vivo. Nature 421, 844–848.

Klink, R., and Alonso, A. (1997). Muscarinic modulation of the oscillatory and repetitive firing properties of entorhinal cortex layer II neurons. J. Neurophysiol. 77, 1813–1828.

de Kock, C.P.J., and Sakmann, B. (2009). Spiking in primary somatosensory cortex during natural whisking in awake head-restrained rats is cell-type specific. Proc. Natl. Acad. Sci. U. S. A. 106, 16446–16450.

Koenig, J., Linder, A.N., Leutgeb, J.K., and Leutgeb, S. (2011). The spatial periodicity of grid cells is not sustained during reduced theta oscillations. Science 332, 592–595.

Köhler, C. (1985). Intrinsic projections of the retrohippocampal region in the rat brain. I. The subicular complex. J. Comp. Neurol. 236:504–522.

Krook-Magnuson, E., Varga, C., Lee, S.H., and Soltesz, I. (2012). New dimensions of interneuronal specialization unmasked by principal cell heterogeneity. Trends Neurosci. 35, 175–184.

Krupic, J., Burgess, N., and O'Keefe, J. (2012). Neural representations of location composed of spatially periodic bands. Science 337, 853–857.

Kumar, S.S., and Buckmaster, P.S. (2006). Hyperexcitability, interneurons, and loss of GABAergic synapses in entorhinal cortex in a model of temporal lobe epilepsy. J. Neurosci. 26, 4613–4623.

Lang, S., Dercksen, V.J., Sakmann, B., and Oberlaender, M. (2011). Simulation of signal flow in 3D reconstructions of an anatomically realistic neural network in rat vibrissal cortex. Neural Networks 24, 998–1011.

Langston, R.F., Ainge, J.A., Couey, J.J., Canto, C.B., Bjerknes, T.L., Witter, M.P., Moser, E.I., and Moser, M.-B. (2010). Development of the spatial representation system in the rat. Science 328, 1576–1580.

Lee, W.C.A., and Reid, R.C. (2011). Specificity and randomness: Structure-function relationships in neural circuits. Curr. Opin. Neurobiol. 21, 801–807.

Lee, A.K., Manns, I.D., Sakmann, B., and Brecht, M. (2006). Whole-Cell Recordings in Freely Moving Rats. Neuron 51, 399–407.

Lee, A.K., Epsztein, J., and Brecht, M. (2009). Head-anchored whole-cell recordings in freely moving rats. Nat. Protoc. 4, 385–392.

Lee, J.H., Durand, R., Gradinaru, V., Zhang, F., Goshen, I., Kim, D.-S., Fenno, L.E., Ramakrishnan, C., and Deisseroth, K. (2010). Global and local fMRI signals driven by neurons defined optogenetically by type and wiring. Nature 465, 788–792.

Lever, C., Burton, S., Jeewajee, A., O'Keefe, J., and Burgess, N. (2009). Boundary vector cells in the subiculum of the hippocampal formation. J. Neurosci. 29, 9771-7.

Lingenhöhl, K., and Finch, D.M. (1991). Morphological characterization of rat entorhinal neurons in vivo: soma-dendritic structure and axonal domains. Exp. Brain. Res. 84, 57–74

Marx, M., Günter, R.H., Hucko, W., Radnikow, G., and Feldmeyer, D. (2012). Improved biocytin labeling and neuronal 3D reconstruction. Nat. Protoc. 7, 394–407.

Mileykovskiy, B., and Morales, M. (2011). Duration of inhibition of ventral tegmental area dopamine neurons encodes a level of conditioned fear. J. Neurosci. 31, 7471–7476.

Mitchell, S.J., Rawlins, J.N., Steward, O., and Olton, D.S. (1982). Medial septal area lesions disrupt theta rhythm and cholinergic staining in medial entorhinal cortex and produce impaired radial arm maze behavior in rats. J. Neurosci. 2:292–302.

Mizuseki, K., Sirota, A., Pastalkova, E., and Buzsáki, G. (2009). Theta Oscillations Provide Temporal Windows for Local Circuit Computation in the Entorhinal-Hippocampal Loop. Neuron 64, 267–280.

Moser, E.I., and Moser, M.-B. (2013). Grid cells and neural coding in high-end cortices. Neuron 80, 765–774.

Moser, E.I., Kropff, E., and Moser, M.-B. (2008). Place cells, grid cells, and the brain's spatial representation system. Annu. Rev. Neurosci. 31, 69–89.

Mulders, W.H.A.M., West, M.J., and Slomianka, L. (1997). Neuron numbers in the presubiculum, parasubiculum, and entorhinal area of the rat. J. Comp. Neurol. 385:83–94.

Muller, R.U., Kubie, J.L., and Ranck, J.B. (1987). Spatial firing patterns of hippocampal complex-spike cells in a fixed environment. J. Neurosci. 7, 1935–1950.

Newman, E.L., Climer, J.R., and Hasselmo, M.E. (2014). Grid cell spatial tuning reduced following systemic muscarinic receptor blockade. Hippocampus 24, 643-655.

Oberlaender, M., Boudewijns, Z.S.R.M., Kleele, T., Mansvelder, H.D., Sakmann, B., and de Kock, C.P.J. (2011). Three-dimensional axon morphologies of individual layer 5 neurons indicate cell type-specific intracortical pathways for whisker motion and touch. Proc. Natl. Acad. Sci. U. S. A. 108, 4188–4193.

Pastoll, H., Solanka, L., van Rossum, M.C.W., and Nolan, M.F. (2013). Feedback Inhibition Enables Theta-Nested Gamma Oscillations and Grid Firing Fields. Neuron 77:141–154.

Paxinos, G., and Watson, C. (2006). The Rat Brain in Stereotaxic Coordinates: Hard Cover Edition (Elsevier Science).

Peterson, D.A., Lucidi-Phillipi, C.A., Murphy, D.P., Ray, J., and Gage, F.H. (1996). Fibroblast growth factor-2 protects entorhinal layer II glutamatergic neurons from axotomy-induced death. J. Neurosci. 16, 886–898.

Pinault, D. (1994). Golgi-like labeling of a single neuron recorded extracellularly. Neurosci. Lett. 170, 255–260.

Pinault, D. (1996). A novel single-cell staining procedure performed in vivo under electrophysiological control: Morpho-functional features of juxtacellularly labeled thalamic cells and other central neurons with biocytin or Neurobiotin. J. Neurosci. Methods 65, 113–136.

Pinault, D. (2011). The Juxtacellular Recording-Labeling Technique. In Electrophysiological Recording Techniques SE - 3, R.P. Vertes, and R.W. Stackman Jr., eds. (Humana Press), pp. 41–75.

Pinault, D., and Deschênes, M. (1998). Projection and innervation patterns of individual thalamic reticular axons in the thalamus of the adult rat: a three-dimensional, graphic, and morphometric analysis. J. Comp. Neurol. 391, 180–203.

Pinault, D., Bourassa, J., and Deschenes, M. (1995). The axonal arborization of single thalamic reticular neurons in the somatosensory thalamus of the rat. Eur. J. Neurosci. 7, 31–40.

Potjans, T.C., and Diesmann, M. (2014). The cell-type specific cortical microcircuit: relating structure and activity in a full-scale spiking network model. Cereb. Cortex 24, 785–806.

Prakash, R., Yizhar, O., Grewe, B., Ramakrishnan, C., Wang, N., Goshen, I., Packer, A.M., Peterka, D.S., Yuste, R., Schnitzer, M.J., et al. (2012). Two-photon optogenetic toolbox for fast inhibition, excitation and bistable modulation. Nat. Methods 9, 1171–1179.

Quilichini, P., Sirota, A., and Buzsáki, G. (2010). Intrinsic circuit organization and theta-gamma oscillation dynamics in the entorhinal cortex of the rat. J. Neurosci. 18, 11128-11142.

Ramsden, H.L., Sürmeli, G., McDonagh, S.G., and Nolan, M.F. (2015). Laminar and dorsoventral molecular organization of the medial entorhinal cortex revealed by large-scale anatomical analysis of gene expression. PLoS Comput. Biol. in press.

Ray, S., Naumann, R., Burgalossi, A., Tang, Q., Schmidt, H., and Brecht, M. (2014). Grid-layout and theta-modulation of layer 2 pyramidal neurons in medial entorhinal cortex. Science 343, 891–896.

Rowland, D.C., and Moser, M.-B. (2014). From cortical modules to memories. Curr. Opin. Neurobiol. 24, 22-27.

Sargolini, F., Fyhn, M., Hafting, T., McNaughton, B.L., Witter, M.P., Moser, M.-B., and Moser, E.I. (2006). Conjunctive representation of position, direction, and velocity in entorhinal cortex. Science 312, 758–762.

Savelli, F., Yoganarasimha, D., and Knierim, J.J. (2008). Influence of boundary removal on the spatial representations of the medial entorhinal cortex. Hippocampus 18, 1270-82.

Schmidt-Hieber, C., and Häusser, M. (2013). Cellular mechanisms of spatial navigation in the medial entorhinal cortex. Nat. Neurosci. 16, 325–331.

Schwarz, C., Hentschke, H., Butovas, S., Haiss, F., Stüttgen, M.C., Gerdjikov, T. V, Bergner, C.G., and Waiblinger, C. (2010). The head-fixed behaving rat--procedures and pitfalls. Somatosens. Mot. Res. 27, 131–148.

Sillitoe, R.V., and Hawkes, R. (2002). Whole-mount immunohistochemistry: a high-throughput screen for patterning defects in the mouse cerebellum. J. Histochem. Cytochem. 50, 235–244.

Skaggs, W.E., McNaughton, B.L., Gothard, K.M., and Markus, E.J. (1993). An information-theoretic approach to deciphering the hippocampal code. In Advances in Neural Processing Systems, Volume 5, S.J. Hanson, J.D. Cowan, and C.L. Giles, eds. (San Mateo: Morgan Kaufmann), pp. 1030–1037.

Slomianka, L., and Geneser, F.A. (1991). Distribution of acetylcholinesterase in the hippocampal region of the mouse: I. Entorhinal area, parasubiculum, retrosplenial area, and presubiculum. J. Comp. Neurol. 303:339–354.

Solstad, T., Boccara, C.N., Kropff, E., Moser, M.-B., and Moser, E.I. (2008). Representation of geometric borders in the entorhinal cortex. Science 322, 1865–1868.

Stensola, H., Stensola, T., Solstad, T., Frøland, K., Moser, M.-B., and Moser E. I. (2012). The entorhinal grid map is discretized. Nature 492, 72–78.

van Strien, N.M., Cappaert, N.L.M., and Witter, M.P. (2009). The anatomy of memory: an interactive overview of the parahippocampal-hippocampal network. Nat. Rev. Neurosci. 10:272–282.

Tamamaki, N., and Nojyo, Y. (1993). Projection of the entorhinal layer II neurons in the rat as revealed by intracellular pressure-injection of neurobiotin. Hippocampus 3, 471–480.

Tang, Q., Brecht, M., and Burgalossi, A. (2014). Juxtacellular recording and morphological identification of single neurons in freely moving rats. Nat. Protoc. 9, 2369-2381.

Tang, Q., Burgalossi, A., Ebbesen, C.L., Ray, S., Naumann, R., Schmidt, H., Spicher, D., and Brecht, M. (2014). Pyramidal and Stellate Cell Specificity of Grid and Border Representations in Layer 2 of Medial Entorhinal Cortex. Neuron 2014 Dec 17;84 http://dx.doi.org/10.1016/j.neuron.2014.11.009.

Taube, J.S. (1995). Place cells recorded in the parasubiculum of freely moving rats. Hippocampus 5:569–583.

Taube, J.S. (2007). The head direction signal: origins and sensory-motor integration. Annu. Rev. Neurosci. 30, 181–207.

Taube, J.S., Muller, R.U., and Ranck, J.B. (1990). Head-direction cells recorded from the postsubiculum in freely moving rats. I. Description and quantitative analysis. J. Neurosci. 10, 420–435.

Thompson, C.L., Pathak, S.D., Jeromin, A., Ng, L.L., MacPherson, C.R., Mortrud, M.T., Cusick, A., Riley, Z.L., Sunkin, S.M., Bernard, A., et al. (2008). Genomic Anatomy of the Hippocampus. Neuron 60, 1010–1021.

Tsuji, S. (1998). Electron microscopic localization of acetylcholinesterase activity in the central nervous system: chemical basis of a catalytic activity of Hatchett's brown (cupric ferrocyanide) precipitate revealed by 3,3'-diaminobenzidine. Folia Histochem. Cytobiol. 36, 67–70.

Tsuno, Y., Schultheiss, N.W., and Hasselmo, M.E. (2013). In vivo cholinergic modulation of the cellular properties of medial entorhinal cortex neurons. J. Physiol. 591, 2611–2627.

Varga, C., Lee, S.Y., and Soltesz, I. (2010). Target-selective GABAergic control of entorhinal cortex output. Nat. Neurosci. 13, 822–824.

Veenman, C.L., Reiner, A., and Honig, M.G. (1992). Biotinylated dextran amine as an anterograde tracer for single- and double-labeling studies. J. Neurosci. Methods 41, 239–254.

Wang, J., Wagner, F., Borton, D. a, Zhang, J., Ozden, I., Burwell, R.D., Nurmikko, A. V, van Wagenen, R., Diester, I., and Deisseroth, K. (2012). Integrated device for combined optical neuromodulation and electrical recording for chronic in vivo applications. J. Neural Eng. 9, 016001.

Wills, T.J., Cacucci, F., Burgess, N., and O'Keefe, J. (2010). Development of the hippocampal cognitive map in preweanling rats. Science 328, 1573-1576.

Witter, M.P., Groenewegen, H.J., Lopes da Silva, F.H., and Lohman, A.H. (1989). Functional organization of the extrinsic and intrinsic circuitry of the parahippocampal region. Prog. Neurobiol. 33, 161–253.

Woolsey, T.A., and van der Loos, H. (1970). The structural organization of layer IV in the somatosensory region (SI) of mouse cerebral cortex. The description of a cortical field composed of discrete cytoarchitectonic units. Brain Res. 17, 205–242.

Zhang, F., Wang, L.-P., Brauner, M., Liewald, J.F., Kay, K., Watzke, N., Wood, P.G., Bamberg, E., Nagel, G., Gottschalk, A., et al. (2007). Multimodal fast optical interrogation of neural circuitry. Nature 446, 633–639.

Zhang, F., Gradinaru, V., Adamantidis, A.R., Durand, R., Airan, R.D., de Lecea, L., and Deisseroth, K. (2010). Optogenetic interrogation of neural circuits: technology for probing mammalian brain structures. Nat. Protoc. 5, 439–456.

9.   Acknowledgements

I would express my greatest thankfulness to the Brecht lab for the fruitful 3 years of PhD study. First of all, I appreciate my supervisor, Prof. Michael Brecht, for his passion, curiosity and creativity in scientific resarch, and constant guidance into the exciting scientific topics. I would also like to thank many of my colleagues and friends in the Brecht lab:

- Dr. Andrea Burgalossi, the most talented electrophysiologist I have ever seen, who supervised me with his patience, knowledge and experience in pioneering the juxtacellular recordingsthroughout my PhD, and it's always very encouraging and fun collaborating with.
- Dr. John Tukker, who generously shared not only his experiment setup, but also his years of knowledge about in vivo electrophysiology and scientific reasoning in neuroscience.
- Dr. Moritz von Heimendahl, who is an excellent scientist with superb computational competence, mentored me from the first day of joining the lab in scientific programming, statistical methods and the logic behind data analysis, and in career planning.
- Saikat Ray, with whom we worked as a team in combining interesting anatomy with electrophysiology. His technical expertise and experience in both anatomy and programming, as well as frequent discussions on scientific progress in neuroscience, helped in many ways..
- Chrstian Ebbesen, who is incredibly productive and efficient in conducting experiments and performing sophisticated analysis. It has been very lucky to work with him on various projects during my PhD, who really made a huge difference.
- Brigitte Geue, Undine Schneeweiss and Juliane Steger, our best lab technicians, provided excellent technical assistance and support.
- Andreea Neukirchner, who helped me so much on all sorts of administrative troubles from the beginning to the end of my PhD.
- Constanze Lenschow, Dr. Andrea Burgalossi, Dr. Ann Clemens, Saikat Ray and Christian Ebbesen who read my thesis and provided critical comments.

Finally, I would like to thank all my family members and friends, to be always with me for this period abroad, I miss you all. Likewise, I would appreciate a lot on our collaborators and colleagues all over the world working on this field, to provide insights, critical comments and suggestions to my work. Most particularly, I thank my wife Rachel Li, the most important girl in my life, to be always with me during my PhD, and for the rest of my lifetime.

To Rachel Li

10.   Selbständigkeitserklärung

Ich erkläre hiermit, dass ich die vorliegende Arbeit ohne fremde Hilfe selbständig verfasst und keine anderen als die im Quellenverzeichnis angegebenen Hilfsmittel verwendet habe.

Ich erkläre weiterhin, dass ich alles gedanklich, inhaltlich oder wörtlich von anderen (z.B. aus Büchern, Zeitschriften, Zeitungen, Lexika, Internet usw.) Übernommene als solches kenntlich gemacht und gemäß den mir bekannten gängigen wissenschaftlichen Regeln korrekt zitiert, d.h. die jeweilige Herkunft im Text oder in den Anmerkungen belegt habe. Dies gilt gegebenenfalls auch für Tabellen, Skizzen, Zeichnungen, bildliche Darstellungen usw. In diesem Zusammenhang muss erwähnt werden, dass der Großteil der vorliegenden Arbeit in wissenschaftlichen Zeitschriften publiziert wurde. Aus diesem Grund sind Ähnlichkeiten in Text oder Abbildungen unvermeidbar. Alle Übereinstimmungen in Text oder Abbildungen aus meinen publizierten Artikeln wurden als solche kenntlich gemacht.

Ich nehme zur Kenntnis, dass die – auch zu einem späteren Zeitpunkt – nachgewiesene Unterlassung der Herkunftsangabe, das Fehlen von Zitationshinweisen, als versuchte Täuschung bzw. als Plagiat („geistiger Diebstahl") gewertet werden wird.

Ich erkenne hiermit an, dass bei Vorliegen eines Plagiats die Arbeit nicht als selbstständige Leistung gewertet werden wird mit der Folge, dass mein Anspruch auf einen Leistungsnachweis entfällt.

Berlin, _____

_____

Declaration

I, the undersigned, declare that this dissertation is my own work, and all the resources I have used or quoted have been indicated or acknowledged by means of completed references. Some parts of the work included in this dissertation have been conducted collaboratively; I provide here a statement of my experimental contributions to the data presented:

Grid-Layout and Theta-Modulation of Layer 2 Pyramidal Neurons in Medial Entorhinal Cortex

I performed most of the in vivo anesthetized and free moving electrophysiology experiments and in vivo pharmacology blockade experiments. Dr. Andrea Burgalossi supervised and helped the electrophysiology experiments. Saikat Ray, Dr. Robert Naumann and Helene Schmidt performed most of the anatomy stainings and experiments.

Establishment of Juxtacellular Recordings in Freely Moving Rats

I tested the experimental equipments, established the experimental protocols and conducted most of the in vivo freely moving experiments. Dr. Andrea Burgalossi conceived the project, supervised all the experimental work and provided comments on the methodological improvements.

Pyramidal and Stellate Cell Specificity of Grid and Border Representations in Layer 2 of Medial Entorhinal Cortex

I performed most of the in vivo freely moving juxtacellular recording experiments under the guidance of Dr. Andrea Burgalossi. Christian Ebbesen performed tetrode recordings, wrote the MatLab scrripts for classifier and analyzed the data. Dominik Spicher designed and tested early versions of the classifier. Saikat Ray, Dr. Robert Naumann and Helene Schmidt helped on the anatomy.

Functional Architecture of the Rat Parasubiculum

I performed most of the in vivo freely moving juxtacellular recording experiments under the guidance of Dr. Andrea Burgalossi. Dr. John Tukker performed virus injections. Helene Schmidt, Saikat Ray and Dr. Robert Naumann helped on the anatomy.

In addition to the experimental contributions, and referring to all the chapters above, I contributed to all the experimental design, data analysis, writing and proofreading of manuscripts. Most of my PhD work has been published in scientific journals already (see notes under each Chapter), therefore the similarities between this dissertation and published articles are unavoidable, but by no means intended. Both the contents and figures reproduced from my published papers are properly cited.

Berlin, _____

_____